A THEORETICAL STUDY OF HEAVY ION COLLISIONS AND RELATED DYNAMICAL ASPECTS

A THESIS

Submitted to the

FACULTY OF SCIENCE

THAPAR INSTITUTE OF ENGINEERING

AND TECHNOLOGY (TIET), PATIALA

for the degree of

DOCTOR OF PHILOSOPHY

by

RAJNI

THAPAR INSTITUTE
OF ENGINEERING & TECHNOLOGY
(Deemed to be University)

SCHOOL OF PHYSICS AND MATERIALS SCIENCE

TIET, PATIALA-147004

INDIA

Dedicated to

My Family

&

My Supervisor

CERTIFICATE

This is to certify that the thesis entitled "**A THEORETICAL STUDY OF HEAVY ION COLLISIONS AND RELATED DYNAMICAL ASPECTS**" being submitted by **Ms. Rajni** for the fulfillment of the requirements for the award of Degree of Doctor of Philosophy in the School of Physics and Materials Science, Thapar Institute of Engineering and Technology, Patiala, is a record of the candidate's own work carried out by her under my supervision. The matter presented in this thesis has not been submitted in part or full for the award of any degree in any university or institute.

Supervisor

Dr. Manoj K. Sharma

Professor and Head

School of Physics and Materials Science

Thapar Institute of Engineering and Technology (TIET)

Patiala- 147004

Punjab (India)

CANDIDATE'S DECLARATION

I hereby certify that the thesis entitled "**A THEORETICAL STUDY OF HEAVY ION COLLISIONS AND RELATED DYNAMICAL ASPECTS**" in partial fulfillment of the requirements for the award of Degree of Doctor of Philosophy in the School of Physics and Materials Science, Thapar Institute of Engineering and Technology, Patiala, is a record of my own work carried under the supervision of Prof. Manoj K. Sharma. The matter presented in this thesis has not been submitted by me in part or full for the award of any other degree in any other university or institute.

(Rajni)

This is to certify that the above statement made by the candidate is correct to the best of our knowledge.

Prof. Manoj K. Sharma
(Supervisor and HOD)

Dean R&SP

External Examiner

Date 18.04.2018

Acknowledgments

Undertaking this PhD has been a truly life changing experience for me and it would not have been possible to do without the support and guidance that I received from many people. I give my enormous thanks to GOD because he has been my stronghold during these years of study.

At this moment of accomplishment, I would like to express my sincere gratitude to my esteemed supervisor Prof. Manoj K. Sharma, Head, School of Physics and Materials Science, Thapar Institute of Engineering and Technology (TIET) Patiala, for his sagacious guidance, sympathetic approach and relentless support I received throughout the research work. I am very grateful for his serenity inspiration, passion, and enormous knowledge in nuclear physics that together, make him great mentor. It is my honor to be work under his generous and able supervision. Thank you for believing in me and encouraging my research. His guidance helped me in all the time of research and writing of this thesis. He was always there to 'repair' whatever 'problem' I may have involuntarily created. I would like to thank him for teaching me how to fulfil my potential and expanding my horizons. Special thanks to Sonam mam for all her love and affection.

I am profoundly obliged to my thesis committee members Dr. Alka Updhyay, Dr. Raj Kumar and Dr. Mahesh Kumar for their constructive ideas during the progress report. I express my sincere thanks to Prof. O. P. Pandey, Dean, Research and Sponsored Projects for providing the possible research facilities here at TIET Campus and fellowship as a teaching associate well in time. He also help me to attend national and international conferences financially. Special thanks to Prof. Kulvir Singh for his encouragement and constant moral support throughout my Ph.D. I greatly appreciate the help and co-operation extended by all the faculty and staff of the School for their help and kind support.

This thesis has been kept on track and been seen through to completion with the support of my seniors Dr. Gudveen Sawhney, Dr. Manpreet Kaur, Dr. Gurvinder Kaur, Dr. Kirandeep Sandhu, Dr. Mahesh Kumar Sharma and Dr. Manjeet Singh

Gautam. I respect their distinguished helping nature. My very earnest thanks to Dr. Raj Kumar and Dr. Deepika Jain for their unremitting encouragement, guidance and moral support. I am happy to acknowledge the contribution and suggestions from my lab mates Amandeep, Neha, Kanishka, Aman, Gurjit, Ishita and Shivani. I owe a deep sense of gratitude to my friends Gitanjali, Sakshi and Mitul, who incentive me to strive towards my goal. Thank you guys for all the enjoyment, moral support and delightful company. I am also thankful to members of other lab groups specially Ms. Sangeeta, Dr. Chandni Khurana, Dr. Samiksha Verma, Dr. Anupriya Jain, Dr. Harjinder Singh, Dr. Meenakshi Batra and Dr. Mintu Tiyagi for their help and all the fun we had during Ph.D.

I am short in words to express my inner sentiments towards my family members for their support and pushing through the hard time, which has made it possible for me to reach end of this voyage. I feel a profound sense of gratitude to my late father Shri. Sunil Kumar Mittal who formed part of my vision and taught me the good things that actually matter in life. The memories of my father still provide continual motivation for my journey in this life. My vocabulary fails to convey depth of my feelings for my mother Mrs. Promila Mittal, my elder sisters Vidhi and Nidhi and my younger brother Aayush. Thank you Mummy for your love, patience, understanding and for all of the sacrifices that you've made on my behalf and allowed me to spend most of the time on this thesis. I am also very thankful to my brother in law Mr. Deepak Mittal who always encourage me to do better and help me in many ways throughout my Ph.D. A special thanks goes to my niece Ruhi and my nephew Aariketh, their smiling and innocent faces worked as stress buster for me and always makes me feel revitalizing and happy.

I gratefully acknowledge the funding source University Grant Commission (UGC), New Delhi, that made my Ph.D work possible.

Patiala
December, 2017 (Rajni)

List of Publications

I. International Journals:

1. Formation and decay of ^{200}Pb* using different incoming channels, **Rajni**, Raj Kumar and Manoj. K. Sharma, Phys. Rev. C **90**, 044604 (2014).

2. Dynamics of ^{16,18}O induced reactions using Ni, Ge and Mo targets, **Rajni**, Gurvinder Kaur and Manoj K. Sharma, Int. J. Mod. Phys. E. **25**, 1650091 (2016).

3. Influence of sticking vs non-sticking limits of moment of inertia and higher order deformations in the decay of ^{214,216}Rn* compound nuclei, **Rajni**, Deepika Jain and Manoj K. Sharma, Nucl. Phys. A **968**, 436-452 (2017).

4. Impact of spin-orbit density dependent potential in heavy ion reactions forming Se nuclei, **Rajni**, Deepika Jain, Ishita Sharma and Manoj K. Sharma, Eur. Phys. J. A **53**, 208 (2017).

5. Decay of Zr isotopes and related nuclear structure effects using collective clusterization approach, Gurvinder Kaur, **Rajni** and Manoj K. Sharma, Phys. Scr. **T166**, 014013 (2015).

6. Role of Barrier modification and inelastic surface excitations in sub-barrier fusion of $_{16}{}^{32}$S+$_{40}{}^{94}$Zr reaction, M. S. Gautam, **Rajni** and Manoj K. Sharma, Braz. J. of Phys. **46**, 133-142 (2016). (not included in thesis)

7. Systematic analysis of hot Yb* isotopes using energy density formalism, Deepika Jain, Manoj K. Sharma, **Rajni**, Raj Kumar and Raj K. Gupta, Eur. Phys. J. A **50**, 155 (2014).

8. Role of rotational energy component in the dynamics of $^{16}O+^{198}Pt$ reaction, Manoj K. Sharma, **Rajni** and Deepika Jain, EPJ Web of Conf. **146**, 12035 (2017).

9. Effect of deformation and orientation on spin orbit density dependent nuclear potential, **Rajni**, Raj Kumar and Manoj K. Sharma, EPJ Web of Conf. **163**, 00038 (2017).

10. Sticking versus non-sticking moment of inertia in the $^{9}Be + ^{232}Th$ reaction, G. Sawhney, R. Kumar, **Rajni** and Manoj K. Sharma, AIP Conf. Proc. **1524**, 174-177 (2013).

II. In International/National Conferences, Symposiums and Workshops:

1. Decay of $^{200}Pb^{*}$ formed in $^{30}Si+^{170}Er$ reaction, **Rajni**, Raj Kumar and Manoj K Sharma, 16th Punjab Science Congress, Feb. 7-9, 2013, Faridkot, India.

2. Systematics in the decay pattern of even mass Zr isotopes, Gurvinder Kaur, **Rajni** and Manoj K Sharma, X Latin American Symposium on Nuclear Physics and Applications, Dec 01- 06, 2013, Montevideo, Uruguay.

3. Entrance channel effect in the formation of ^{200}Pb, **Rajni**, Raj Kumar, Deepika Jain and Manoj K Sharma, DAE symposium on Nuclear Physics, Vol. **58**, 412, Dec. 2-6, 2013, BARC, Mumbai, india.

4. Study of compound system $^{200}Pb^{*}$, **Rajni** and Manoj K Sharma, Emerging Trends in Physics for Ionizing Radiations, Aerosols and Material Science (ETPRAM), Dec. 13-14, (2013), Punjabi University, Patiala, India.

5. Fusion hindrance in $^{27}Al+^{45}Sc$ reaction using dynamical cluster decay model, **Rajni**, Deepika Jain and Manoj K Sharma, National conference on Emerging

challenges in Nuclear and Many body physics (ECNMP-14), Nov. 10-11, 2014, Jammu University, Jammu, India.

6. Average total kinetic energy for Pb isotopes using Fragmentation theory, Raj Kumar, **Rajni** and Manoj K. Sharma, DAE symposium on Nuclear Physics, Vol. **59**, 514-515, 2014, BHU, Varanasi, India.

7. Study of barrier modification using Hill-Wheeler and WKB approximation in Wong Model, Deepika Jain, Manoj K. Sharma, **Rajni** and Raj Kumar, DAE symposium on Nuclear Physics, Vol. **59**, 520-521, 2014, BHU, Varanasi, india.

8. Dynamics of ^{92}Zr and ^{108,110}Sn nuclei formed in ^{16,18}O induced reactions, **Rajni**, Kanishka Sharma, Gurvinder kaur and Manoj K. Sharma, DAE symposium on Nuclear Physics, Vol. **59**, 562-563, 2014, BHU, Varanasi, India.

9. Dynamics of ^{72}Se from nuclear prospective, **Rajni**, Deepika Jain and Manoj K Sharma, National Conference on Advances in Engineering Materials (NAEM) 2015, March 20-22, 2015, Department of Physics, DIT University, Dehradun, India.

10. Role of spin orbit interaction potential in two nucleon transfer reactions, **Rajni**, Ishita Sharma, Deepika Jain and Manoj K Sharma, DAE symposium on Nuclear Physics, Vol. **60**, 332-333, 2015, SSSIHL, Prasanthi Nilayam, (A.P.), India.

11. Stability aspects of radioactive isotopes of Rn nucleus, **Rajni** and Manoj K Sharma, National Conference on Application of Radioisotopes and Radiation Technology in Industry Healthcare and Agriculture (ARRTIHA-2016), Nov 28-29, 2016, Department of Chemical Engineering, Thapar University, Patiala, India.

12. Probing surface diffuseness of nucleus-nucleus interaction potential in Mass range A=24-206, **Rajni** and Manoj K Sharma, International Nuclear Physics

Conference (INPC), Sept. 11-16, 2016, Adelaide, Australia.

13. Impact of double spin component within the energy density formalism, **Rajni**, Deepika Jain, Raj Kumar and Manoj K Sharma, DAE symposium on Nuclear Physics, Vol. **61**, 584, 2016, Kolkata, India.

14. Effect of incident channel properties on the fusion dynamics, Ishita Sharma, **Rajni**, Raj Kumar and Manoj K Sharma, DAE symposium on Nuclear Physics, Vol. **62**, 606, 2017, TIET, Patiala, India.

Contents

List of Tables

List of Figures

Abstract

In this thesis, a comprehensive study is carried out to explore the formation and decay mechanism of various nuclear systems formed in heavy ion induced reactions. The Wong and ℓ-summed Wong formula are applied to account for the formation process, whereas dynamical cluster decay model (DCM) employed to address the decay paths of hot and rotating compound nuclei. To investigate both the processes, two sets of nuclear interaction potentials are employed *i.e.* one based on the proximity based pocket formula and other obtained from the Skyrme Energy Density Formalism (SEDF). It is relevant to mention here that, the angular momentum, temperature, deformations and orientation effects of the reacting partners and decaying products are aptly contained respectively in Wong and DCM model. The thesis is organized into seven chapters, a transient discussion of which is discussed below.

Chapter 1 presents the brief account of heavy ion induced nuclear reactions governing the dynamics at low energy region. A literature survey on the formation and decay of compound nucleus is discussed in detail. To understand the mechanisms involved in fusion-fission processes and to extract related nuclear structure effects, a deep understanding of nucleus-nucleus interaction potentials is crucial, a brief interpretation of which is discussed in this chapter. Along with this, the deformation and orientation effects in view of dynamics governed via heavy ion reactions is discussed in brief.

Chapter 2 describe the details of the methodology used to probe the formation and decay mechanism of heavy ion induced compound nucleus reactions. Wong formula and its extended version i.e. ℓ-summed Wong formula are used to study the formation phenomena. The dynamical cluster-decay model (DCM) which originate from the well known Quantum Mechanical Fragmentation Theory ($QMFT$) is applied to investigate the decay mechanism of excited compound nucleus, in the form

of evaporation residue, intermediate mass fragments, heavy mass fragments and fission fragments etc. DCM is a non-statistical model and provide an advantage to treat all compound nucleus decay processes on parallel footing. Within DCM, the fragmentation potential is obtained as a sum of Coulomb, nuclear proximity (based on Blocki *et al.* potential and Skyrme energy density formalism) and centrifugal potentials, a brief detail of all outlined in this chapter.

In **Chapter 3**, Entrance channel effect is studied in the dynamics of ^{200}Pb* formed in ^{16}O+^{184}W, ^{19}F+^{181}Ta and ^{30}Si+^{170}Er reactions over a wide range of excitation energies using the dynamical cluster-decay model (DCM) and Wong model. The effect of deformations upto β_2 along with optimum orientation is investigated in both the formalisms. Fusion cross-section is studied using Wong model, which overestimates experimental data for ^{19}F+^{181}Ta and ^{30}Si+^{170}Er reactions and underestimates the data at few energies for ^{16}O+^{184}W. However with the use of extended ℓ-summed Wong model, the overestimation is taken care and the cross-sections are fitted nicely. The Wong based calculations suggest that there might be some non-compound nucleus contribution at few energies for ^{16}O+^{184}W channel, as the underestimation of cross-section persists even after the inclusion of deformation effects. This lead us to conclude that the formation of ^{200}Pb* compound nucleus depends on the choice of incoming channel. In addition to this, in this chapter, the decay path of ^{200}Pb* is investigated using DCM. Although, the overall decay pattern of compound nucleus ^{200}Pb* seems similar for all the chosen reactions, some signature of variation are observed in fission and intermediate mass fragment (IMF) region for the deformed fragmentation process. It is to be noted that with the inclusion of deformation, the decay pattern changes from symmetric to asymmetric, there by suggesting that the deformation and orientation of decaying fragment are equally important in formation as well as in the decay process of proton magic nuclear system ^{200}Pb*. Prediction of ER and fission cross-sections at higher as well as at lower incident energies are also worked out. Beside this, the dynamics of neighboring

nuclei $^{192}Pb^*$ and $^{202}Pb^*$ is also analyzed.

In **Chapter 4**, the reaction dynamics of various even-mass Zr isotopes is explored formed in ^{16}O-induced reactions is explored using DCM based on collective clusterization approach. In reference to the measured fusion cross-section data, various decay modes contributing towards $^{86,88,90,92}Zr^*$ nuclei are investigated. Also, the role of deformations and orientation degree of freedom is analyzed by comparing results with spherical choice of fragmentation. In addition to this, the entrance channel impact is explored for $^{92}Zr^*$ and $^{76}Kr^*$ nuclei formed in ^{16}O and ^{18}O induced reactions. Besides this the dynamics of relatively heavier Sn isotopes formed using using ^{16}O and ^{18}O beams is analysed. The DCM calculated decay cross-sections find a nice agrement with available experimental data.

In **Chapter 5** the dynamical cluster decay model (DCM) is employed to explore the relative effect of sticking (I_S) and non-sticking (I_{NS}) limits of moment of inertia (MOI) in the decay of hot and rotating $^{214,216}Rn^*$ compound nuclei, formed in $^{16,18}O+^{198}Pt$ reactions. Beside this, the nuclear deformation effects i.e. quadrupole β_2 (static and dynamic) and higher order static deformation up to hexadecapole (β_4) are duly incorporated within the framework of DCM. The influence of both I_S and I_{NS} addressing rotational energy component is gauged through the barrier characteristics, preformation factor and barrier lowering effects via proper inclusion of deformation effects of decaying fragments. The experimentally given ER and fusion-fission (ff) data is addressed by optimizing the neck-length ΔR, that strongly depends on the limiting angular momentum, which in turn depends on the sticking or non-sticking limits of interaction. In addition to this, the influence of increase in energy and neutron number is probed in reference to ER survival probability of Rn compound nucleus. Finally, the ff cross-sections of $^{214,216}Rn^*$ nuclei are predicted within sticking limit of moment of inertia as the same seems to be more suitable heavy particle emission.

In all previous chapters, the nuclear dynamics and related deformations effects

are investigated within Blocki based nuclear proximity potential. Such kind of analytical form of nuclear interaction potential does not contain individual contribution from spin-orbit density dependent part, though it affects the fusion-fission dynamics appreciably. Henceforth in **Chapter 6**, role of deformation and orientation in nuclear dynamics is investigated in terms of spin-orbit density dependent part V_J of nuclear potential (V_N=V_P+V_J) obtained within semi-classical Thomas Fermi approach of Skyrme energy density formalism. Calculations are performed for $^{24-54}$Si+^{30}Si reactions, with spherical target ^{30}Si and projectiles $^{24-54}$Si having prolate and oblate shapes. The quadrupole deformation β_2 varies within range of $0.023 \leq \beta_2 \leq 0.531$ for prolate and $-0.242 \leq \beta_2 \leq -0.592$ for oblate projectiles. Si-nuclei with $\beta_2 < 0$ have higher spin-orbit barrier (compact spin-orbit configuration) in comparison to systems with $\beta_2 > 0$. The possible role of spin-orbit potential on barrier characteristics such as barrier height, barrier curvature and on the fusion pocket etc is probed. In reference to prolate and oblate systems, the angular dependence of spin-orbit potential is further studied on fusion cross-sections. Along with this, the effect of spin-orbit interaction potential is explored by considering a two nucleon transfer process by employing various entrance channels such as ^{23}Na+^{49}V,^{25}Mg+^{47}Ti,^{27}Al+^{45}Sc,^{29}Si+^{43}Ca and ^{31}P+^{41}K, all forming the same compound system ^{72}Se*, using both spherical as well as β_2-deformed choice of nuclei. For spherical nuclei, the spin-orbit density part V_J of nucleon-nucleon potential remain unaffected with the transfer of two nucleon from target to projectile, however show notable variation in magnitude after inclusion of deformation effects. Likewise, deformations play important role in spin-orbit density independent part V_P, as the fusion pocket start appearing, which otherwise diminish for the spherical nuclei. Further, the effect of increase in N/Z ratio of Se is explored on V_J as well as V_P and results are compared with transfer channels. In addition to this, the role of double spin-orbit parameter (W_0 and W_0') is explored in view of SkI2, SkI3 and SkI4 Skyrme forces. Also, the decay path of ^{72}Se* nucleus formed in ^{27}Al+^{45}Sc reaction is

investigated within framework of dynamical cluster decay model (DCM), where the nuclear proximity potential is obtained by both Skyrme energy density formalism (SEDF) and proximity pocket formula. The fusion hindrance in ^{27}Al+^{45}Sc reaction is also addressed via barrier lowering parameter ΔV_B. Finally, the contribution of spin-orbit density dependent interaction potential is estimated for ^{27}Al+^{45}Sc reaction using single (W_0) and double spin-orbit parameter (W_0 and W_0').

Chapter 7, summarizes the work carried out in this thesis. A brief account of results obtained and conclusion drawn is discussed and possible extension of this work from future prospective is outlined.

Chapter 1

Introduction

In this macrocosm, numerous processes supervene every day at the diminutive and lucid levels. All these processes are the pursuance of some kind of nuclear reactions governed through the static and dynamical nuclear features. The most notable nuclear reaction is the nuclear fusion of light elements that endowment energy production of stars and the sun. An extensive applications of the nuclear reactions that influence the daily life of human society is most prominently espied in production of energy and medicine. Therefore, to have a better insight of such mechanisms, a deep understanding of nuclear reactions and related aspects is immensely desirable. Inspite of naturally occurring reactions, large number of nuclear reactions have been exercised artificially in various laboratories around the globe. The first experimental corroboration of nuclear reaction was observed almost a century ago by Rutherford [1]. Since then, the study of these reactions were being accompanied by several fundamental discoveries, such as discovery of neutron, nuclear fission, production of the superheavy elements, elementary particles, a new state of matter; quark-gluon plasma etc.

During the earlier time, light particle such as proton, neutron and alpha particle were used to trigger the reactions. Later on, experimental techniques in the area of nuclear physics got ameliorated with the invention of highly advanced particle accelerators techniques and made in possible to synthesize nuclear reactions using

high energy beam of heavy ions. The term heavy ions (HI) usually means nuclei equal to or heavier than the alpha particle ($^4_2$He). The availability of HI beam opens new horizon for exploring field of nuclear physics. Moreover, HI collisions give the possibility to extract information about the nuclear matter behavior and to study the reaction mechanisms over an extensive energy region. In the quest to extend the periodic table element by element, the beams of ^{12}C, ^{14}N, ^{16}O, ^{35}Cl, ^{40}Ar, ^{48}Ca and even higher projectile are being used to synthesize new and exotic nuclear systems. Inspite of stable ion beam, some loosely bound isotopes of He, Li and Be etc. [2] possess peculiar properties and hence affect the fusion reaction dynamics accordingly. To achieve the pure and intense beams of the desired energy, HI-accelerators are required. The construction of modern heavy ion accelerators is influenced by the subsistence of appropriate ion source and should provide beams of high intensity, good emittance, long lifetime and production of great variety of ions. The commonly used ion sources for the production of HI are penning hot, cold and self heated cathode etc. These ion sources have been developed in number of laboratories, particularly in Berkeley at Lawrence Berkaley National Laboratory (LBNL) and in Dubna at Joint Institute for Nuclear Research (JINR). In early days of experiments at Berkeley laboratory, the spark-type ion sources were operated to accelerate the heavy ions, these ion sources were analogous to those used in spectroscopy [3]. Moreover, a source of same variety is also practised on the heavy-ion linac at Kharkov [4].

The main aim of the theoreticians working in the area of nuclear physics is to understand the properties of nuclei which can be described in the form of rudimentary theories of prescribed legitimacy that account for the structure of nuclei, forces between them and their internal motion. The macroscopic properties of nuclei such as constant density and binding energy per nucleon resembles to those of drop of liquid, however, the microscopic features like nuclear wave function and particle motion be similar with weakly interacting gas. The macroscopic part of nuclei is

best understood by the Liquid drop model (LDP) [5], whereas for the microscopic characteristics; Shell model (SM) and Fermi Gas Model (FM) [6] are superlative options. The SM and LDM are the basic types of simple nuclear models used to address the properties and behavior of nucleons within the nucleus. The shell model is based on the quantum mechanical hypothesis and deals with an individual particle showing that all the nucleons are in discrete energy states. On the other hand, the liquid drop model is established using a semi-classical idea, in accordance with collective particle state. Later on, some unified or collective models are built up that comprise both the features of SM and LDM. Since the complete perceptive of nuclear forces leads to remarkable growth in the overall understanding and behavior of nuclei, therefore continuous attempts are being made to have extensive idea about nuclear forces involved in the process. Each type of nuclear reaction displays specific and certain types of nuclear properties which guide us to investigate the nuclear structure and related dynamics such as (i) the information regarding the elementary nuclear forces is indulged through the nucleon-nucleon scattering, where the elastic scattering reaction gives the information about the size of nuclei and the interaction potential (ii) the reactions in which compound nuclei (CN) are formed, used to study the statistical nuclear properties and related nuclear dynamics.

1.1 Heavy ion-induced reaction mechanism at low energy

For nuclear physics community, the study of heavy ion induced nuclear reactions is a subject of resurgence interest, as it gives direction to understand the nuclear forces origin and consequently provide the much needed nuclear structure information. With the advancement in the technology, heavy-ion reactions (HIR) can occur at different bombarding energies from a few MeV/nucleon to a few GeV/nucleon and thus lead to a variety of nuclear phenomena. Our main focus here is to address

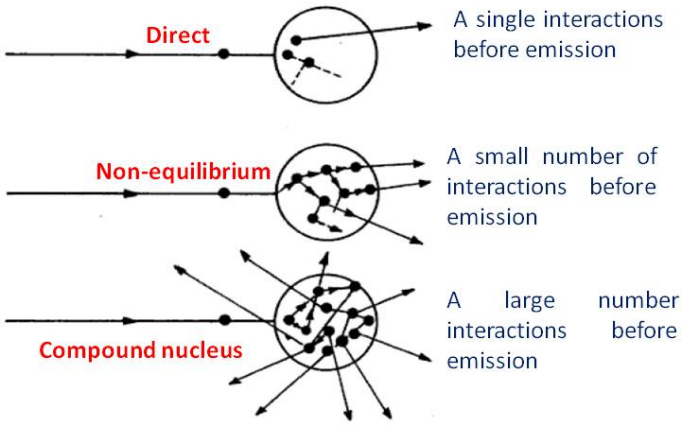

Figure 1.1: The three models of reaction mechanism i.e. the direct, pre-compound and compound nucleus interaction are shown [7].

heavy ion collision and related reaction dynamics at low energy regime only ($E_{beam} \leq$ 15MeV/nucleon).

During a projectile-target interaction, either of the two possibility may occur (i) the projectile may be deviated by the potential of target nucleus, resulting in change of its direction without the change in the center of mass energy. (ii) the projectile may interact with the target nucleus, passes its energy and get absorbed by the target nucleus. Succeeding interaction process, nuclear reaction can be proceeded via different mechanisms such as direct reaction [8], compound nuclear reaction [9] or by some non-equilibrium processes [10], a pictorial display of these processes is shown in Fig. 1.1.

(i) Direct reaction or peripheral reactions: They proceed directly from incoming channel to exit channel without the formation of intermediate state (compound nucleus) and involve a few available degrees of freedom for interaction. In these reactions, the projectile interacts with the target nucleus through one or more nucleon(s) and after single interaction both of them are ejected. Such nuclear process involve elastic and inelastic nuclear collisions, stripping and the pick-up reactions,

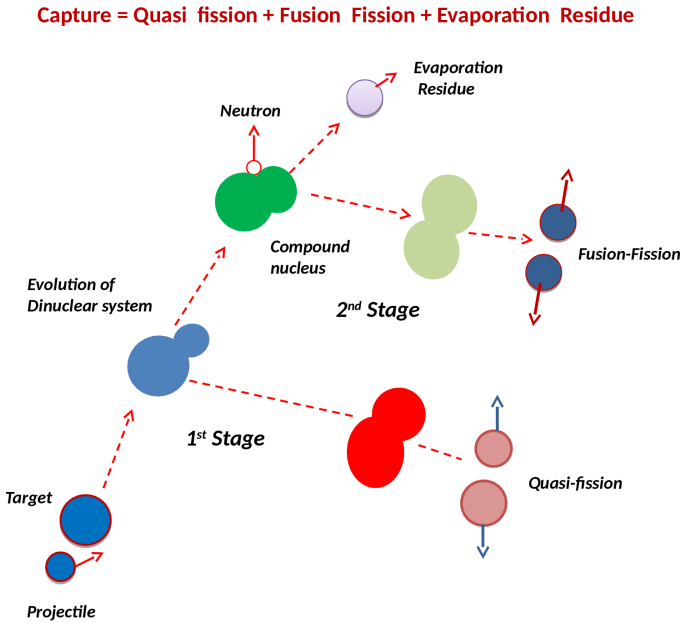

Figure 1.2: Two possible ways through which projectile and target interacts giving rise to compound nucleus (stage 2) and non-compound nucleus phenomena (stage 1).

observed predominately at relatively high energies.

(ii) Compound nucleus (CN) process: Here the incident particle interacts with a large number of nucleons and redistributes its energy among them. As a result of this, some nucleons or a group of nucleons gather adequate amount of energy and get acquitted after multiple interactions. This mechanism denotes as compound nucleus process and is shown as II stage in Fig. 1.2. This figure depicts that, when projectile interacts with target through its energy E and angular momentum ℓ, a di-nuclear system (DNS) is formed, as a first step. Subsequently, the evolution of DNS take place by means of nucleon displacement and/or transformation of energy resulting into formation of mono-nuclear system. Which subsequently emerges to equilibrated compound nucleus.

(iii) Non-equilibrium process: These reactions involve interaction of projectile with two to five nucleons of target which may further interact with other nucleons and hence is considered neither a direct nor a compound nucleus process. Basically such reactions are characterized by emitting a particle long before the attainment

of compound nucleus formation, thus treated as non-compound nucleus (nCN) phenomena. Similar to CN reactions, the nCN processes also provide much needed information about the nuclear structure and the reaction dynamics. In subject to the beam energy, entrance channel mass asymmetry and nature of projectile used, the processes like deep-inelastic collision (DIC), quasi-fission (qf), fast-fission(ff) and incomplete fusion (ICF) etc. come into picture. In DIC, the projectile and the target nuclei cohere for adequate period of time and dissipate substantial amount of energy, whereas the surfaces of the colliding nuclei overlap for a limited time. In this process, the product mass is close to the mass of reactant nuclei and generally observed for systems in which charge product Z_1Z_2 (Coulomb force) of entrance channel is higher. Quasi-fission is a process in which the DNS disengage before attaining equilibrium position, giving target and projectile like products in the exit channel. It occurs at an initial phase of the collision when two fragments are linked by a neck and nucleon start shifting from the heavy fragment towards the lighter one. Like DIC, the probability of qf process to occur also depends on the Coulomb interaction of colliding nuclei along with the deformation of reaction partners. The qf process is shown in Fig. 1.2 as I stage. Fast fission (ff) predominately occur at higher energies. In this process, due to the large angular momentum, the fission barrier vanishes and system re-separate before reaching equilibrium.

In general, direct, CN and non-equilibrium reactions can be distinguished according to the reaction time scale, and the degree to which the kinetic energy of the projectile is converted into internal excitation of the final products. Although, at some stage, the reaction time scale of direct and CN reactions become comparable and it becomes difficult to differentiate between them. At low incident beam energy, the compound nucleus or complete fusion reactions [9] survive for a longer duration and hence impart useful information regarding the dynamical behavior of colliding and emission partners. In this thesis, an extensive analysis relating the compound nuclear dynamics is worked out. The detailed information regarding the formation and corresponding decay mechanisms of compound nucleus are discussed below.

1.2 Compound nucleus formation and subsequent decay mechanism

Complete fusion is a process in which a composite system is formed after amalgamation of target and projectile giving rise to the formation of fully equilibrated compound nucleus (CN). In 1936, Bohr visualized a classical picture of compound nucleus reaction as (i) union of colliding nuclei into a single unit called as "formation of compound nucleus", with life span of $\sim 10^{-15}$s and (ii) the disintegration of CN into the products of the reaction. During the former stage, the target nucleus capture the incident particle, followed by the division of excitation energy and angular momentum among all the nucleons of the equilibrated compound system. Because of redistribution of energy, the decay of the CN retains no memory of its creation and provide a rather uniform angular emission of particles, thus the processes of formation and the break-down of compound nucleus are completely independent of each other. The time scale of compound nucleus is larger than the time required by a nucleon to cross over a nucleus ($\sim 10^{-23}$s), leading to the statistical equilibrium. Long after the capture process, particles emissions takes place following statistical process just as the evaporation of molecules from a liquid droplet.

The Bohr independence hypothesis implies that, the decay of a compound nucleus is determined rigorously by its quantum mechanical properties such as excitation energy, parity and angular momentum but independent of the entrance channel from which it was formed. A schematic view of formation and decay of compound nucleus is displayed in Fig. 1.2 (stage II). The figure depicts that, because of immense excitation energy and rotational momentum, the excited compound nucleus (CN) further de-excites with times into two main mechanisms. The first one is the emission of multiple light particles (LPs) also known as evaporation residues (ER) i.e. *n, p,* α, γ-rays and secondly into fission (A/2$\pm$20). However in some cases, intermediate mass fragments (IMFs) called as clusters or complex fragments

contributes, lying within the range of $5 \leq A \leq 20$ ($2 < Z < 10$) and the heavy mass fragments HMFs (mass in-between IMF and fission). The probability of IMF and HMF decay is observed to be significant for few nuclear systems but LPs and fission are the main contributors towards the fusion excitation functions at low energy range. In 1950 Ghoshal [11] provided the first experimental evidence in support of the Bohr independence hypothesis by investigating the decay of $^{64}Zn^{*}$ compound nucleus formed through different entrance channels, using a beam of α particle and proton. This study was further cemented by Smith [12]. Later on J. R. Grover and R. J. Nagle [13] demonstrated that, to validate the independence hypothesis thoroughly, angular momentum effects must be accounted adequately. In quest of this, D'Auria *et al.* [14] performed an experiment with the beams of heavy ion such as ^{12}C and ^{16}O, as HIR provide an excellent inquisition for extensive study of compound nucleus reactions with angular momentum effects, which under favorable conditions, support the Bohr independent hypothesis.

With an aim to correlate the experimental observations with conceptual grounding, Bethe, [15] and Weisskopf, [16] were the first to develop a theoretical model to study the compound nuclear decay by calculating the average neutron cross sections and light particle (*n, p,* α) evaporation using the partial wave technique (the discussion about the nuclear cross-section and partial wave technique is outlined in next section). The limitation of this model find its basis in non-conservation of the parity and angular momentum for each particle wave, though it still presents a good estimate of the cross-section magnitude. Subsequently, in 1952, Hauser and Feshbach [17] rectified this problem in more detailed way by explicitly taking angular momentum and parity into account for certain reactions. Further, in subject to investigate the dynamics involved in formation and decay processes of compound nucleus, numerous quantum mechanical hypothesis have been established.

In the recent past, various statistical approaches are developed to study above mentioned particle emission and other decay processes. The light particles LPs

emission is best understood by Hauser Feshbech (HF) [17] analysis (eg: PACE code [18]). However its other version is used to understand the production of IMFs/HMFs/fission, like extended Hauser-Feshbach Scission point Model [19] or BUSCO code [20] are used for 2<Z<10 fragments. In addition to this, some other fission models [21] are employed for A<80 nuclei. These models are either based on the scission or saddle-point configurations [22], or the saddle-point transition-state model (TSM) [21, 23–25]. Whereas for A>100 GEMINI code based on Moretto's fission model [26] is used. Both HF analysis and Fission Models considered the ER, IMF, HMF and fission processes separately, in spite of the fact that, the fission and cluster decay are competing processes with later being more frequent for light fragments [27]. An alternative approach to statistical models is provided by Gupta and Collaborators known as Dynamical Cluster-decay Model (DCM) [28–31] based on the Quantum mechanical fragmentation theory (QMFT) [32] and treats all possible decay processes on equal grounding. Thus, in DCM, the emission of both the ER and fission are treated as the collective mass motion of preformed clusters through the potential barrier. Another interest of using the DCM over statistical models is that, CN structure effect can be extracted via the preformation probability of the fragments that is absent in the other statistical based approaches. In addition to DCM, to address compound nucleus fusion process, the Wong formula [33] and its extended version ℓ-summed Wong formula [34] are employed.

1.3 Nuclear cross-section within partial wave analysis

For unmitigated conception of compound nuclear mechanism and to understand the numerous applications in the field of nuclear energy, astrophysics, and national security; many area of applied and basic nuclear physics require nuclear reaction cross-sections. Cross-section is the meeting ground between the theory and the

experiment. The nuclear cross section is defined as the probability of occurrence of a particular reaction, or in physical terms, this concept can be assessed as the "characteristic area" where a larger area designates greater interaction probability. Experimentally one can only measure the rate through which certain reaction takes place (event/second) under required conditions such as incident particle energy, angle of deviation etc. The nuclear cross section is denoted as 'σ' and measured in standard unit 'barn' (one barn equals to 10^{-28} m^2 (or 10^{-24} cm^2)). In case when these cross-sections can not be predicted reliably or measured directly, then some indirect technique such as 'Surrogate method' may be employed.

One can measure the nuclear cross-section microscopically or macroscopically. The microscopic cross section characterize the effective part or section (area) of isolated target nucleus, whereas the macroscopic form depicts the effective target area of all nuclei with in certain volume. It means that, the probability of interaction of a neutron/proton/heavy ion with a target nucleus also depend on the density of nuclei within that volume. Primarily the nuclear cross-sections are categorized in 'partial' and 'differential' forms. Partial cross-section represents the contribution from several independent and/or distinct processes which can remove particles from the incident beam. These partial contributing cross-sections can be further separated into different contributing parts *i.e.* total cross-section (σ_t) equals to the sum of cross-section that produces measurable scattering σ_{sc} and the reaction cross-section σ_r; so that σ_t=σ_{sc}+σ_r. However in differential form, the distribution of emitted particles is measured with respect to the solid angle (dσ/dω). These differential cross-sections are then integrated over all space to give total reaction cross-section, also called an integrated cross-section.

Theoretically speaking, one of the most acceptable method for measurement of cross-section is the 'partial wave' (PW) method. This method has been applied in various fields such as acoustic, quantum mechanics and optics etc. The technique of PW was initially adopted by British Physicist 'Rayleigh' for the sound

wave scattering [35] and later used by Faxen and Holtsmark to the scattering of Schrodinger wave. To extract the physics involved in certain scattering/collision or in cases where effects of interference are predominant, Partial Wave Analysis (PWA) is a useful mathematical tool to understand all such problems. Quantum mechanically, partial wave analysis is a method or technique for resolving scattering problems via decomposing each wave into its constituent angular momentum element (or component) and then solved using boundary conditions. In PWA, the potential is considered to be spherically symmetric $V(\overrightarrow{r}) = V(r)$, as a result of this, the angular momentum of the incoming projectile is conserved, for the reason that, in central potential, the angular momentum (ℓ) of scattered particle is same before and after the collision (Noethers theorem). Therefore, one can expand a wave function in the eigne-states of the angular momentum, consequently resultant waves with definite 'ℓ' are called partial waves.

In case of CN reactions, the complete fusion cross-section is obtained by measuring ER, IMFs and fusion-fission (ff) cross-sections: $\sigma_{fus}=\sigma_{ER}+\sigma_{IMF}+\sigma_{ff}$. Therefore following above, to estimate the formation and the decay cross-sections, in this thesis, partial wave method is adopted both in Wong and dynamical cluster-decay approaches.

It is observed that, the probability of interaction also influenced by the shape and orientation of interacting nuclei, the detail of which is discussed in the upcoming section.

1.4 Nuclear deformation and orientation effects

The role of nuclear deformations has been continually probed to analyze both the fusion and decay paths involved in heavy ion induced reactions (HIRs). For a better description of nuclear reaction dynamics, deformations play significant role and have always been a matter of resurgent interest during last few decades. In 1935, Schuller and Schmidt [36] were first to probe the shape of nucleus through nuclear electric

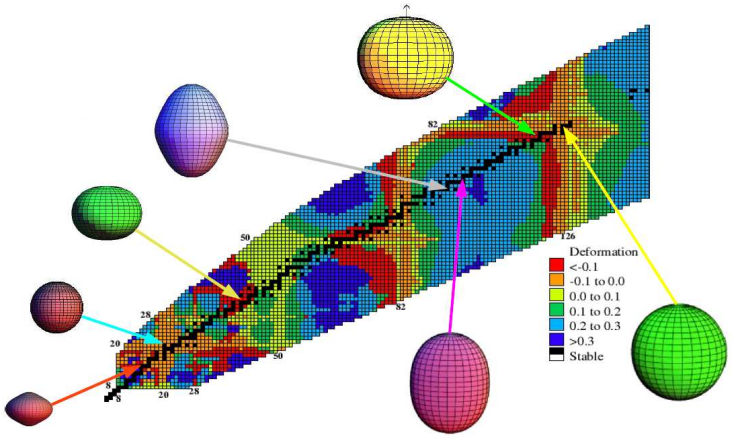

Figure 1.3: A chart showing the theoretical quadrupole deformation of approximately 2000 nuclide calculated by Möller [38].

quadrupole moment (Q) from hyperfine structure in atomic nuclei, before that nucleus was considered to be spherical with symmetric charge distribution. Depending on the properties of each nuclei, they come in various shapes such as quadrupole deformed (β_2), octupole deformed (β_3) and hexadecapole deformed (β_4) nuclei. The sign of quadrupole deformation (β_2) , extracted from Q, tell us the exact shape of nuclei as $\beta_2>0$ corresponds to elongated (cigar-like prolate) shape and $\beta_2<0$ refers to flattened (oblate) shape nuclei [37]. The Octupole deformation gives the nuclear pear like appearance and define the reflection-asymmetry in the nuclear shape. It is found that majority of deformed nuclei have prolate shape, while very few exist with oblate structure as depicted in a chart presented in Fig. 1.3 [38]. For more than half a century, this preponderance has taken a lot of attention of nuclear physicists and presented a challenge in the understanding of nuclear structure physics [39]. Subsequently a detailed study of intrinsic electric quadrupole moments provided by experiment [40] has confirmed the predominant occurrence of prolate shape nuclei.

Beside above discussed nuclear shapes, some of nuclei be found with superdeformed and hyperdeformed states but are very few in numbers. Macroscopically, these nuclear shapes are not just as true hard shapes, but are rather described by

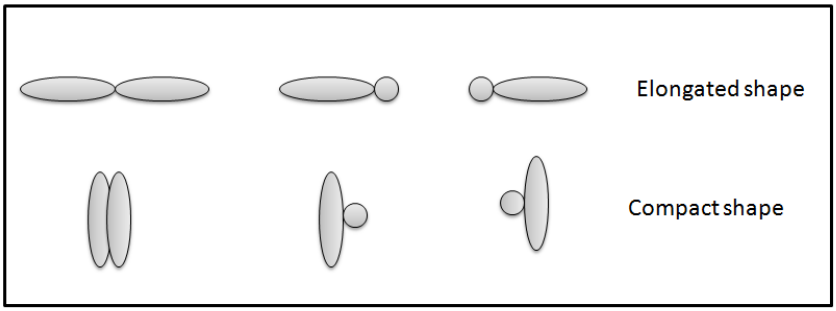

Figure 1.4: Schematic diagrams for the interaction of spherical and quadrupole deformed (prolate and oblate) nuclei giving elongated and compact shapes.

their mean field and density.

When the nuclear deformations are included, the consideration of orientation degree becomes unavoidable [41]. In early 1980s, the study of deformation and orientation was investigated by Greiner [42] via considering the collision between ^{238}U+^{238}U and suggested that only a peculiar orientation of Uranium nucleus could give a very long lived ($\sim 10^{-20}$s) giant molecule. A detailed study of deformation and related orientation is required at both theoretical and experimental level to understand more about the distinctive features of heavy-ion induced reactions involving deformed nuclei. When a deformed nucleus is in ground state, it can be oriented in many ways and each type of configuration of colliding nuclei leads to separate fusion barrier. About a decade ago, a comprehensive analysis was done by Gupta *et al.* [41], in which fixed (optimum) orientations were suggested for each pair of quadrupole deformed (prolate or oblate) or spherical + β_2-deformed colliding nuclei, that may have different signs (+/-) of β_4-deformation. The optimum orientations are suggested for cold, non-compact (elongated) fusion configuration corresponding to lowest barrier/largest interaction radius and for hot, compact fusion configuration with the highest barrier/smallest interaction radius as shown in Table 1 of Ref. [41]. The schematic view of elongated and compact shapes is depicted in Fig. 1.4. The compact configuration is used for nuclei with higher multipole deformations particularly for positive hexadecapole deformations. In recent past notable amount of work

has been done to address the importance of deformations and related orientations by studying various nuclear systems formed in HI reactions [43–45], which eventually show inevitable influence on fusion-fission and other competing decay channels. It is noted that, in the absence of deformation and orientation effects, the decay profile of CN show symmetric mass distribution, on the other hand, on allowing deformation effects, asymmetric fragmentation path is obtained [31]. The ground state deformations are generally obtained from the work of [38] and their effect on the decay path of various nuclei from low to heavy mass region (A=70-220) is discussed in subsequent chapters. In order to address nuclear reaction dynamics one may also proceed via static as well as dynamical (temperature dependent) deformations. In past some effort have been made in this direction, but still there is immense need to investigate this issue as different nuclei of different mass/shell region exhibit distinct behavior over a wide range of incident energy.

At low incident energy, the phenomena like fusion, fission, elastic and inelastic scattering etc. cannot be described without an accurate knowledge of nuclear interaction potential. The determination of the interaction potential between two nuclei is a difficult quest and endless efforts are being made in this direction. In the present work, different approaches are employed to estimate the nuclear interaction potential as discussed below.

1.5 Interaction potential

Our perception of the fusion reactions between the strongly and weakly bound nuclei have been refined due to the relentless efforts devoted by the nuclear physics community in the area of theoretical [46–55] and experimental research [56–60]. For the successful occurrence of a particular fusion reaction, its interaction potential plays an important role. When two nuclei come together, they feel a long range electrostatic Coulomb force of repulsion by virtue of their charges in addition to short range attractive nuclear force. The interplay among these forces form a in-

teraction/fusion barrier with an appropriate fusion pocket. The interaction barrier denotes the energy where the barrier penetrating probability is one-half for the s-wave. At low energy, the formation (or decay or both) of system is also stimulated by the repulsive centrifugal potential which originates owing to rotational motion of system and depend on the contributing angular momentum and moment of inertia involved. The effect of this repulsive part is to intensify the fusion barrier height, thereby making fusion pocket shallower. It implies that an accurate knowledge of the interaction potential is highly desirable for an extensive study of the heavy ion reaction dynamics.

In interaction barrier and pocket formation process the short range part plays major role as suggested by Holm and Greiner [61] and later by Wong [62]. To describe the nuclear interactions at both microscopic/macroscopic level, the theoretical models perform extremely constructive role. In recent years, a vast number of theoretical models have become available to explain different features of fusion dynamics. The most commonly used two approaches for estimation of ion-ion interaction potential are macro-microscopic and analytical methods as discussed below. A schematic of both kinds of the nuclear interaction potentials is shown in Fig. 1.5.

1.5.1 Energy Density formalism (EDF)

In macro-microscopic methods [63–65], the asymmetric two center shell model [66] and other mean field calculations [67,68] have been used comprehensively to investigate the behavior of nuclear interaction potential. For the microscopic interpretation of nuclei, the energy density functional (EDF) method [69–73] is the best theoretical tool usually quoted as "self-consistent mean-field and beyond-mean-field methods". Although the empirical reconstruction of such method required Hamiltonian based approaches and explicit wave-function. The EDF is established from a theorem proposed by Hohenberg and Kohn [74]; and Sham and Kohn [75], originally manifested for an electron gas. Further, its elementary extension is made for more complex

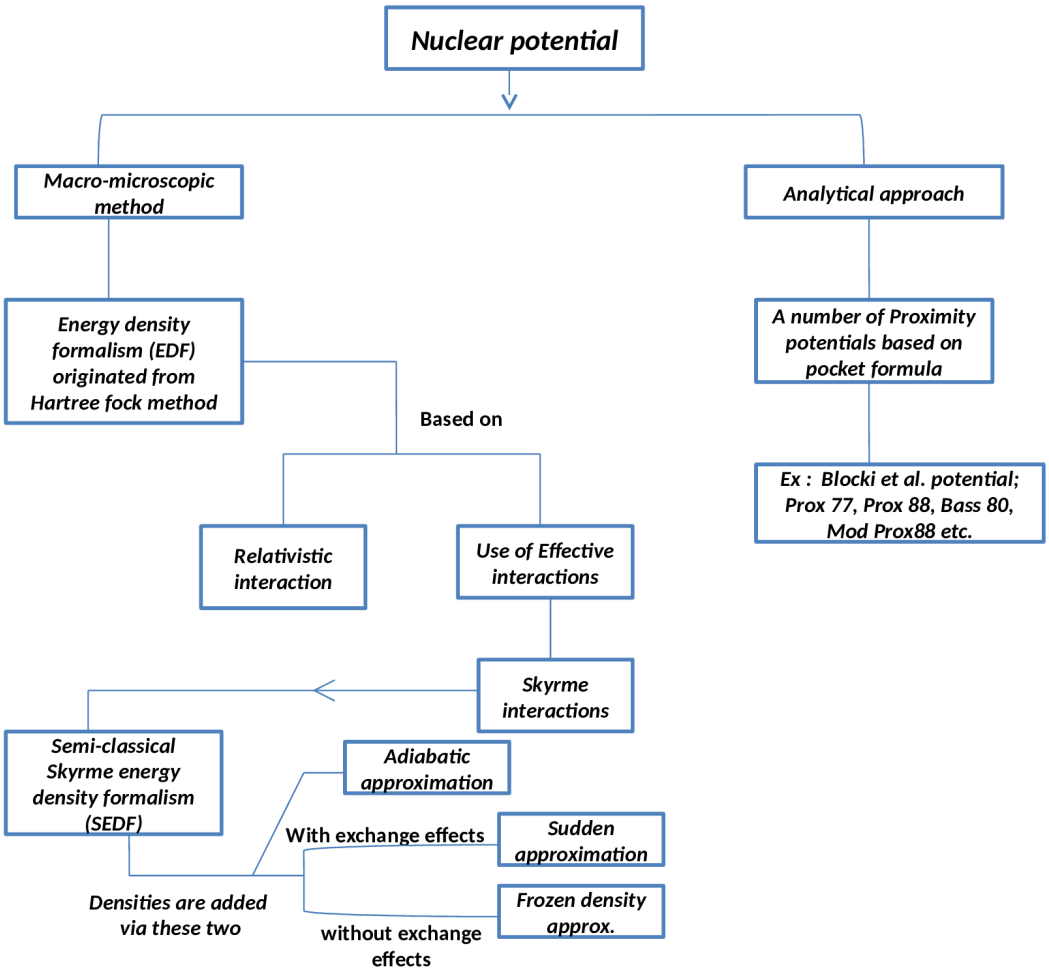

Figure 1.5: A schematic presentation of different forms of nuclear interaction potentials.

fermion systems, which says that, the total energy of fermions in its ground state can be inscribed in the form of local density and its derivatives. This approach is very appealing in nuclear physics as it reduces the tricky expressions of the many-body problem into a simpler form of Lagrangian formalism. However, the difficulty lies in the fact that, there is no way of calculating a lagrangian initially. As a result of this, yet the functional should be unique, but some recipe has to be followed to approximate it. Such kind of inconsistency encountered here is alike in selecting an effective interaction imitating the actual G-Matrix to be operated in Hartree-Fock calculations.

Depending on the non-relativistic or a relativistic scheme, EDF is a single consistent frame designed to provide complete and detailed description of specific nuclei.

It also gives estimation in the region of the nuclear chart where experimental data are inaccessible. Moreover, it is a convenient way to ingress the problems related with the infinite nuclear matter system such as neutron stars. One can work within EDF using two distinct groups; the first associated with the realistic nucleon-nucleon interaction, exercised to solves the Bethe-Goldstone equation in momentum space as a consequence of this, the resulting energy density is complex with both the real and the imaginary parts, and presents strenuous numerical problems. The second group makes use of an effective nucleon-nucleon interaction like the Skyrme interaction to obtain the energy density that is real within the Hartree-Fock approximation. The latter approach is usually applied to calculate the nucleus-nucleus potential [69, 70, 76, 77] due to mathematically simpler structure of it. This formalism was first adopted by Vautherin and Brink (VB) [78] in order to study the ground state properties of spherical nuclei derived from Skyrme interaction [79] and enjoy special popularity because of its achievement in predicting properties of each nuclei. The VB energy density is expressed in the form of the kinetic energy density (τ), nucleon mass density (ρ) and the spin density (J). The full Hartree-fock (HF) calculations were not possible in energy density formalism due to non availability of adequate 'τ' terms at Hartree-fock level. This problem was further rectified by Grammaticos and Voros [80], who introduced the semi-classical approaches such as Thomas-Fermi (TF) method or its extension the Extended Thomas Fermi (ETF) used for obtaining Kinetic energy expression of the compound system. With the help of semi-classical approaches, the total energy of the nuclear system become a function of the nucleon density only. The Hamiltonian considered by Grammaticos and Voros (GV) in [80] does not contain any spin dependent term, though, it is well known that, in order to give better description of nuclear properties, the single-particle nuclear Hamiltonian must include a spin-orbit part which comes into picture after the success of Shell-Model. Consequently, to include the spin-orbit part, an extension of GV work was made in [81] by extending the semi-classical expansions

to the realistic case where spin-orbit density dependent terms are accounted in the effective one-body Hamiltonian. In semi-classical approach, the spin-orbit density (J_q) depends on nucleon density as a result of this, J_q is non-zero for nuclei with completely filled shell, which is not the case in microscopic shell model approach where J_q=0 for such nuclei.

In view of above, in this thesis, I shall use the energy density formalism given by Vautherin and Brink based on Skyrme interactions (discussed later in Sec. 1.5.2) within semiclassical ETF approach. The interaction potential obtained by EDF is usually calculated under two extreme physical assumptions: (a) **Adiabatic approximation**: this approximation works suitably if the time of collision of nuclei is larger than the relaxation time so that at each stage of collision the nucleons of two ions take up the symmetric configuration. (b) **Sudden density approximation**: this approximation is appropriate for the reactions where the time of collision is much less than the relaxation time as a result of that nuclear density overlaps without changing their shapes. The sudden densities due to anti-symmetrization can be defined without or with exchange effects, and the one without exchange effects is named as frozen density approximation [82]. In the frozen density approximation, nucleon density ρ_q, kinetic energy density τ_q (q=1,2 for target and projectile) and spin-orbit density J_q are assumed as the sum of the corresponding densities of the projectile and target nuclei. Whereas in sudden approximation spin-orbit density and kinetic energy density are expressed as a function of nucleon density, which corresponds to the sum of density of target and projectile. Though both sudden and frozen approaches can be applied in EDF, but recent analysis [83] on some Ni- and Ca-based medium to superheavy mass region reactions suggest that, fusion barriers obtained under frozen approximation are more realistic than sudden approximation. Moreover, the barrier are formed at all angular momentum states and orientation angles when frozen density is used, which is not true for sudden approximation. In view of this, the present work is carried

out in the framework of frozen density approximation.

1.5.2 Skyrme Interaction

Nuclei are the many body systems containing large number of nucleons such as proton and neutron. However, in the path to understand the interaction between these particles, we faced certain complications originated due to the posterior issues (a) as a quantum many body system, large number of degrees of freedom of nucleus were not considered in the thermodynamical and statistical approaches. The finiteness of a nucleus was expected to play important part in the description of associated properties (b) the nuclear force which plays determinant role in determining nuclear properties is not that established in comparison to electromagnetic interactions. Therefore to overcome above issues, suitable approximations are needed. In the past three decades, for microscopic description of nucleon-nucleon interaction, some mean field models such as Skyrme-Hartree-Forck scheme (SHF) [84], the Gony force [85] and relativistic mean field force (RMF) [86] are commonly accepted. These effective forces are fitted phenomenologically because of the insufficient understanding from nuclear many body theory. In such phenomenological forces, about seven to ten adjustable parameters are good enough to describe the ground state properties of many stable elements from ^{16}O to the heaviest nuclei. Among different phenomenological forces, the Skyrme interaction [79], a non-relativistic approach is a topic of present interest. It is a conventional force with many adjustable parameters applied to study the heavy-ion reactions from low to intermediate energies. In 1950, Tony Skyrme proposed an effective nuclear interaction that was expected to occupy the crucial features of in-medium interaction. Since the pioneering work of [78], the Skyrme interaction has become famous for the absolute depiction of nuclear properties based on a self-consistent mean-field approach. Originally, standard Skyrme effective force (SSEF) [78, 87–89] consists of zero-range central, density-dependent and spin-orbit terms with 11 parameters. The SSEF performed successfully in a

ample range of the nuclear chart, however as one move away from the valley of β-stability, some nuclear properties couldn't be precisely reproduced. To remove this inadequacy, continuous modifications and generalization to the SSEF were suggested by adjusting the nucleon effective mass m^* and incompressibility factor K, and new set of Skyrme force parameters were set up [90] now called as generalized Skyrme effective forces (GSEF) [90–92]. Later on various Skyrme forces were made available by prolonged efforts [92–94]. Reinhard and Flocard [95] has modified spin-orbit term by adding extra spin-orbit coefficient $W_0^{'}$ and gave five parametrization named as SkI1 (W_0=$W_0^{'}$), SkI2 (W_0=$W_0^{'}$), SkI3 ($W_0^{'}$=0), SkI4 ($W_0 \neq W_0^{'}$) and SkI5 (W_0=$W_0^{'}$) Skyrme forces. Intense work has been devoted to improve the existing parameterizations, in particular considering additional terms in the standard form. B. K. Aggarwal *et al.* [92] has introduced six additional parameters in density dependent term of Hamiltonian, fitted by some specific characteristics of normal and isospin-rich nuclei. Until now these interactions have been successfully and extensively used to study the nuclear reaction dynamics including nuclear structure, fusion hindrance [96] and fusion-fission [97,98] at low energy. Till date, we have vast variety of Skyrme forces, which provide a wide spectrum of barrier characteristics. In the present thesis, different Skyrme forces are applied to address the experimental data in vicinity of the barrier, where fusion hindrance and related nuclear phenomena come into picture.

1.5.3 Analytical methods

Several attempts have been made to give simple and optimized form of nuclear potential. The nuclear proximity potential [99] is widely accepted to address the surface interaction effects of colliding/decaying nuclei. This phenomenological potential uses a simple analytical expression for obtaining the nuclear interaction potential and is extensively applied to address fusion-fission dynamics. It was first adopted by Bass [100, 101] for calculation of nucleus-nucleus interaction potential. Similar effort

were done by Blocki *et al.* [99], who introduced a formula for calculating potential as a function of separation distance of two interacting nuclei, which is popularly known as Blocki pocket formula [99]. All the proximity potentials arise from the proximity forces, based on generalized theorem given by Deryagin [102]. It states that, If two gently curved objects or surfaces are put intently, then the force acquired by them will be equivalent to the interaction potential per unit area among two flat surface(s) designed from the same material. The proximity potentials are expressed as a product of geometrical factor and a universal function. Over the years, many refinements and modifications have been made through the surface energy coefficients or via nuclear radius [103,104]. With the passage of time, various methodologies are developed which give wide range of barrier characteristics to address fusion fission and related aspects of heavy ion reaction mechanism. In this thesis, Blocki *et al.* potential is used to study the dynamics involved in compound nuclei formed via HI induced reactions.

1.6 Motivation of the present work

In this thesis, we investigate the heavy ion collision and related dynamical aspects at low energy region (E $\leq$ 15 MeV/nucleon) using the Wong formula and dynamical cluster decay model. The main emphasis is to address the formation and decay pattern of various nuclear systems by examining the problems related to following aspects: (i) Effect of entrance channel, mass asymmetry, excitation energy and deformations etc. in heavy ion reaction dynamics. (ii) Comparative analysis of phenomenological and microscopic interaction potentials in nuclear reaction dynamics. (iii) Influence of centrifugal potential via sticking and non-sticking moment of inertia. (iv) Comparison of theoretical results with available experimental data and effort to make possible predictions for future experiments. To carry out the study, various compound nuclei and their isotopes such as ^{200}Pb*, ^{86,88,90,92}Zr*, ^{76}Kr*, ^{108,110}Sn*,

^{214,216}Rn*, ^{72}Se* and ^{56}Ni* are considered.

The detail description of the theoretical work presented in this thesis is discussed in chapters 3-6.

1.7 Organization of the Thesis

The thesis is organized as follows:

In **Chapter** 2 an extensive detail of nuclear models used to carry out the present work is discussed. Wong formula is employed to describe the fusion process and the dynamical cluster decay model (DCM) based on collective clusterization approach is applied to address the decay process of various compound nuclei. DCM has the advantage to treat various decay processes *i.e.*, ER, IMF and fission fragments on same grounding. The detail of nuclear potentials; obtained from the proximity theorem and other using Skyrme energy density formalism of Vautherin and Brink is also reported.

In **Chapter** 3, it is intended to analyze the entrance channel dependence in view of ^{16}O+^{184}W, ^{19}F+^{181}Ta and ^{30}Si+^{170}Er reactions, addressed respectively using Wong and DCM approach. The calculations are carried out using with both the spherical and quadrupole (β_2) deformed choices of nuclei. It is observed that, the Wong formula overestimates the data for ^{19}F- and ^{30}Si- induced reactions, however underestimate excitation function of ^{16}O-induced reaction. While its extended version, *i.e.* the ℓ-summed extended Wong model, fits the experimental fusion cross-section nicely for the ^{19}F+^{181}Ta and ^{30}Si+^{170}Er channels, however inadequate to address the fusion data at few energies of ^{16}O+^{184}W reaction. The underestimation of data persists even after inclusion of deformation effects and might be associated with the contribution of non-compound nucleus (nCN) process. This lead us to conclusion that, the formation of ^{200}Pb* compound nucleus seems to depend on the choice of incoming channel. Apart from this, entrance channel effects are further

explored in the decay path of ^{200}Pb* using DCM. An interesting result is that, although, the overall decay pattern of compound nucleus ^{200}Pb* seems similar for all the chosen reactions though some signature of variation are observed in fission and intermediate mass fragment (IMF) region for the deformed fragmentation process, there by suggesting that the deformation and orientation of decaying fragment are equally important in formation as well as in the decay process of proton magic nuclear system ^{200}Pb*. In addition to this, ER and fission cross-sections are predicted within comprehensive energy range from 98 MeV to 128 MeV, an experimental verification is called for predicted cross-sections. Along with this, the dynamics involved in neighboring isotopes of Pb *i.e.* ^{192}Pb* and ^{202}Pb* is also investigated.

In **Chapter** 4, the decay of even mass $^{86-92}$Zr* isotopes is studied in order to observe the iso-spin and deformation effects. It is observed that the fragmentation path of all Zr nuclei gets influenced with inclusion of deformation effects. Also, the entrance channel independence is inspected in ^{92}Zr* and ^{76}Kr* systems both formed via $^{16,18}O$-induced reactions. We further aimed to analyze the role of projectile mass in the dynamics of spherical magic ^{108,110}Sn* compound systems.

In **Chapter** 5, the relative effect of sticking and non-sticking limits of moment of inertia is investigated in reaction dynamics of ^{214,216}Rn* compound nuclei formed respectively via ^{16,18}O+^{198}Pt channels. The role of different limits of moment of inertia is examined on both spherical as well as deformed choice of fragments by studying barrier characteristics and preformation probabilities of considered compound systems. It is observed that, the barrier height (and corresponding position) and the preformation paths of chosen systems change significantly while going from I_{NS} to I_S approach and also depend on the deformation and orientation of nuclei. The DCM calculated ER cross-sections find nice agreement with experimental data within both the sticking or non-sticking limits of interaction. This is true for spherical as well as deformed choice of fragmentation. Whereas, ff data is fitted within I_S limit only specially after inclusion of higher order deformations. Further, within

DCM, the ER survival probability of ^{214,216}Rn* compound nuclei is calculated and it is confirmed that ^{216}Rn* system with N=130 has greater stability against fission as compared to ^{214}Rn* nucleus with N=128. Also the ff cross-sections are predicted for ^{214,216}Rn* nuclei within sticking limit of moment of inertia as the same seems to be more preferable for emission of heavy fragments.

In **Chapter** 6, we have examined the role of deformations and orientations on spin-orbit density dependent potential, obtained via the Skyrme energy density formalism (SEDF). For the purpose, $^{24-54}$Si+^{30}Si reactions are considered with spherical target ^{30}Si and projectiles $^{24-54}$Si having prolate and oblate shapes. The calculations suggest that, Si-nuclei with β_2 <0 form most compact configuration at $(0^0, 180^0)$, which further changes to $(90^0, 180^0)$ for nuclei with β_2 >0. Furthermore, the possible role of spin-orbit potential is tested on barrier characteristics and fusion cross-sections. Beside this, the effect of spin-orbit density dependent (V_J) and independent (V_P) part of nuclear interaction potential is explored on various entrance channels ^{23}Na+^{49}V,^{25}Mg+^{47}Ti,^{27}Al+^{45}Sc,^{29}Si+^{43}Ca and ^{31}P+^{41}K, forming ^{72}Se* compound nucleus and on N/Z ratio of Se isotopes. Also, the role of double spin-orbit parameter (W_0 and W_0') is explored on two nucleon transfer reactions in view of SkI2, SkI3 and SkI4 Skyrme forces. The decay of ^{72}Se* nucleus formed in ^{27}Al+^{45}Sc reaction is also explored within DCM, using both SEDF and proximity based pocket formula. Moreover efforts are made to address the fusion hindrance phenomena via barrier lowering parameter ΔV_B of DCM in agreement to experiment. The contribution of spin-orbit density dependent interaction potential is also estimated in ER excitation functions of ^{27}Al+^{45}Sc reaction using single (W_0) and double spin-orbit parameter (W_0 and W_0') Skyrme forces.

Finally, **Chapter** 7, summarizes the result of the work presented in this thesis along with possible extension for future prospective.

Bibliography

[1] E. Rutherford, Phil. Mag. **37**, 581 (1919).

[2] I. Tanihata *et al.*, Phys. Rev. Lett. **55**, 2676 (1985); I. Tanihata *et al.*, Phys. Lett. B **160**, 380 (1985).

[3] H. York, R. Hildebrand, T. Putnam, and J. G. Hamilton, Phys. Rev. **70**, 446 (1946).

[4] L. I. Bolotin *et al.*, Proc. Intern. Con. High-Energy Accelerators and Instrumentation, CERN, Geneva, 643, 644 (1959).

[5] A. Bohr and B. R. Mottleson, Nuclear Structure Vol. II: Nuclear Deformations World Scientiific ISBN 9810239807 (1998).

[6] M. G. Mayer, Phys. Rev. **75**, 1969 (1949); O. Haxel, D. Jensen, and H. E. Suess, Phys. Rev. **75**, 1766 (1949).

[7] Desalegn Ketema, 'Complete and incomplete fusion reactions in ^{16}O +^{93}Nb systems at various projectile energies', M.Sc thesis, Addis Ababa University, Ethiopia, (2013).

[8] S. T. Butler, Phys. Rev. **80**, 1095 (1950); S. T. Butler, Proc. R. Soc. A **208**, 559 (1950); N. Austern, S. T.Butler, and H. McManus, Phys. Rev. **92**, 350 (1953). ; J. R. Oppenheimer and M. Phillips, Phys. Rev. **48**, 500 (1935).

[9] N. Bohr, Nature (London) **137**, 344 (1936).

[10] K. Chen, G. Friedlander, G. D. Harp and J. M. Miller, Phys. Rev. **166**, 949 (1966).

[11] S N Ghoshal, Phys. Rev. **80**, 939 (1950).

[12] C. F. Smith, U. S. Atomic Energy Commission Document, University of California Radiation Laboratory Report No. UCRL-1182, (1965).

[13] J. R. Grover and R. J. Nagle, Phys. Rev. **134**, 31248 (1964).

[14] J. M. DAuriaM, M. J. Fluss, G. Herzog, L. Kowalski, M. J. Miller and D. C. Reedy Phys. Rev. **174**, 1409 (1968).

[15] H. A. Bethe, Phys. Rev. **50**, 332 (1936).

[16] V. F. Weisskopf and P. H. Ewing, Phys. Rev. **57**, 472 (1940).

[17] W. Hauser and H. Feshbach, Phys. Rev. **87**, 366 (1952).

[18] A. Gavron, Phys. Rev. C **21**, 230 (1980).

[19] T. Matsuse, C. Beck, R. Nouicer, and D. Mahboub, Phys. Rev. C **55**, 1380 (1997).

[20] J. Gomez del Campo, R. L. Auble, J. R. Beene, M. L. Halbert, H. J. Kim, A. Donofrio, and J. L. Charvet, Phys. Rev. C **43**, 2689 (1991); Phys. Rev. Lett. **61**, 290 (1988).

[21] S. J. Sanders, A. Szanto de Toledo, and C. Beck, Phys. Rep. **311**, 487 (1999).

[22] R. J. Charity, M. A. McMahan, G. J.Wozniak, R. J. McDonald, L. G. Moretto, D. G. Sarantites, L. G. Sobotka, G. Guarino, A. Pantaleo, L. Fiore, A. Gobbi, and K.D. Hildenbrand, Nucl. Phys. A **483**, 371 (1988).

[23] L. G. Moretto, Nucl. Phys. A **247**, 211 (1975).

[24] S. J. Sanders, D. G. Kovar, B. B. Back, C. Beck, D. J. Henderson, R. V. F. Janssens, T. F. Wang, and B. D. Wilkins, Phys. Rev. C **40**, 2091 (1989).

[25] S. J. Sanders, Phys. Rev. C **44**, 2676 (1991).

[26] L. G. Moretto, Nucl. Phys. A **247**, 211 (1975).

[27] R. K. Gupta and W. Greiner, Int. J. Mod. Phys. E **3**, 335 (1994).

[28] R. K. Gupta, in *Cluster in Nuclei*, Lecture Notes in Physics 818, Vol. I, edited by C. Beck (Springer-Verlag, Berlin, 2010), p. 223.

[29] K. Sandhu, M. K. Sharma, and R. K. Gupta, Phys. Rev. C **85**, 024604 (2012).

[30] M. Kaur, R. Kumar, and M. K. Sharma, Phys. Rev. C **85**, 014609 (2012).

[31] Rajni, R. Kumar and, M. K. Sharma, Phys. Rev C **90**, 044604 (2014).

[32] R. K. Gupta and W. Greiner, in *Heavy Elements and Related New Phenomena*, edited by W. Greiner and R. K. Gupta (World Scientific, Singapore, 1999), Vol. **I**, p. 397; *ibid* Vol. **I**, p. 536.

[33] C. Y. Wong, Phys. Rev. Lett. **31**, 766 (1973).

[34] R. Kumar, M. Bansal. S. K. Arun, and R. K. Gupta, Phys. Rev. C **80**, 034618 (2009).

[35] J. W. S. Rayleigh, The theory of sound vol. 2. New York: Dover publications (1945).

[36] T. Schüller and T. Schmidt, Z. Phys. **92**, 148 (1934); **94**, 457 (1935).

[37] P. Stransky, A. Frank and R. Bijker, J. Phys. Conf. Ser. **322**, 012018 (2011).

[38] P. Möller and J. R. Nix, Nucl. Phys. A **361**, 117 (1981).

[39] I. Hamamoto and B. R. Mottelson, Phys. Rev. C **79**, 034317 (2009); M. Horoi and V. Zelevinsky, Phys. Rev. C **81**, 034306 (2010).

[40] N. J. Stone, At. Data Nucl. Data Tables **90**, 75 (2005).

[41] R. K. Gupta, M. Balasubramaniam, R. Kumar, N. Singh, M. Manhas, and W. Greiner, J. Phys. G: Nucl. Part. Phys. **31**, 631 (2005).

[42] W. Greiner, *International NATO Advanced Study Institute (NASI) Course on Quantum Electrodynamics of Strong Fields*, Lahnstein 1981; M. Seiwert, N. Abul-Naga, V. Oberacker, J. A. Maruhn and W. Greiner, Gesellschaft für Schwerionenforschung (GSI) Annual Report 1981.

[43] G. Kaur, D. Jain, R. Kumar and M. K. Sharma, Nucl. Phys. A **916**, 260-274 (2013).

[44] M. Kaur and M. K. Sharma, Phys. Rev. C **85**, 054605 (2012).

[45] R. Kumar and M. K. Sharma, Phys. Rev. C **85**, 054612 (2012).

[46] R. K. Puri, R. Arora and R. K. Gupta, Phys. Rev. C **60**, 054619 (1999).

[47] R. Kumari, Nucl. Phys. A **917**, 85 (2013).

[48] C. Simenel, Eur. Phys. J. A **48**, 152 (2012).

[49] L. C. Chamon *et al.*, Phys. Rev. C **66**, 014610 (2002).

[50] C. H. Dasso, S. Landowne and A. Winther, Nucl. Phys. A **432**, 495 (1985).

[51] C. Simenel, M. Dasgupta, D. J. Hinde and E. Williams, Phys. Rev. C **88**, 064604 (2013).

[52] A. S. Umar, C. Simenel and V. E. Oberacker, Phys. Rev. C **89**, 034611 (2014).

[53] C. Simenel and B. Avez, Int. J. Mod. Phys. E **17**, 31 (2008).

[54] A. B. Balantekin and N. Takigawa, Rev. Mod. Phys. **70**, 77 (1998).

[55] H. Esbensen and S. Landowne, Phys. Rev. C **35**, 2090 (1987).

[56] J. J. Kolata *et al.*, Phys. Rev. C **85**, 054603 (2012).

[57] A. Pakou *et al.*, Phys. Rev. C **87**, 0146193 (2013).

[58] G. Montagnoli *et al.*, Phys. Rev. C **85**, 024607 (2012).

[59] J. R. Leigh *et al.*, Phys. Rev. C **52**, 3151 (1995).

[60] C. R. Morton *et al.*, Phys. Rev. Lett. **72**, 4074 (1994).

[61] H. Holm and W. Greiner, Phys. Rev. Lett. **24**, 404 (1970).

[62] A. S. Jensen and C. Y. Wong, Phys. Lett. B **32**,567 (1970); Nucl. Phys. A **171**, 1 (1971).

[63] H. J. Krappe, J. R. Nix, A. J. Swiatechi and A. J. Sierk, Phys. Rev C **20**, 992 (1979).

[64] P. Möller, A. J. Sierk and A. Iwamotto, Phys. Rev. Lett. **92**, 072501 (2004).

[65] T. Ichikawa, A. Iwamotto, P. Möller and A. J. Sierk, Phys. Rev C **71**, 044608 (2005).

[66] J. Maruhn and W. Greiner, Z. Phys. **251**, 431 (1972).

[67] V. Yu. Denisov and W. Nrenberg, Eur. Phys. J. A **15**, 375 (2002).

[68] A. Dobrowolski, K. Pomorski and J. Bartel, Nucl. Phys. A **729**, 713 (2003).

[69] K. A. Brueckner, J. R. Buchler, and M. Kelley, Phys. Rev. **173**, 944 (1968).

[70] D. M. Brink and Fl. Stancu, Nucl. Phys. A **243** 175 (1975).

[71] D. M. Brink and Fl. Stancu, Nucl. Phys. A **270**, 236 (1976).

[72] T. Izumoto *et al.*, Nucl. Phys. A **341** 319 (1980); ibid A **357** 471 (1981).

[73] A. Faessler *et al.*, Nucl. Phys. A **428** 271c (1984).

[74] P. Hohenberg and W. Kohn, Phys. Rev. **136**, 1384 (1964).

[75] W. Kohn and L. J. Sham, Phys. Rev. A **137**, 1697 (1967).

[76] D. Berdichevsky *et al.*, Z. Phys. A **327** 271 (1987).

[77] J. P. Blocki *et al.* Nucl Phys. A **459** 145 (1987); G-Q Li and G-O Xu, Nucl Phys. A **492** 340 (1989); G-Q Li and G-O Xu, Phys. Rev. C **39** 274 (1989); Li G-Q and G-O Xu, Commun. Theor. Phys. **11** 279 (1989).

[78] D. Vautherin and D. M. Brink, Phys. Rev. C **5**, 626 (1972).

[79] T. H. R. Skyrme, Phil. Mag. **1**, 1043 (1956); Nucl. Phys. **9**, 615 (1959).

[80] B. Grammoticos and A. Voros, Ann. Phys. **123**, 359 (1979).

[81] B. Grammoticos and A. Voros, Ann. Phys. **129**, 153 (1980).

[82] Li G -Q, J. Phys. G: Nucl. Part. Phys. **17** 1-34 (1991).

[83] R. Kumar, M. K. Sharma, and R. K. Gupta, Nucl. Phys. A **870**, 42 (2011).

[84] P. Quentin and H. Flocard, Ann. Rev. Nucl. Part. Sci. **28**, 523 (1978).

[85] J. Dechargé and D. Gogny, Phys. Rev. **21**, 1568 (1980).

[86] P.-G. Reinhard, Rep. Prog. Phys. **52**, 439 (1989).

[87] J. Bartel, P. Quentin, M. Brack, C. Guet and H. B. Hakansson, Nucl. Phys. A **386**, 79 (1982).

[88] F. Tondeur, M. Brack,M. Farine, and J. M. Pearson, Nucl. Phys. A **420**, 297 (1984).

[89] E. Chabanat, P. Bonche, P. Haensel, J. Meyer, and R. Schaeffer, Nucl. Phys. A **635**, 231 (1998).

[90] S. Krewald, V. Klemt, J. Speth and A. Faessler, Nucl. Phys. A **281**, 166 (1977).

[91] T. Duguet and P. Bonche, Phys. Rev. C **67**, 054308 (2003); B. Cochet, K. Bennaceur, P. Bonche, T. Duguet, and J. Meyer, Nucl. Phys. A **731**, 34 (2004).

[92] B. K. Agrawal, S. Shlomo, and V. Kim Au, Phys. Rev. C **72**, 014310 (2005); B. K. Agrawal, S. K. Dhiman, and R. Kumar, Phys. Rev. C **73**, 034319 (2006).

[93] H. S. Kohler, Nucl. Phys. A **258**, 301 (1976).

[94] H. Krivine, J. Treiner and O. Bohigas, Nucl. Phys. A **336**, 155 (1980); J. Treiner and H. Krivine, J. Phys. G **2**, 285 (1976).

[95] P. G. Reinhard and H. Flocard, Nucl. Phys. A **584**, 467 (1995).

[96] K. Hagino *et al.*, Phys. Rev. C **55**, 276 (1997); K. Hagino, A. Vitturi, C. H. Dasso and S. M. Lenzi, Phys. Rev. C **61**, 037602 (2002).

[97] R. K. Gupta, D. Singh, and W. Greiner, Phys. Rev. C **75**, 024603 (2007).

[98] D. Jain, R. Kumar and M. K. Sharma, Phys. Rev. C **85**, 024615 (2012).

[99] J. Blocki, J. Randrup, W. J. Swiatecki, and C. F. Tsang, Ann. Phys. (NY) **105**, 427 (1977).

[100] R. Bass, Nucl. Phys. A **231**, 45 (1974).

[101] R. Bass, Nuclear Reactions with Heavy Ions, Springer-Verleg, Berlin (1980).

[102] Deryagin, Kolloid Z. **69**, 155 (1934).

[103] W. Reisdorf, J. Phys. G: Nucl. Part. Phys. **20**, 1297 (1994).

[104] W. D. Myers and W. J. Swiatecki, Phys. Rev. C **62**, 044610 (2000).

Chapter 2

Methodology

2.1 Introduction

The main motive of this work is to address the excitation energy, angular momentum, deformation and orientation effects associated with the formation and disintegration of compound nucleus in low energy heavy ion induced reactions. For a proper understanding of dynamics involved, it is necessary to have an appropriate choice of nuclear interaction potential. The nucleon-nucleon potentials fall into two classes describe as phenomenological and microscopic methods. In this chapter, both kind of nuclear potentials are discussed, one obtained from Blocki *et al.* potential based on phenomenological picture and other using the well known Skyrme Energy Density Formalism (SEDF) a microscopic method. In literature within energy density formalism two different functional forms of Hamiltonian density are available (i) one is given by Bruckner *et al.* [1]- [4] and (ii) uses the density dependent Skyrme interactions [5] as applied by Vautherin and Brink [6]. In the present thesis, later approach is used for the estimation of microscopic potential due to its simple mathematical structure discussed in section 2.2.

To account the fusion process, Wong formula [7]- [9] is applied in which tunnelling probability of composite system is estimated according to Hill-Wheeler approximation. The relevant information of Wong formula and its extended ℓ-summed

form is presented in section 2.3. To govern the excited state decay of hot ($T\neq0$) and rotating ($\ell\neq0$) compound nucleus (CN), the dynamical Cluster-decay Model (DCM) [10]- [16], an extension of preformed cluster model (PCM) [17]- [22] (T=0 and ℓ=0), is employed. DCM originates from the well known Quantum Mechanical Fragmentation Theory (QMFT) [23]- [29], derived to study the dynamics involved in heavy ion reaction. Compound nucleus is a complex body system which even at lower excitation energies, involve large number of degree of freedom and consequently opens the existence of number of decay channels. In such physical conditions, the dynamical cluster decay approach emerges as an option to address the competing decay paths of nuclear systems. Within DCM, the escape tunnelling probability is calculated using the low-energy limit of the WKB formula, where the entry point of the penetration path is defined through a neck-length parameter, which is optimized to address the fusion-evaporation and fusion-fission excitation functions adequately. The probability of formation of nascent fragments known as 'preformation probability' (or spectroscopic factor) is calculated by solving the time independent Schrodinger equation in mass asymmetry η-co-ordinate, which also carry the structural information of the decaying compound nucleus. It should be mentioned here that the prescription used in such a calculation is similar in spirit to the Hauser-Feshbach theory, with the decay probability replacing the branching ratio, $\mathrm{T}_f(\ell)/\Sigma j\mathrm{T}_j(\ell)$, where $T_j(\ell)$ is the transmission coefficient of final channel j, and $\mathrm{T}_f(\ell)$ is the same for the detected fragment f. An overview of DCM approach is discussed in section 2.4. In the following section an attempt is made to give a brief account of microscopic nuclear potential calculated in the framework of SEDF.

2.2 Skyrme Energy Density Formalism (SEDF)

In this section, the theoretical structure of the microscopic Skyrme Energy Density Formalism (SEDF) along with semiclassical extended Thomas-Fermi (ETF) ap-

proach shall be discussed to parameterize the nucleus-nucleus interaction potential and subsequently to study the fusion barrier and fusion-fission excitation functions. The nuclear interaction potential V_N(R) between colliding nuclei can be defined as

$$V_N(R) = E_{tot}(R) - E_1 - E_2 \tag{2.1}$$

where E_{tot}(R) is the total energy expectation value of the reacting parters at distance R (center to center), whereas the individual energies of non-interacting projectile and target nuclei is represented by E_1 and E_2. The energy expectation values E_{tot}(R), E_1 and E_2 are further obtained by volume integration of Hamiltonian density H(r) as,

$$E_{tot}(R) = \int H[\rho_p(\vec{r}), \rho_n(\vec{r})]d\vec{r}, \tag{2.2}$$

$$E_i(R) = \int H[\rho_{ip}(\vec{r}), \rho_{in}(\vec{r})]d\vec{r}, (i = 1, 2) \tag{2.3}$$

Here ρ_{ip}(r), ρ_{in}(r) are proton and neutron densities of non-interacting nuclei and ρ_p(r), ρ_n(r) densities of interacting nuclei.

H(r) in above equation stands for energy density functional given as in [6, 30], including the kinetic energy contribution τ(r) and nuclear interaction parts H_{sky}(r),

$$H(\rho, \tau, \vec{J}) = \frac{\hbar^2}{2m}\tau + H_{sky}(r) \tag{2.4}$$

The kinetic energy density τ is then calculated by extended Thomas fermi approximation of Bartel *et al.* [31] reads as

$$\tau_q(\vec{r}) = \frac{3}{5}(3\pi^2)^{2/3}\rho_q^{5/3} + \frac{1}{36}\frac{(\vec{\nabla}\rho_q)^2}{\rho_q} + \frac{1}{3}\Delta\rho_q + \frac{1}{6}\frac{\vec{\nabla}\rho_q \cdot \vec{\nabla}f_q + \rho_q\Delta f_q}{f_q} - \frac{1}{12}\rho_q\left(\frac{\vec{\nabla}f_q}{f_q}\right)^2$$

$$+\frac{1}{2}\rho_q\left(\frac{2m}{\hbar^2}\right)^2\left(\frac{W_0}{2}\frac{\vec{\nabla}(\rho+\rho_q)}{f_q}\right)^2, \tag{2.5}$$

with the effective mass form factor (f_q),

$$\begin{aligned} f_q(\vec{r}) &= 1+\frac{2m}{\hbar^2}\frac{1}{4}\left\{t_1(1+\frac{x_1}{2})+t_2(1+\frac{x_2}{2})\right\}\rho(\vec{r}) \\ &\quad -\frac{2m}{\hbar^2}\frac{1}{4}\left\{t_1(x_1+\frac{1}{2})-t_2(x_2+\frac{1}{2})\right\}\rho_q(\vec{r}). \end{aligned} \tag{2.6}$$

Now the Skyrme nuclear interaction is given as

$$\begin{aligned} H_{sky}(r) &= \frac{1}{2}t_0\left[(1+\frac{1}{2}x_0)\rho^2-(x_0+\frac{1}{2})(\rho_n^2+\rho_p^2)\right] \\ &\quad +\frac{1}{2}\sum_{i=1}^{3}t_{3i}\rho^{\alpha_i}\left[(1+\frac{1}{2}x_{3i})\rho^2-(x_{3i}+\frac{1}{2})(\rho_n^2+\rho_p^2)\right] \\ &\quad +\frac{1}{4}\left[t_1(1+\frac{1}{2}x_1)+t_2(1+\frac{1}{2}x_2)\right]\rho\tau \\ &\quad -\frac{1}{4}\left[t_1(x_1+\frac{1}{2})-t_2(x_2+\frac{1}{2})\right](\rho_n\tau_n+\rho_p\tau_p) \\ &\quad +\frac{1}{16}\left[3t_1(1+\frac{1}{2}x_1)-t_2(1+\frac{1}{2}x_2)\right](\vec{\nabla}\rho)^2 \\ &\quad -\frac{1}{16}\left[3t_1(x_1+\frac{1}{2})+t_2(x_2+\frac{1}{2})\right]\times\left[(\vec{\nabla}\rho_n)^2+(\vec{\nabla}\rho_p)^2\right] \\ &\quad +\frac{1}{2}W_0\left[\rho\vec{\nabla}\cdot\vec{J}\right]+\frac{1}{2}W_0'\left[\rho_n\vec{\nabla}\cdot\vec{J}_n+\rho_p\vec{\nabla}\cdot\vec{J}_p\right] \\ &\quad -\left[\frac{1}{16}(t_1x_1+t_2x_2)\vec{J}^2-\frac{1}{16}(t_1-t_2)(\vec{J}_p^2+\vec{J}_n^2)\right] \end{aligned} \tag{2.7}$$

Here, the nuclear and spin-orbit densities are represented by ρ and $\vec{J}$. t_j, x_j (j=0,1,2), t_{3i}, x_{3i}, α_i, (i=1,2,3), A refers to the Skyrme force parameters and W_0, W_0' denotes the strength of spin-orbit interaction. The various terms in Eq 2.4 and

Eq 2.7 have a particular meaning as ($\hbar^2$/2m) determine the density dependence of effective mass, $\rho\tau$ takes care of relativistic force, $(\vec{\nabla}\rho)^2$ is responsible for surface effects and $\vec{\nabla}\cdot\vec{J}$ term is used to understand the structure of spin-density potential. Some of the authors have modified standard Skyrme functional by revisiting some parts of original Skyrme force(s) by adding an extra term in spin-orbit part. A subsequent extension comes from Reinhard and Flocard [30] which leads to SkI2, SkI3 and SkI4 Skyrme forces. In SkI2 force W_0=W$'_0$, for SkI3 W$'_0$=0 and for SkI4 $W_0\neq$W$'_0$. In original Skyrme force W_0=W$'_0$ only as in SIII force [32]. The last term in the Hamiltonian represents the tensor coupling with spin and gradient. Author of [33] has introduced new Skyrme parameter set known as SKRA force with contribution from tensor coupling term but contain single spin-orbit parameter i.e. W_0=W$'_0$ only. Recently, some new Skyrme forces named as 'GSkI and GSkII' are given by Agarwal and collaborators [34] with additional six parameters in the third term of the Hamiltonian. These forces are found to account better for nuclear interactions and adequately describe finite nuclei at low and intermediate energies. It is relevant to mention here that the use of different Skyrme forces enables us to have a variety of barrier characteristics and hence the addressal of fusion cross-section gets significantly influenced due to the barrier modification component. This barrier modification helps us to address the fusion enhancement/ fusion hindrance somewhat similar to that of coupled channel approach (the results are discussed in chapter 6).

In Eq. (2.7), spin density $\vec{J}$ is given by

$$\vec{J}_q(\vec{r}) = -\frac{2m}{\hbar^2}\frac{1}{2}W_0\frac{1}{f_q}\rho_q\vec{\nabla}(\rho+\rho_q), \tag{2.8}$$

Note that each of τ_q, f_q and $\vec{J}_q$ are functions of ρ_q and/ or ρ alone.

Densities of composite system $\rho = \rho_1 + \rho_2$ with $\rho_i = \rho_{in} + \rho_{ip}$ (i=1,2), and the $\tau(\rho)$ and $\vec{J}(\rho)$ are added under frozen density approximation, as follows:

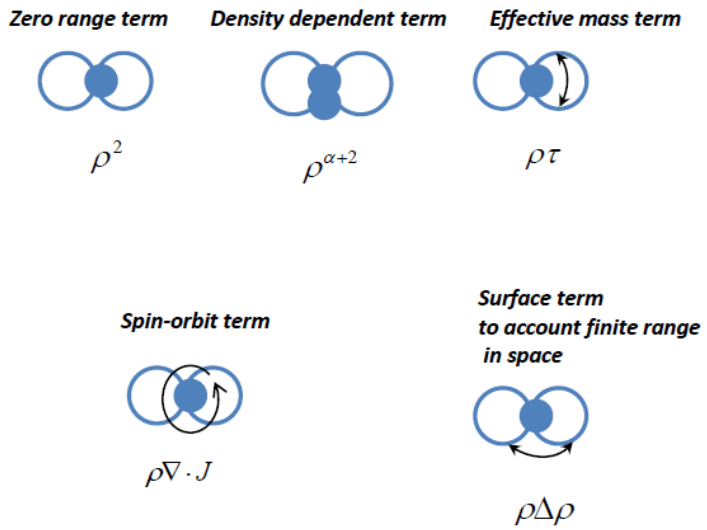

Figure 2.1: A Schematic view of nucleon-nucleon interaction within Skyrme approach [35].

$$\begin{aligned} \tau(\rho) &= [\tau_{1n}(\rho_{1n}) + \tau_{1p}(\rho_{1p})] + [\tau_{2n}(\rho_{2n}) + \tau_{2p}(\rho_{2p})], \\ \vec{J}(\rho) &= [\vec{J}_{1n}(\rho_{1n}) + \vec{J}_{1p}(\rho_{1p})] + [\vec{J}_{2n}(\rho_{2n}) + \vec{J}_{2p}(\rho_{2p})], \end{aligned} \tag{2.9}$$

The nuclear interaction potential in Eq. (2.1) is calculated by using slab approximation method [36] given as

$$\begin{aligned} V_N(R) &= 2\pi\bar{R}\int_{s_0}^{\infty} e(s)ds \\ &= 2\pi\bar{R}\int \left\{H(\rho,\tau,\vec{J}) - [H_1(\rho_1,\tau_1,\vec{J}_1) + H_2(\rho_2,\tau_2,\vec{J}_2)]\right\} dZ \\ &= 2\pi\bar{R}\int \left\{(H(\rho) - [H_1(\rho_1) + H_2(\rho_2)]) + \left(H(\vec{J}) - [H_1(\vec{J}_1) + H_2(\vec{J}_2)]\right)\right\} dZ \\ &= V_P(R) + V_J(R). \end{aligned} \tag{2.10}$$

Here, $V_J(R)$ and $V_P(R)$ are spin unsaturated (density dependent) and spin saturated (density independent) parts of nuclear interaction potential. The mean curvature radius, $\bar{R} = R_1R_2/(R_1+R_2)$, defines the geometry of the system. It is to be noted here that, the surface integral of $e(s)$ is a universal function, independent of the

geometry of the colliding nuclei.

Temperature dependent nuclear density (ρ_i)

The nuclear density used in Eq. (2.7) can be evaluated from different models such as Thomas Fermi Density (TFD), Two Parameter Fermi Density (FD), Shell Model Density (SMD) and Uniform Gaussian Density (UGD) etc. In this work, nuclear density ρ_i is obtained from the two-parameter Fermi density as the same is more realistic for heavy ion collisions, which is further made temperature dependent by Bartel *et al.* [37] as

$$\rho_i(z_i) = \rho_{0i}(T)\left[1+\exp\left(\frac{z_i - R_i(T)}{a_i(T)}\right)\right]^{-1} \quad -\infty \leq z \leq \infty \tag{2.11}$$

with $z_2 = R - z_1 = [R_1(\alpha_1) + R_2(\alpha_2) + s] - z_1$, and central density

$$\rho_{0i}(T) = \frac{3A_i}{4\pi R_i^3(T)}\left[1+\frac{\pi^2 a_i^2(T)}{R_i^2(T)}\right]^{-1}. \tag{2.12}$$

Since $\rho_i = \rho_{n_i} + \rho_{p_i}$, therefore we define neutron and proton densities as $\rho_{n_i} = (N_i/A_i)\rho_i$ and $\rho_{p_i} = (Z_i/A_i)\rho_i$.

The radius vector $\mathrm{R}_i(T)$ in Eq. 2.11 is defined as

$$R_i(T) = R_{0i}(T)[1+\sum_{\lambda}\beta_{\lambda i}Y_{\lambda}^{(0)}(\alpha_i)], \tag{2.13}$$

with half density radii R_{0i} is given by

$$\begin{aligned} R_{0i}(T=0) &= 0.9543 + 0.0994A_i - 9.8851\times10^{-4}A_i^2 \\ &\quad +4.8399\times10^{-6}A_i^3 - 8.4366\times10^{-9}A_i^4 \end{aligned} \tag{2.14}$$

The surface thickness parameters a_i at T=0 for the mass region A=4-238 is

obtained from [38, 39]

$$\begin{aligned} a_i(T=0) &= 0.3719 + 0.0086A_i - 1.1898\times10^{-4}A_i^2 \\ &\quad +6.1678\times10^{-7}A_i^3 - 1.0721\times10^{-9}A_i^4. \end{aligned} \tag{2.15}$$

The temperature-dependence T in above equations is then included via [40],

$$\begin{aligned} R_{0i}(T) &= R_{0i}(T=0)[1+0.0005T^2], \\ a_i(T) &= a_i(T=0)[1+0.01T^2]. \end{aligned} \tag{2.16}$$

The nuclear potential described in this section shall be used to calculate the fusion cross-section within Wong approximation discussed in section 2.3 and the decay cross-sections in the framework of the dynamical cluster decay model as describe in section 2.4. The detail of calculations and results are discussed in subsequent chapters.

2.3 Fusion cross-section using Wong formula

Within partial wave analysis, Wong [7] has derived an expression of fusion cross-section as

$$\sigma(E_{c.m.},\theta_i) = \frac{\pi\hbar^2}{2\mu E_{c.m.}}\sum_{\ell}(2\ell+1)P_\ell(E_{c.m.},\theta_i), \tag{2.17}$$

P_ℓ is the tunnelling probability determined for each ℓ that describe the penetration of barrier V_T^ℓ,

$$V_T^\ell(R,E_{c.m.},\theta_i) = V_N(A_i,R,T,\beta_{\lambda i},\theta_i) + V_C(Z_i,R,T,\beta_{\lambda i},\theta_i) + V_\ell(A_i,R,T,\beta_{\lambda i},\theta_i), \tag{2.18}$$

Here V_C, V_N and V_ℓ correspond to the temperature-dependent Coulomb, nuclear and centrifugal potentials, discussed later in sections 2.5.1, 2.5.2 and 2.5.3

respectively and A_i and Z_i are the mass and charge number of interacting nuclei. β_{λ_i}, λ=2,3,4 are the static quadrupole, octupole and hexadecapole deformations of colliding partners.

Based upon parabolic approximation of the effective interaction potential between colliding nuclei, Hill and Wheeler [41] proposed following expression for tunnelling probability P_ℓ,

$$P_\ell = \left[1 + \exp\left(\frac{2\pi(V_B^\ell(E_{c.m.},\theta_i) - E_{c.m.})}{\hbar\omega_\ell(E_{c.m.},\theta_i)}\right)\right]^{-1}, \tag{2.19}$$

with curvature $\hbar\omega_\ell(E_{c.m.},\theta_i)$, calculated at the barrier position $R = R_B^\ell$ corresponding to the maximum barrier height $V_B^\ell(E_{c.m.},\theta_i)$, given as

$$\hbar\omega_\ell(E_{c.m.},\theta_i) = \hbar\left[|d^2V^\ell(R)/dR^2|_{R=R_B^\ell}/\mu\right]^{1/2}, \tag{2.20}$$

and, the R_B^ℓ calculated from the condition

$$|dV_T^\ell(R)/dR|_{R=R_B^\ell} = 0 \tag{2.21}$$

The above expression of penetrability was further simplified by Wong via imposing some assumptions on barrier position, curvature and height

i) $\hbar\omega_\ell \approx \hbar\omega_0$, and (ii) $V_B^\ell \approx V_B^0 + \frac{\hbar^2\ell(\ell+1)}{2\mu {R_B^0}^2}$,

In other words, both V_B^ℓ and $\hbar\omega_\ell$ are independent of ℓ and V_B^0 is the sum of nuclear proximity potential V_P and Coulomb potential V_C at $R = R_B^0$.

$$V_B^0 = V_P(A_i, R = R_B^0, \beta_{\lambda i}, E_{c.m.}, \theta_i) + V_C(Z_i, R = R_B^0, \beta_{\lambda i}, E_{c.m.}, \theta_i) \tag{2.22}$$

Since infinite number of partial waves contribute to the fusion process, hence,

the summation in Eq. (2.17) can be replaced by an integral over ℓ. By using above assumptions, the fusion cross-section determined for each orientation is obtained as,

$$\sigma(E_{c.m.},\theta_i) = \frac{{R_B^0}^2 \hbar\omega_0}{2E_{c.m.}} \ln\left[1+\exp\left(\frac{2\pi}{\hbar\omega_0}(E_{c.m.}-V_B^0)\right)\right], \tag{2.23}$$

This expression is known as Wong formula.

On integration over orientation angle θ_i (i=1,2) the fusion cross-section at the given center of mass energy $E_{c.m.}$ becomes,

$$\sigma(E_{c.m.}) = \int_{\theta_i=0}^{\pi/2} \sigma(E_{c.m.},\theta_i) sin\theta_i d\theta_i. \tag{2.24}$$

Although Wong formula gives satisfactory description of fusion cross-section near the Coulomb barrier, but overestimates the same at the higher incident energies, due to the consideration of all angular momentum values (though the barrier characteristics are calculated for s-wave only). In view of this, Gupta *et al.* [9] suggested the extension of Wong formula to include ℓ-summation explicitly in Eq. (2.17) and calculated the barrier characteristics such as V_B^ℓ, R_B^ℓ and $\hbar\omega_\ell$ at various ℓ-values. This modified version is known as ℓ-summed extended Wong formula or ℓ-summed Wong formula. In this extended form, the ℓ-summation is done from ℓ=0 to ℓ_{max} rather than upto ∞. This method is reasonably good for addressing the fusion cross-section at higher incident energies, however demands modification of barrier at sub-barrier region. Which is further done by employing different proximity potentials or by using different Skyrme forces in Semi-classical extended Thomas-Fermi (SETF) approach, giving different barrier characteristics.

After describing the formulation for fusion cross-section, the subsequent decay channels of excited compound nucleus can be addressed via dynamical cluster decay model (DCM) discussed below in Section 2.4. A flow chart presenting both nuclear

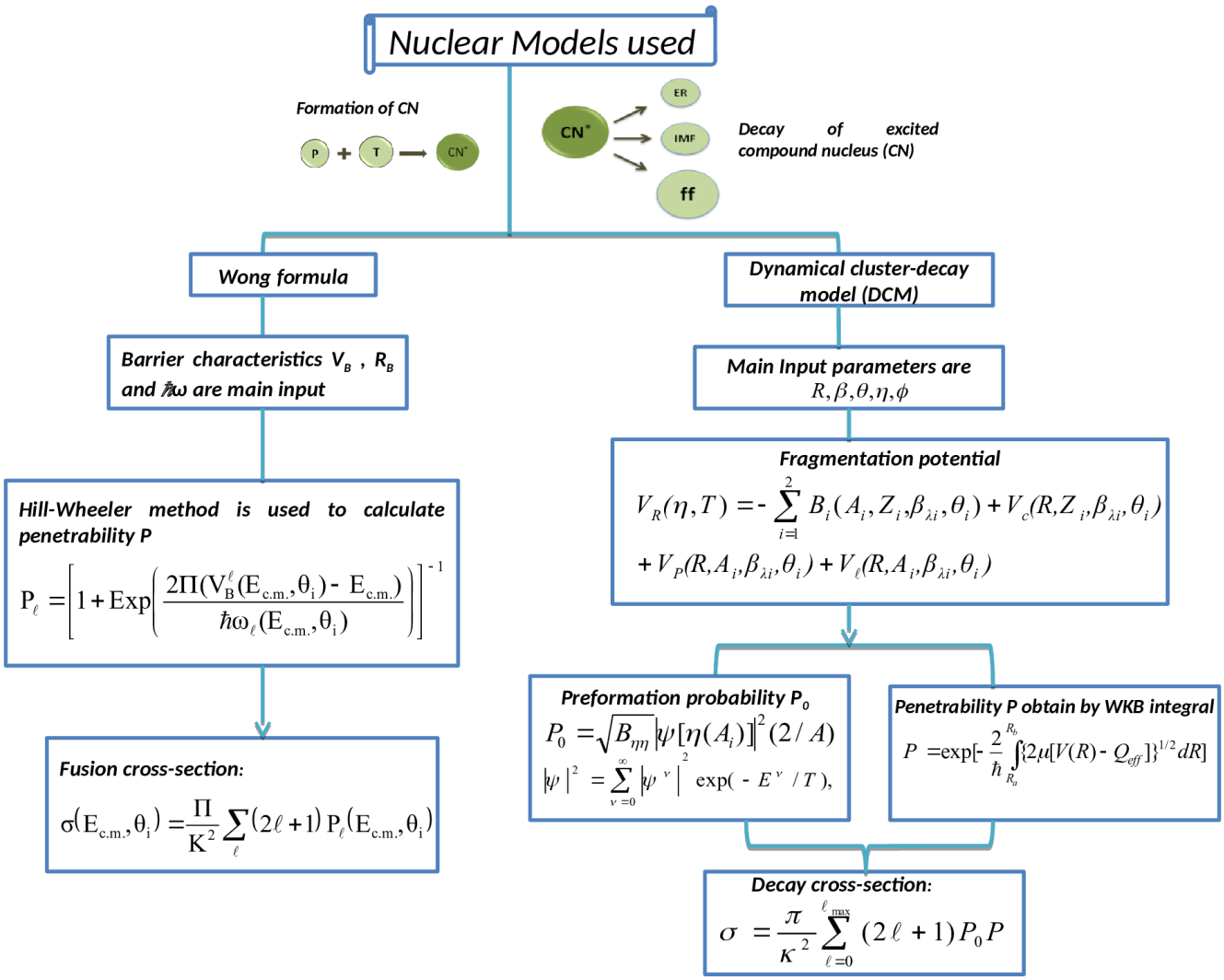

Figure 2.2: Flow chart of nuclear models used to study formation and decay of compound nucleus.

models is shown in Fig. 2.2

2.4 Decay of excited compound nucleus using the Dynamical Cluster-decay Model (DCM)

The dynamical cluster decay model (DCM) is based on a non-statistical description within the framework of quantum mechanical fragmentation theory (QMFT), where all decay modes such as light particle emission (LPs), intermediate mass fragments (IMFs) and fusion-fission (ff) etc are estimated simultaneously in one set of

calculation and also bring out the nuclear structure information in terms of preformation probability of decaying fragments. The static properties of the nucleus are describe by the potential energy, whereas for exploring nuclear dynamics, in addition to potential energy, the mass parameters are used as paramount tool to address the kinetic energy contribution. In this formalism, the decay of excited compound nucleus is investigated by incorporating the temperature and angular momentum effects, along with the influence of deformation and orientation degree of freedom. The methodology used can be described in terms of five co-ordinates (i) Neck parameter ε, defined by the ratio $\varepsilon = E_0/E'$, where E_0 and E' exhibit the actual and fixed height of the barrier, of the two center oscillator. $\epsilon = 1$ represents that, the neck is fully squeezed in, whereas for broad neck formation $\epsilon = 0$ (corresponding to the asymptotic region). (ii) relative separation coordinate R between the two fragments or, two nuclei. (iii) The collective surface co-ordinate or simply deformation of target and projectile $\beta_{\lambda i}$ (λ=2, 3, 4... and i=1, 2) and the orientation degrees of freedom $\theta_i (i = 1, 2)$ of the two deformed colliding nuclei. (iv) The azimuthal angle ϕ formed between the principal planes of the two colliding nuclei. (v) the mass (and charge) co-ordinate [23, 28] defined as, $\eta_A = (A_1 - A_2)/(A_1 + A_2)$ (and $\eta_Z = (Z_1 - Z_2)/(Z_1 + Z_2)$. Here A_1, A_2 and Z_1, Z_2 respectively refer to mass and charge number of two fragments.

In terms of above coordinates, the collective Hamiltonian is written as H=K(η, R, β, θ, ϕ)+V(η, R, β, θ, ϕ), where K attributes to Kinetic energy and V to the potential energy. For fixed orientation, the mass η is fixed by minimizing the potential V in the η coordinate, which fixes the deformation also. Moreover, the colliding nuclei being in same plane correspond to ϕ=0, where for non-coplanar interactions one should take $\phi \neq 0$.

Thus, for fixed β, θ and ϕ, both η and R contribute to study the decay cross-

section in terms of partial wave analysis defined as [42, 43]

$$\sigma = \sum_{\ell=0}^{\ell_{max}} \sigma_\ell = \frac{\pi}{k^2} \sum_{\ell=0}^{\ell_{max}} (2\ell+1) P_0 P; \qquad k = \sqrt{\frac{2\mu E_{c.m.}}{\hbar^2}} \tag{2.25}$$

where, ℓ_{max} is the maximum value of angular momentum, calculated at a point where light particle cross-sections become negligibly small i.e., $\sigma_{ER}(\ell) \rightarrow 0$. $\mu = mA_1A_2/(A_1 + A_2)$ is the reduced mass with nucleon mass m. P_0 is the probability of formation of fragments at compound nucleus state calculated in η-motion and P is the barrier penetrability of decaying fragments related to R-motion. The brief description of P_0 and P is discussed in subsequent subsections.

In DCM, η and R co-ordinates are characterized by the nucleon division/exchange between outgoing fragments and by the devolution of kinetic energy of incident channel ($E_{c.m.}$) to total excitation energy (TXE) and or total kinetic energy (TKE) (internal excitation) of the outgoing channel. Therefore, the energy transfer process is expressed as following

$$E^*_{CN} = E_{c.m.} + Q_{in} = \mid Q_{out}(T) \mid + TKE(T) + TXE(T). \tag{2.26}$$

The semi-empirical statistical formula [44] is used to calculate the nuclear temperature T at compound nuclear stage, which is related to the energy of excited compound nucleus E^*_{CN}, as:

$$E^*_{CN} = \frac{1}{a} A T^2 - T = E_{c.m.} + Q_{in} \qquad (MeV). \tag{2.27}$$

where a is the level density parameter. Its value may vary from 8 to 11 depending on the mass of the CN. The Q-value of the incoming channel 'Q_{in}' is obtained by $Q_{in} = B_1 + B_2 - B_{CN}$ where B's shows the the binding energies.

The average total kinetic energy <TKE> liberated in the decay process is calcu-

lated by, <TKE>= $\sum_{\ell=0}^{\ell_{max}} \frac{\sigma_\ell(A_2)}{\sigma(A_2)} TKE(\ell, A_2)$. This equation implies that, the TKE calculated at ℓ is averaged over its corresponding production cross-section σ_ℓ with respect to total cross-section $\sigma(A_2) = \sum_{\ell=0}^{\ell_{max}} \sigma_\ell(A_2)$.

2.4.1 Solution of preformation probability P_0

For calculating the quantum mechanical preformation probability of finding the mass fragment A_1 and A_2 corresponding to charges Z_1 and Z_2 respectively at a fixed point, we solve the time independent Schrödinger wave equation in mass asymmetry co-ordinate (η=$\frac{A_1-A_2}{A_1+A_2}$) at R=R_a (defined later)

$$\left[-\frac{\hbar^2}{2\sqrt{B_{\eta\eta}}}\frac{\partial}{\partial\eta}\frac{1}{\sqrt{B_{\eta\eta}}}\frac{\partial}{\partial\eta} + V(\eta)\right]\psi^\nu(\eta) = E^\nu_\eta \psi^\nu(\eta), \tag{2.28}$$

Here $\nu = 0, 1, 2...$, referring to ground state and excited state solutions. On solving Eq. (2.28), $\mid \psi^\nu(\eta) \mid^2$ provides the probability P_0 of finding the mass distribution as, $P_0 \propto \mid \psi^\nu(\eta) \mid^2$ which for Boltzmann like function reads as,

$$\mid \psi(\eta) \mid^2 = \sum_{\nu=0}^{\infty} \mid \psi^\nu(\eta) \mid^2 exp(\frac{-E^\nu}{T}) \tag{2.29}$$

It is evident from above expressions that, the temperature effects are duly incorporated in the preformation factor P_0^ℓ which is calculated using the collective clusterization method. In Eq. (2.28), $B_{\eta\eta}$ is the mass parameter used to define the kinetic energy term. In the present work, simple classical model given by Kröger and Scheid for mass transfer in heavy ion collision [45] is used to account for hydrodynamical mass parameter $B_{\eta\eta}$, which read as

$$B_{\eta\eta} = \frac{AmR^2}{4}\left[\frac{v_t(1+\gamma)}{v_c(1+\delta^2)} - 1\right] \tag{2.30}$$

with

$$\gamma = \frac{R_c}{2R}\left[\frac{1}{1+\cos\vartheta_1}\left(1-\frac{R_c}{R_1}\right)+\frac{1}{1+\cos\vartheta_2}\left(1-\frac{R_c}{R_2}\right)\right] \tag{2.31}$$

$$\delta = \frac{1}{2R}\left[(1-\cos\vartheta_1)(R_1-R_c)+(1-\cos\vartheta_2)(R_2-R_c)\right] \tag{2.32}$$

$$v_c = \pi R_c^2 R \tag{2.33}$$

In Eq. (2.30), v_t ($=v_1+v_2$) is the total conserved volume. For two touching sphere $\vartheta_1 = \vartheta_2 = 0$, $\delta = 0$. The radius of a cylinder $R_c(\neq 0)$ of length R is assumed for the mass transfer between the two spherical fragments, having a homogeneous flow in it (see Fig.1 of [45]).

2.4.2 Analytical method to calculate barrier penetrability 'P'

The barrier penetrability or transmission probability P is solved analytically [22] using the WKB integral [46], and reads as

$$P = \exp\left[-\frac{2}{\hbar}\int_{R_a}^{R_b}\{2\mu[V(R)-Q_{eff}]\}^{1/2}dR\right]. \tag{2.34}$$

Q_{eff} refers to effective Q-value of decay process and V(R) is the scattering potential given as a sum of Coulomb (V_C) nuclear proximity (V_N) and centrifugal (V_ℓ) potentials (discussed later in sections 2.5.1, 2.5.2 and 2.5.3 respectively). The limits over integral means that the fragments start penetration of barrier at R = R_a and terminates at R = R_b. Since in DCM single penetration path is adopted as a result of this the potential at positions R_a and R_b remain same or equal and reads as $V(R_a,T) = V(R_b,T) = TKE(T) = Q_{eff}$, where $V(R_a)$ and $V(R_b)$ represent the scattering potentials experienced by the fragment during entry and exit of the

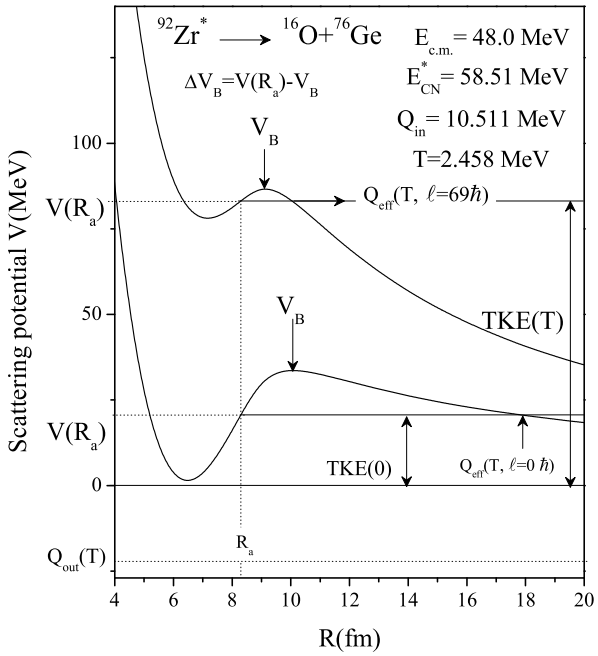

Figure 2.3: The scattering potential for the decay of ^{92}Zr$^{*}\rightarrow^{16}$O+^{76}Ge using Blocki *et al.* potential. The barrier penetration points and barrier lowering parameter ΔV_B are also shown at extreme ℓ-values.

barrier as represented in Fig. 2.2. The entry point is calculated as

$$\begin{aligned} R_a &= R_1(\alpha_1, T) + R_2(\alpha_2, T) + \Delta R(\eta, T) \\ &= R_t(\alpha_i, T) + \Delta R(\eta, T), \end{aligned} \tag{2.35}$$

The radius vector $\mathrm{R}_i(\alpha_i, T)$, through which deformation and orientation effects are added, is defined as

$$R_i(\alpha_i, T) = R_{0i}(T)[1 + \sum_{\lambda} \beta_{\lambda i} Y_{\lambda}^{(0)}(\alpha_i)], \tag{2.36}$$

and

$$R_{0i}(T) = R_{0i}(1 + 0.0007T^2). \tag{2.37}$$

Here β is the deformation parameter with λ=2,3,4... corresponds to quadrupole, octapole and hexadecapole deformations. α_i is an angle formed by the radius vector R_i with the symmetry axis (see Fig. 2.4), measured clockwise. ΔR refers to the neck-length parameter which assimilated the neck formation effects as taken in Asymmetric Two Center Shell Model (ATCSM) [23]. In DCM, for the uniquely fixed co-ordinates as explained earlier, the decay cross-sections are attained using the only parameter of model i.e. neck-length ΔR. In general, for a variety of nuclei studied using DCM, it has been observed that ΔR in general increases with increase in incident energy [16, 47].

The deformations added here are the temperature independent or static deformations $\beta_{\lambda i}(0)$. Since at higher excitation energies, the static deformation start approaching zero [48, 49], therefore the deformation parameter needs to be temperature dependent [49–51], and corresponding dynamics deformations are evaluated as

$$\beta_{\lambda i}(T) = \exp(-\frac{T}{T_0})\beta_{\lambda i}(0), i = 1, 2 \tag{2.38}$$

where T_0= 1.5 MeV refers to the temperature of the nucleus at which shell effects start to disappear [50].

It may be noted that with the incorporation of deformations (β_1,β_2....β_n), a generalized force acts on a nucleus which may be studied through tensor of inertia or the effective mass parameter B_{ij}. In reference to the work of D. N. Poenaru *et al.* [52], it may be said that, for incompressible irrotational approach, the effective mass is nearly similar to reduced mass μ, as used in Eq. (2.34).

2.5 Fragmentation potential

To analyze the dynamics involved in various compound systems, the potential energy surfaces (PESs) are studied in terms of fragmentation potential which is the major

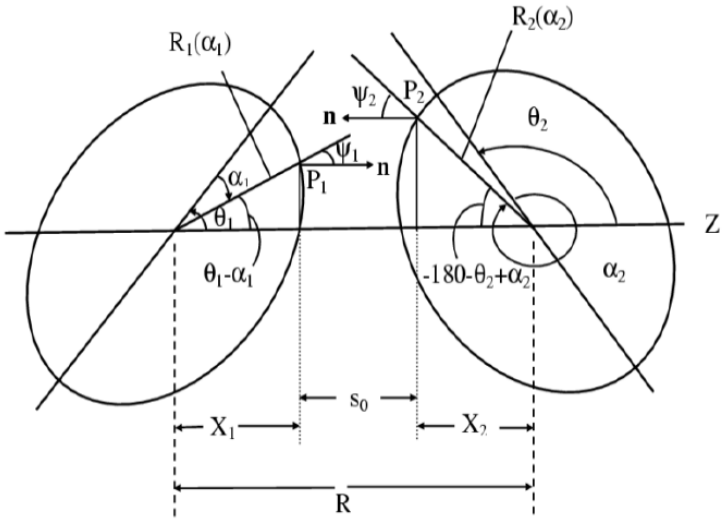

Figure 2.4: Schematic picture of two prolate deformed nuclei with their orientation angles and α's lying in the same plane.

ingredient of stationary Schrödinger equation. It helps to understand the forces acting on the fragments originating from different potential components and thus help in estimating the relative stability of decaying fragments. Therefore the temperature, deformation and orientation dependent fragmentation potential or collective potential energy is given as,

$$\begin{aligned} V(\eta, R, \ell, T) &= \sum_{i=1}^{2} V_{LDM}(Z_i, A_i, T, \beta_{\lambda i}) + \sum_{i=1}^{2} \delta U_i \exp(-T^2/T_0^2) \\ &\quad + V_C(Z_i, R, T, \beta_{\lambda i}, \theta_i, \phi) + V_N(A_i, R, T, \beta_{\lambda i}, \theta_i, \phi) \\ &\quad + V_\ell(A_i, R, T, \beta_{\lambda i}, \theta_i, \phi) \end{aligned} \tag{2.39}$$

In above equation, first two terms corresponds to the binding energies (B.E) of the outgoing fragments calculated within Strutinsky renormalization procedure [53]. In the macro-microscopic method of Strutinsky, the B.E is the sum of temperature-dependent liquid drop model energy V_{LDM} (macroscopic part) given by Davidson *et al.* [54] based on Seeger's [55] semi-empirical mass formula and "empirical" shell corrections (microscopic part) δU of Myers and Swiatecki [56]. In this work, binding

energies are taken from the experimental work of Audi-Wapstra [57]. However, for those nuclei where experimental B.E is not available, the theoretical estimates of Möller *et al.* [58] tabulated for $Z \geq 8$ are opted. In order to have proper description of binding energies for complete mass range, the authors of [42] have modified the empirical method of Myers-Swiatecki (given for $Z \leq 16$) and estimated the shell corrections for light mass nuclei.

In recent years, the extension of microscopic corrections with inclusion of deformations has been effectively studied by R. A. Gherghescu *et al.* [59, 60] through deformed two-center shell model, which describes the evolution of single particle levels from parent potential to that of two fragment potential. Apparently, such inclusion of deformations in shell correction may result some modification in the potential depth. In the present work deformations are included through radius term as mention in Eq. (2.36).

2.5.1 The Coulomb potential (V_C)

Coulomb potential (V_C) arises due to the electro-static force of repulsion acting between the two charged ions (or nuclei). The Coulomb potential between spherically symmetric nuclei is simply describe as

$$V_c = \frac{Z_1 Z_2 e^2}{R} \tag{2.40}$$

If the interacting nuclei are deformed and oriented, then the above expression is accordingly modified. Several authors [7, 61–63] have given various expressions for the interaction between two hot, deformed and oriented nuclei given such as [61]:

$$\begin{aligned} V_c(Z_i, \beta_{\lambda i}, \theta_i, \alpha_i, T) &= \frac{Z_1 Z_2 e^2}{R(T)} + 3 Z_1 Z_2 e^2 \sum_{\lambda, i=1,2} \frac{1}{2\lambda+1} \frac{R_i^{\lambda}(\alpha_i, T)}{R(T)^{\lambda+1}} Y_{\lambda}^{(0)}(\theta_i) \\ &\quad \Big[\beta_{\lambda i} + \frac{4}{7} \beta_{\lambda i}^2 Y_{\lambda}^{(0)}(\theta_i)\Big], \end{aligned} \tag{2.41}$$

$Y_\lambda^{(0)}(\theta_i)$ represents the spherical harmonics function.

2.5.2 The nuclear Proximity Potential for deformed and oriented nuclei (V_N)

All the proximity potentials arise from proximity forces, based on generalized force theorem, according to which: when two nuclear surfaces interact within a distance of $< 2fm$, or when a nucleus is at the point of breaking into two fragments, then the two surfaces actually face each other. In both the cases, the surface energy term is insufficient to explain the attraction between two surfaces and hence some additional forces are required. Such additional attractive forces are named as proximity forces and related potential is called the proximity potential. The proximity force originally given by Deryagin [64], was reanalyzed and extended by Blocki *et al.* [65]. The original expression of proximity potential was applicable for spherical nuclei only, which was extended further by authors of [66] for two deformed and oriented nuclei as,

$$V_N(A_i, R, T, \beta_{\lambda i}, \theta_i) = 4\pi\bar{R}(T)\gamma b(T)\Phi(s_0(T)) \tag{2.42}$$

Here $\Phi(s_0)$ is the universal function, independent of the geometry of nuclear system, but depends on the minimum separation distance s_0,

$$\Phi(s_0) = \begin{cases} -\frac{1}{2}(s_0 - 2.54)^2 - 0.0852(s_0 - 2.54)^3; s_0 \leq 1.2511 \\ -3.437exp(-\frac{s_0}{0.75}); s_0 \geq 1.2511 \end{cases} \tag{2.43}$$

s_0 is defined in terms of nuclear surface diffuseness b, i.e. s_0/b. The temperature dependence in b [67] is added via the following expression

$$b(T) = 0.99(1 + 0.009T^2). \tag{2.44}$$

In the expression of V_N, γ is the specific nuclear surface tension defined as

$$\gamma = \gamma_0 \left[1 - k_s \left(\frac{N-Z}{A}\right)^2\right] MeVfm^{-2} \tag{2.45}$$

Here N and Z are the total number of neutrons and protons. In the present version, the value of coefficients γ_0, k_s is 0.9517 MeV/fm^2 and 1.7826 respectively. This potential is referred as Proximity 77 or Prox 77.

$\bar{R}(T)$ for spherical reacting partners reads as,

$$\overline{R} = \frac{R_1 R_2}{R_1 + R_2} \tag{2.46}$$

with radius vector, R_i (i=1,2)

$$R_i = \left[1.28A_i^{1/3} - 0.76 + 0.8A_i^{-1/3}\right]. \tag{2.47}$$

and for two deformed and oriented nuclei is expressed as

$$\begin{aligned} \frac{1}{\bar{R}^2} &= \frac{1}{R_{11}R_{12}} + \frac{1}{R_{21}R_{22}} + \left[\frac{1}{R_{11}R_{21}} + \frac{1}{R_{12}R_{22}}\right] sin^2\phi \\ &+ \left[\frac{1}{R_{11}R_{22}} + \frac{1}{R_{21}R_{12}}\right] cos^2\phi. \end{aligned} \tag{2.48}$$

R_{i1} and R_{i2} are the radii of curvature of the two nuclei (i=1,2) at the points of closest approach (defining s_0 in Fig. 2.4). ϕ is the azimuthal angle between the principal planes of curvature of two nuclei which for co-planar nuclei ϕ=0^0.

There are varieties of proximity potential such as Prox 77, Bass 80, Prox 88, Mod prox 88 etc., but we have used Prox77 in our analysis. Alternatively we discussed in section 2.2 for obtaining the contribution of nuclear interaction potential.

2.5.3 Centrifugal potential (V_ℓ)

Centrifugal potential originates due to the presence of pseudo or fictitious forces (inertial forces) pointing away from the axis of rotation. It appears to act on all objects when viewed in a rotating frame of reference. Such forces are governed by the angular momentum ℓ and play a pivotal role in describing the nuclear dynamics. The angular momentum in rotating nucleus can be effectuated either by alignment of single-particle angular momentum along the rotation axis or via collective rotation.

The relation between rotational energy, angular momentum and related moment of inertia is given by,

$$V_\ell(A_i, T, \beta_{\lambda i}, \theta_i, \alpha_i) = \frac{\ell(\ell+1)\hbar^2}{2I(T)} \tag{2.49}$$

where I represents the moment of inertia (MOI) of rotating system. Basically the moment of inertia depends on following factors such as: the axis upon which the system is rotating, mass(es) of nuclei and distance between the contributing nuclei and axis of rotation. For moment of inertia I, Cindro and Pocanic [68] considered the rotation of two touching spheres with masses A_1 and A_2 and radii R_1 and R_2 about their common center of mass. The resultant configuration with limit R=R_1+R_2 is known as "sticking" moment of inertia (I_S) such that,

$$I_S(T) = \mu R^2 + \frac{2}{5}A_1 m R_1^2(\alpha_1, T) + \frac{2}{5}A_2 m R_2^2(\alpha_2, T). \tag{2.50}$$

which for the separated nuclei (R>R_1+R_2), becomes simply equal to

$$I_{NS}(T) = \mu R^2 \tag{2.51}$$

called as "Non-sticking" limit [69].

In above equations, m is the nucleon mass and μ is the reduced mass of interacting nuclei. The use of reduced mass alone in Eq. (2.51) indicates the prompt

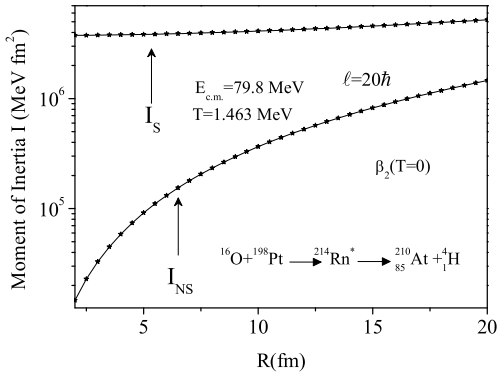

Figure 2.5: Variation of moment of inertia as a function of internuclear distance R.

emission of outgoing fragments. The variation of both the choices of moment of inertia as a function of inter nuclear distance R is shown in Fig. 2.5. Alternatively one can use other hypothesis such as rolling and sliding conditions.

Noting that, experimentally, the rotational momentum number ℓ is estimated using the MOI in non-sticking limit. However, in DCM, the preference of employing sticking limit of MOI is due to the use of Blocki *et al.* proximity potential with neck-length surface $\Delta R \leq 2$ fm, thereby increasing the limiting angular momentum as compared to I_{NS} limit, where lesser number of partial waves contribute towards the reaction cross-sections. The previous studies [70] suggest that, both I_S and I_{NS} limits are equally good to study evaporation residue process, although, in fission process I_S seems to perform better. These observations are for independent addressal of ER and fission paths. In order to generalize this aspect, we intended to carry out a comprehensive decay analysis of heavy ion-induced reactions exhibiting evaporation residue and fission paths over a common range of center of mass energy. In the present work, both sticking and non-sticking limits are used to analyze the decay path of excited ^{214,216}Rn* compound nuclei and the results are discussed in chapter 5.

2.5.4 Barrier lowering/Barrier modification effect

In heavy ion induced reactions, the formation of CN hinders with the increase in mass number of colliding partners, due to the presence of strong dissipative forces. In recent times, it has been observed that, some of the reactions show unexpected behavior at sub-barrier energies caused by the macroscopic properties of colliding nuclei. For such reactions, fusion excitation-functions decrease abruptly at sub-barrier energies. This phenomena is known as fusion-hindrance. Some of the theoretical models like conventional coupled-channels calculations (ccc) address this anomalous behavior by including coupling effects. Misicu and Esbensen [71] have proposed a new mechanism where this steep falloff is associated with the saturation properties of nuclear matter, which consequently modify the inner part of the nuclear potential. Beside this, Ichikawa *et al.* [72] explain fusion hindrance phenomena using a dynamical two-step model based on adiabatic picture. In last two approaches the repulsive core is exploited to amend the shape of potential pocket.

In the DCM the barrier lowering at sub-barrier energies originates automatically during the optimization of the neck-length parameter ΔR. The barrier modification ΔV_B is estimated by subtracting the potentials at first turning point R_a ($V(R_a)$) and the top of the barrier (V_B) (see Fig. 2.3). Mathematically ΔV_B in DCM is given by

$$\Delta V_B(\ell) = V(R_a, \ell) - V_B(\ell) \tag{2.52}$$

Noting that ΔV_B is a negative number, whose magnitude increases with decrease in incident energy.

Bibliography

[1] K. A. Brueckner, C. A. Levinson, and H. H. Mohmoud, Phys. Rev. **95**, 217 (1954).

[2] K. A. Brueckner, J. L. Gammel, and H. Weitzner, Phys. Rev. **110**, 431 (1958).

[3] K. A. Brueckner, A. M. Lockett, and M. Rotenberg, Phys. Rev. **121**, 255 (1961).

[4] K. A. Brueckner, J. R. Buchler, and M. Kelley, Phys. Rev. **173**, 944 (1968).

[5] T. H. R. Skyrme, Phil. Mag. **1**, 1043 (1956); Nucl. Phys. **9**, 615 (1959).

[6] D. Vautherin and D. M. Brink, Phys. Rev. C **5**, 626 (1972).

[7] C. Y. Wong, Phys. Rev. Lett. **31**, 766 (1973).

[8] R. Kumar, M. K. Sharma, and R. K. Gupta, Nucl. Phys. A **870-871**, 42 (2011).

[9] R. Kumar, M. Bansal, S. K. Arun, and R. K. Gupta, Phys. Rev. C **80**, 034618 (2009).

[10] R. K. Gupta, R. Kumar, N. K. Dhiman, M. Balasubraniam, W. Scheid, and C. Beck, Phys. Rev. C **68**, 014610 (2003).

[11] M. Balasubraniam, R. Kumar, R. K. Gupta, C. Beck, and W. Scheid, J. Phys. G **29**, 2703 (2003).

[12] R. K. Gupta, M. Balasubramaniam, R. Kumar, D. Singh, C. Beck, and W. Greiner, Phys. Rev. C **71**, 014601 (2005).

[13] B. B. Singh, M. K. Sharma, and R. K. Gupta, Phys. Rev. C **77**, 054613 (2008).

[14] M. K. Sharma, G. Sawhney, R. K. Gupta, and W. Greiner, J. Phys. G: Nucl. Part. Phys. **38**, 105101 (2011).

[15] M. Kaur, R. Kumar, and M. K. Sharma, Phys. Rev. C **85**, 014609 (2012); K. Sandhu, M. K. Sharma, and R. K. Gupta, Phys. Rev. C **85**, 024604 (2012).

[16] Rajni, R. Kumar, and M. K. Sharma, Phys. Rev C **90**, 044604 (2014); Rajni, G. Kaur, and M. K. Sharma, Int. J. Mod. Phys. E **25**, 1650091 (2016).

[17] S. Kumar and R. K. Gupta, Phys. Rev. C **49**, 1922 (1994).

[18] R. K. Gupta, W. Scheid, and W. Greiner, J. Phys. G: Nucl. Part. Phys. **17**, 1731 (1991).

[19] R. K. Gupta, in *Heavy Elements and Related New Phenomena*, edited by W. Greiner and R. K. Gupta (World Scientific, Singapore, 1999), Vol. **II**, p. 730.

[20] B. B. Singh, M. K. Sharma, and R. K. Gupta, Phys. Rev. C **77**, 054613 (2008), and earlier references there in it.

[21] R. K. Gupta, Lecture Notes in Physics, 818 *Clusters in Nuclei*, ed C. Beck, Vol. I, (Springer Verlag) p 223 (2010).

[22] S. S. Malik and R. K. Gupta, Phys. Rev. C **39**, 1992 (1989).

[23] J. Maruhn and W. Greiner, Phys. Rev. Lett. **32**, 548 (1974).

[24] R. K. Gupta, W. Scheid and W. Greiner, Phys. Rev. Lett. **35**, 353 (1975); A. Săndulescu, R. K. Gupta, W. Scheid and W. Greiner, Phys. Lett. **60B**, 225

(1976); R. K. Gupta, A. Săndulescu and W. Greiner, Phys. Lett. **67B**, 257 (1977); Rev. Roum. Phys. **23**, 51 (1978).

[25] S. Yamaji, W. Scheid, H. J. Fink and W. Greiner, Z. Phys. A **278**, 69 (1976); S. Yamaji, W. Scheid, H. J. Fink and W. Greiner, J. Phys. G: Nucl. Phys. **2**, L189 (1976); S. Yamaji, K. H. Ziegenhain, H. J. Fink, W. Greiner and W. Scheid, J. Phys. G: Nucl. Phys. **3**, 1283 (1977).

[26] R. K. Gupta, A. Săndulescu and W. Greiner, Z. Naturforsch. **32a**, 704 (1977); R. K. Gupta, C. Pirvulescu, A. Săndulescu and W. Greiner, Z. Phys. A **283**, 217 (1977); Sovt. J. Nucl. Phys. **28**, 160 (1978); R. K. Gupta, Z. Physik. A **281**, 159 (1977).

[27] A. Săndulescu, H. J. Lustig, J. Hahn, and W. Greiner, J. Phys. G: Nucl. Phys. **4**, L279 (1978); H. J. Lustig, J. A. Maruhn, and W. Greiner, J. Phys. G: Nucl. Phys. **6**, L25 (1980).

[28] H. J. Fink and W. Greiner and R. K. Gupta and S. Liran and J. H. Maruhn and W. Scheid and O. Zohni, in Proceedings of Int. Conf. on Reaction between Complex Nuclei, Nashville, 1974, **21**, (Amsterdam: North Holland), pages 2.

[29] R. K. Gupta, IANCAS Bull. (India), **6**, 2 (1990).

[30] P.-G. Reinhard and H. Flocard, Nucl. Phys. A **584**, 467-488 (1995).

[31] J. Bartel and K. Bencheikh, Eur. Phys. J. A. **14**, 179 (2002).

[32] J. Friedrich and P.-G. Reinhardt, Phys. Rev. C **33**, 335 (1986).

[33] M. Rashdan, Mod. Phys. Lett. **15**, 1287 (2000).

[34] B. K. Agrawal, S. K. Dhiman, and R. Kumar, Phys. Rev. C. **73**, 034319 (2006).

[35] P.-G. Reinhard, M. Bender, T. Buervenich, C. Reiss, J. Maruhn, W. Greiner, RIKEN Rev. **26**, 23 (2000).

[36] P. Chattopadhyay and R. K. Gupta Phys. Rev. C **30**, 1191 (1984).

[37] J. Bartel, M. Brack and M. Durang, Nucl. Phys. A **445**, 263 (1985).

[38] L. R. B. Elton, *Nuclear Sizes* (Oxford University Press, London, 1961).

[39] H. de Vries, C. W. de Jager, and C. de Vries, At. Data Nucl. Data Tables **36**, 495 (1987).

[40] S. Shlomo and J. B. Natowitz, Phys. Rev. C **44**, 2878 (1991).

[41] D. L. Hill and J. A. Wheeler, Phys. Rev. **89**, 1102 (1953); T. D. Thomas, Phys. Rev. **116**, 703 (1959).

[42] M. Balasubraniam, R. Kumar, R. K. Gupta, C. Beck, and W. Scheid, J. Phys. G **29**, 2703 (2003).

[43] R. K. Gupta, R. Kumar, N. K. Dhiman, M. Balasubraniam, W. Scheid, and C. Beck, Phys. Rev. C **68**, 014610 (2003).

[44] K. J. LeCouteur and D. W. Lang, Nucl. Phys. **13**, 32 (1959).

[45] H. Kröger and W. Scheid, J. Phys. G **6**, L85 (1980).

[46] G. Wentzel, Z. Phys. **38**, 518 (1926); H. A. Kramers, Z. Phys. **39**, 828 (1926) ; L. Brillouin, Comptes Rendus de lAcademie des Sciences **183**, 24 (1926).

[47] G. Sawhney, R. Kumar and M. K. Sharma, Phys. Rev. C **86**, 034613 (2012).

[48] A. Faessler, M. Rashdan, M. Ismail, and N. Othusuka, Nucl. Phys. A **468**, 168 (1987).

[49] As. Jensen and J. Damgaard, Nucl. Phys. A **203**, 578 (1973); M. Muenchow and W. Scheid, Nucl. Phys. A **468**, 59 (1987).

[50] M. Muenchow and W. Scheid, Phys. Lett. B **162**, 265 (1985).

[51] M. Rashdan, A. Faessler, and W. Waida, J. Phys. G: Nucl. Part. Phys. **17**, 1401 (1991).

[52] D. N. Poenaru, R. A. Gherghescu, and W. Greiner, Eur. Phys. J. A **24**, 355-359 (2005).

[53] V. M. Strutinsky, Nucl. Phys. A **95**, 420 (1967).

[54] N. J. Davidson, S. S. Hsiao, J. Markram, H. G. Miller, and Y. Tzeng, Nucl. Phys. A **570**, 61c (1994).

[55] P. A. Seeger, Nucl. Phys. **25**, 1 (1961).

[56] W. Myers and W. J. Swiatecki, Nucl. Phys. **81**, 1 (1966).

[57] G. Audi and A. H. Wapstra, Nucl. Phys. A **595**, 4 (1995).

[58] P. Möller, J. R. Nix, W. D. Myers, and W. J. Swiatecki, At. Data Nucl. Data Tables **59**, 185 (1995).

[59] R. A. Gherghescu, Phys. Rev. C **67**, 014309 (2003).

[60] R. A. Gherghescu, W. Greiner, and G. Mnzenberg, Phys. Rev. C **68**, 054314 (2003).

[61] R. K. Gupta, M. Balasubramaniam, R. Kumar, N. Singh, M. Manhas and W. Greiner, J. Phys. G: Nucl. Part. Phys. **31**, 631 (2005).

[62] M. Münchow, D. Hahn and W. Scheid, Nucl. Phys. A **388**, 381 (1982).

[63] M. J. Rhoades-Brown, V. E. Oberacker, M. Seiwert and W. Greiner, Z. Phys. A **310**, 287 (1983)

[64] Deryagin, Kolloid Z. **69**, 155 (1934).

[65] J. Blocki, J. Randrup, W. J. Swiatecki, and C. F. Tsang, Ann. Phys. (N.Y.) **105**, 427 (1977).

[66] R. K. Gupta, N. Singh, and M. Manhas, Phys. Rev. C **70**, 034608 (2004).

[67] G. Royer and J. Mignen, J. Phys. G: Nucl. Part. Phys. **18**, 1781 (1992).

[68] N. Cindro and D. Pocanic, J. Phys. G: Nucl. Part. Phys. **6**, 359-366 (1980).

[69] R. Aroumougame, N. Malhotra, S. S. Malik, and R. K. Gupta, Phys. Rev. C **35**, 3 (1987).

[70] G. Kaur, N. Grover, K. Sandhu, M.K. Sharma, Nucl. Phys. A **927**, 232 (2014); K. Sandhu, M. K. Sharma, A. Kaur, R.K. Gupta, Phys. Rev. C **90**, 034610 (2014); R. K. Gupta, M. Manhas, W. Greiner *et al.*, J. Phys. G: Nucl. Part. Phys. **36**, 115105 (2009); G. Sawhney, R. Kumar, M. K. Sharma, Phys. Rev. C **86**, 034613 (2012).

[71] S. Misicu and H. Esbensen, Phys. Rev. Lett. **96**, 112701 (2006).

[72] T. Ichikawa, K. Hagino and A. Iwamoto, Phys. Rev. C **75**, 064612 (2007).

Chapter 3

Entrance channel effects in ^{200}Pb* formed in ^{30}Si+^{170}Er, ^{16}O+^{184}W and ^{19}F+^{181}Ta reactions

3.1 Introduction

Entrance channel effect on fusion-fission dynamics has been investigated for last few decades on consistent basis. This concept draws attention because of many open questions in the related area. Depending on the entrance channel mass asymmetry and deformation involved, the dynamical path to fusion-fission process differ significantly. The fusion of two nuclei is a complex process and can be best understood via compound nucleus (CN) decay products, such as the fusion-evaporation residue (ER), intermediate mass fragment (IMF) and fusion-fission (ff) process. The ff comprises either symmetric fission, asymmetric or near- symmetric fission (nSF) and/or heavy mass fragment (HMF). In addition to CN process some non-compound processes such as, deep inelastic collision (DIC), quasi-fission (qf), incomplete-fusion (ICF) etc may also occur depending upon the beam energy, mass asymmetry and nature of projectile used. It is worth noticing that qf occurs at early stage of the collision when two fragments are linked by a neck and nucleon start shifting from

heavy fragment towards the lighter ones. The two fragments then get re-separated with same or higher mass symmetry than the entrance channel, without forming a CN. In fact, the qf process is a dynamical mechanism depending on the characteristics of the entrance channel, while CN fission is purely statistical and is determined by the temperature and angular momentum involved. The fusion-fission process of incoming channel depends upon the barrier formed by different potentials like long-range Coulomb and short range nuclear potentials. The incoming projectile must have sufficient energy to cross the barrier, which indicates that the barrier characteristics are important for studying the ff-process.

Earlier, experiments [1, 2] were performed at different center-of-mass energies ($E_{c.m.}$) ranging from 107.40 MeV to 136.96 MeV in order to measure the ER and fusion cross-section of spherical compound nucleus ^{200}Pb*, formed in reaction with ^{30}Si projectile and ^{170}Er target. Since ^{200}Pb* is a spherical and stable system, with magic Z, so it is of interest to study the role of deformation in the decay and formation of ^{200}Pb* nucleus. The same CN was formed using ^{16}O+^{184}W and ^{19}F+^{181}Ta [1, 3, 4] with $E_{c.m.}$ ranging from 77.19 MeV to 110.56 MeV. Since at ℓ=0$\hbar$, the nucleus-nucleus interaction potential for relatively asymmetric system is wider and deeper, so the measured cross-sections of the fission like and ER fragment for ^{16}O+^{184}W reaction are larger than those for ^{19}F and ^{30}Si induced reactions. These facts directly indicate the experimental signature of entrance channel effect in ^{200}Pb* nucleus, which motivate us further to study the role of entrance channel in the decay and formation of ^{200}Pb*. Since long, the Wong formula [5] is used for calculating the fusion cross-sections. In this chapter, I have used Wong formula and its extended version [6–9] to study the fusion process of ^{200}Pb*. In order to study the entrance channel dependence on the decay pattern, we used the dynamical cluster-decay model (DCM) [10–21]. This model employs neck-length parameter (ΔR) for addressing the data, which leads to required modification of the barrier at near and sub-barrier region.

In the present work, we observe that the Wong formula overestimates or underestimates the data, whereas its extended version, i.e. the ℓ-summed extended Wong model, fits the experimental fusion cross-section nicely for the three incident channels except at few energies of ^{16}O+^{184}W reaction. However, fitting is improved slightly with the inclusion of deformation effect. It is anticipated that there might be some non-compound nucleus (nCN) contribution at two or three energies for ^{16}O induced channel.

For the decay part, DCM gives a nice fit to the experimental ER and fission cross-section with spherical as well as deformed choice of fragments for the reactions ^{16}O+^{184}W, ^{19}F+^{181}Ta and ^{30}Si+^{170}Er. In order to see the difference in the decay pattern of CN, the fragmentation potential and preformation probability for spherical and deformed case of three incoming channels are worked out at comparable incident energy $E_{c.m.} \simeq 110$ MeV. The deformation effects are included upto β_2 along with the hot optimum orientations [22]. It is observed that with the inclusion of deformations, decay pattern changes from symmetric to asymmetric. Although, overall pattern of the fragmentation is similar for three channels, but some signatures of the entrance channel dependence are observed in IMF and fission region. Further, the prediction of ER and fission cross-sections at higher energies (for O and F- induced reactions) and at lower energies (for Si-induced) help us to provide comprehensive understanding regarding dynamics of ^{200}Pb*.

The chapter is organized as follows. The calculation and results are shown in section 3.2. The conclusions are given in Section 3.3.

3.2 Calculations and results

To see the entrance channel dependence in the formation and decay of CN, calculations have been done for three different channel ^{30}Si+^{170}Er , ^{16}O+^{184}W and ^{19}F+^{181}Ta forming same compound nucleus i.e. ^{200}Pb*. In Section 3.2.1, we address the fusion cross-section using Wong and ℓ-summed extended Wong model. In Sec-

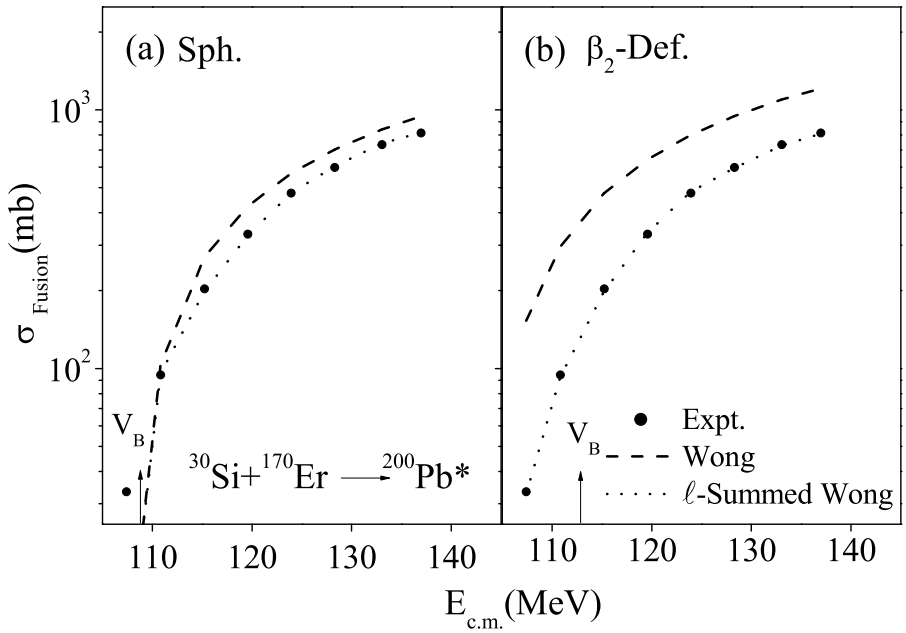

Figure 3.1: Comparison of experimental data with the calculated fusion cross-section using Wong formula and its extended version, ℓ-summed extended Wong model, for ^{30}Si+^{170}Er$\rightarrow$^{200}Pb*reaction with (a) spherical and (b) deformed choice of nuclei.

tion 3.2.2, we study the decay mechanism in the frame work of DCM. The behavior of fragmentation path, preformation profile, average total kinetic energy, and barrier modification, etc., are investigated for better understanding of dynamics involved in the chosen reactions.

3.2.1 Formation of ^{200}Pb* using the Wong formula and ℓ-summed Wong Model

Fig. 3.1 shows the comparison of fusion cross-section of ^{30}Si+^{170}Er, calculated using Wong formula and its extended version, the ℓ-summed Wong model, with experimental data. It is clear from Fig. 3.1 that though Wong formula overestimate most of the data, however its extended version, after appropriate inclusion of angular momentum effect, fits the data nicely except at lowest energy for spherical choice of fragmentation. On incorporating the deformations, this anomaly at lowest energy gets resolved and we get nice comparison with data at all the energies. Since barrier

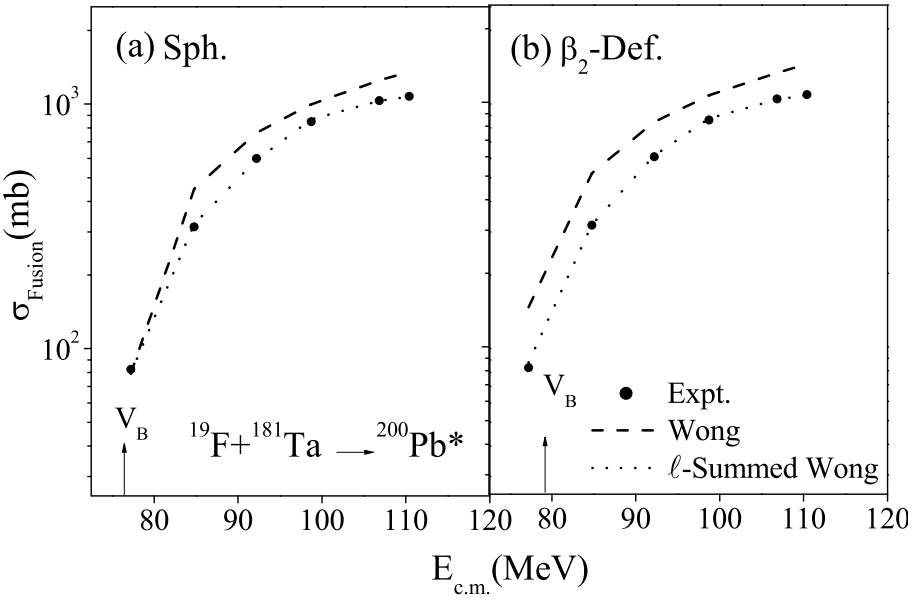

Figure 3.2: Same as Fig. 3.1 but for ^{19}F+^{181}Ta$\rightarrow$^{200}Pb* reaction.

characteristics (V_B^ℓ, R_B^ℓ and $\hbar\omega_\ell$), extracted from the potential barrier, are the main input of the Wong model and deformations modify the barrier characteristics significantly, so the inclusion of deformation effects play appreciable role in the formation of compound system ^{200}Pb*.

Fig. 3.2 and Fig. 3.3 are same as that of Fig. 3.1 but for ^{19}F+^{181}Ta and ^{16}O+^{184}W reaction respectively. Fig. 3.2 showing almost similar behavior as that of Fig. 3.1. However it is observed in Fig. 3.3 that for O-induced reaction, both the Wong formula and its extended version are not able to fit the data at few energies. This observation seems to suggest that, there is possibility of some nCN contribution or may be due to the fact that ^{16}O (projectile) and ^{200}Pb (the CN formed) are magic nuclei, so the measured cross-section are comparatively larger for this reaction. Also, the number of target neutrons for ^{16}O channel are higher (N=110) than the other two incoming reactions. Therefore the magicity associated with projectile or CN and\or higher number of neutrons in the target nucleus might be responsible for this disagreement with data.

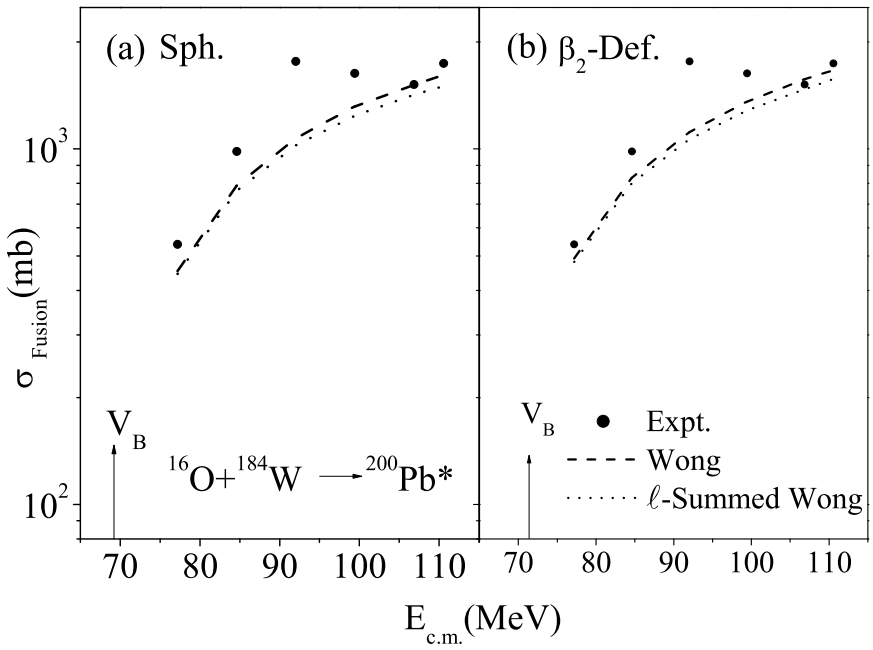

Figure 3.3: Same as Fig. 3.1 but for ^{16}O+^{184}W→^{200}Pb* reaction.

Fig. 3.4 shows the variation of the deduced maximum angular momentum (ℓ_{max}) for best fit to the experimental data as a function of $E_{c.m.}$ for spherical and deformed choice of nuclei. The ℓ_{max} increases with increase in $E_{c.m.}$ for all the chosen reactions. It is observed that with the inclusion of deformation, the variation become more smooth particularly for ^{30}Si induced reaction. One may recall that the comparison at lowest energy for this reaction was not good for spherical choice of fragmentation, which improved significantly with the inclusion of deformation effects. As a result of this, we find smooth variation of ℓ_{max} for the deformed case. At comparable $E_{c.m.}$ $\simeq$ 110 MeV different reactions seem to give different ℓ_{max} values being least for most symmetric choice (i.e. ^{30}Si induced reaction) and highest for the most asymmetric combination (i.e. ^{16}O induced reaction), independent of deformation effects.

Fig. 3.5 (a) shows the comparison of scattering potential for the three entrance channels at T=0 MeV and ℓ=0$\hbar$ using spherical fragmentation. It is clear from the graph that barrier is highest for Si- induced channel followed by F and O-induced reactions. The highest barrier of Si channel finds its origin in Coulomb

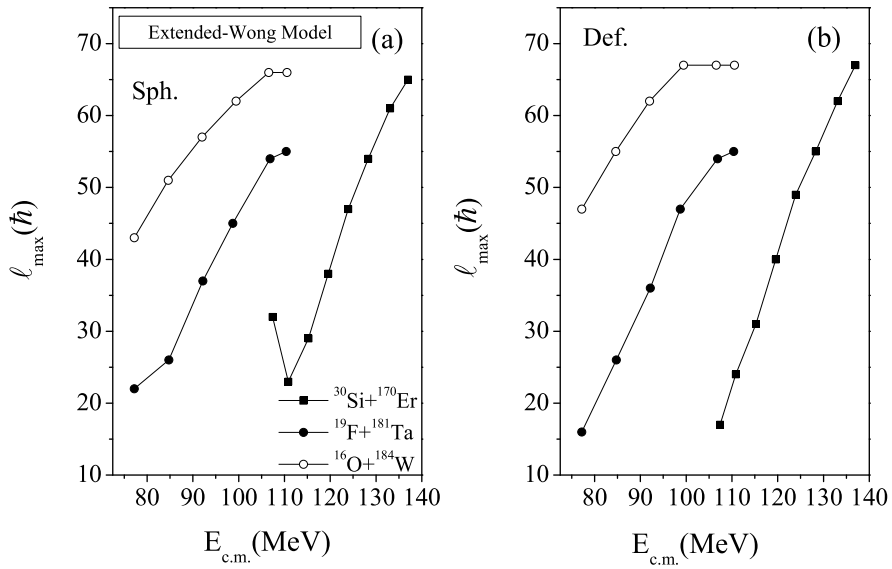

Figure 3.4: Deduced ℓ_{max}-values as a function of $E_{c.m.}$ for three incoming channels i.e. ^{30}Si+^{170}Er,^{19}F+^{181}Ta and ^{16}O+^{184}W with (a) spherical and, (b) deformed (upto β_2) fragmentation.

potential (V_c) as product of charge numbers of target and projectile is highest for Si-induced reaction (Z_1Z_2=952). The other ingredient of interaction potential i.e. the proximity potential, on the other hand plays relatively a silent role. Fig. 3.5 (b) shows the comparison of total interaction potential for the three entrance channels at $E_{c.m.} \approx 110$ MeV and their respective ℓ_{max}-values with spherical case. It is clear from the figure that the combined effect of T and ℓ become more pronounced for most asymmetric reaction (^{16}O) as one can observe that barrier height is almost constant for symmetric channel (^{30}Si+^{170}Er) while significant change is observed in F- and O-induced reaction (asymmetric reactions). Here the highest magnitude of barrier height for ^{16}O+^{184}W may be associated with larger value of ℓ_{max} along with relatively higher mass asymmetry for this reaction. Fig. 3.5 (c) is same as Fig. 3.5 (b) but with effect of β_2-deformation included. The comparative analysis of Fig. 3.5(b) with Fig. 3.5(c) clearly show that the barrier characteristics are significantly influenced with the inclusion of deformation and orientation effects. Therefore one may conclude that such effects are desirable to understand the comprehensive role

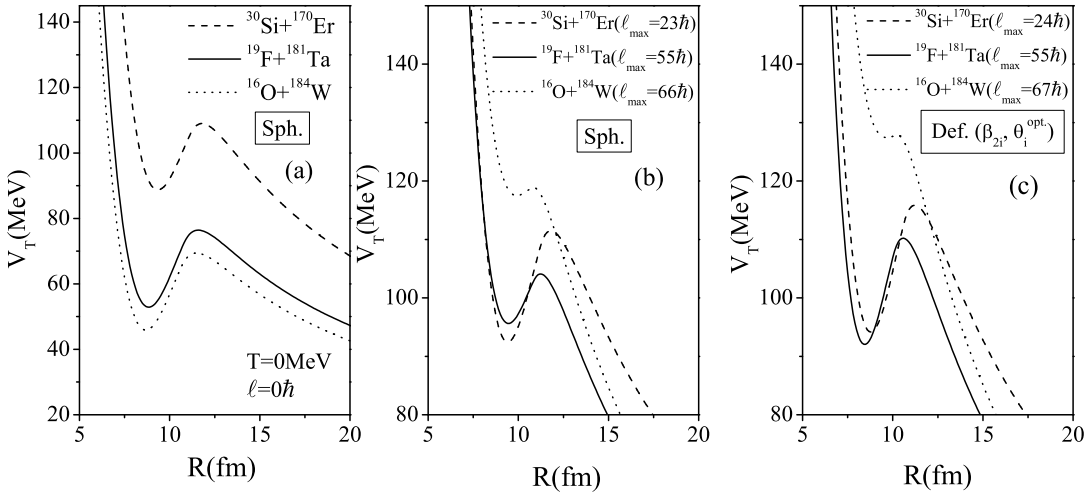

Figure 3.5: Total interaction potential V_T(MeV) as a function of R(fm), for three incoming channels i.e. ^{30}Si+^{170}Er,^{19}F+^{181}Ta and ^{16}O+^{184}W. (a) corresponds to spherical nuclei without temperature and angular momentum effects and (b), (c) at $E_{c.m.} \approx 110$ MeV (T $\neq 0$ and $\ell \neq 0$), for spherical and β_2-deformations respectively.

of formation process using different target-projectile combinations.

Since all the reactions are forming same compound nucleus, but behaving differently, it means different target-projectile combinations affect the compound nucleus formation. As mentioned above, the deformations and orientation also play a decisive role in the study of fusion cross-section of ^{200}Pb*. After studying the role of different reaction partner in the formation of ^{200}Pb*, it would be of further interest to investigates the decay path of this nucleus, which is carried out in next section.

3.2.2 Decay of ^{200}Pb* using DCM

The decay process of ^{200}Pb* formed in ^{30}Si+^{170}Er, ^{19}F+^{181}Ta and ^{16}O+^{184}W reactions, is studied using dynamical cluster-decay model (DCM) over an extensive range of incident energies. Experimental data [1–4] of ^{30}Si, ^{19}F and ^{16}O-induced reactions is available at near and above barrier energies. DCM gives a nice description of ER and ff cross-section with spherical and deformed choice of fragmentation by fitting the neck length "ΔR". The experimental and the DCM calculated ER and fission cross-section along with the corresponding neck-length and deduced maximum angular momentum at various center of mass energies are listed in Table 3.1.

Table 3.1: The evaporation-residue and Fission cross-sections for ^{200}Pb* system, calculated using the DCM at different $E_{c.m.}$'s for three different entrance channel ^{30}Si+^{170}Er,^{19}F+^{181}Ta,^{16}O+^{184}W compared with the experimental data [1–4].

$E_{c.m.}$	Temp.	ΔR (fm)		$\ell_{max}(\hbar)$	$\sigma_{Expt.}$(mb)		σ_{DCM}(mb)	
(MeV)	(MeV)	ER	Fission		ER	Fission	ER	Fission
				^{30}Si+^{170}Er→^{200}Pb* (Q$_{in}$=-58.308 MeV)				
107.40	1.508	1.682	0.710	123	31.98	1.37	31.30	1.382
110.84	1.560	1.750	0.878	125	80.08	14.41	81.30	14.68
115.24	1.623	1.796	1.007	127	140.33	63.17	139.0	63.60
119.57	1.683	1.843	1.080	127	202.34	128.34	201.0	128.6
123.93	1.741	1.841	1.154	129	217.34	259.80	216.0	260.0
128.31	1.797	1.838	1.195	130	216.34	382.30	216.0	382.0
133.06	1.856	1.835	1.214	131	210.0	523.91	210.0	522.0
136.96	1.903	1.834	1.231	131	202.34	611.29	202.0	612.0
				^{19}F+^{181}Ta→^{200}Pb* (Q$_{in}$=-23.689 MeV)				
77.21	1.5745	1.726	0.784	124	77.08	5.16	77.8	5.23
84.75	1.6802	1.865	0.990	126	313.97	61.35	314.0	61.40
92.19	1.7783	1.887	1.104	128	396.78	203.62	396.0	204.0
98.72	1.8601	1.900	1.193	129	425.64	423.16	425.0	424.0
106.84	1.9570	1.884	1.216	132	401.45	633.66	400.0	626.0
110.40	1.9979	1.864	1.227	133	342.78	733.48	342.0	734.0
				^{16}O+^{184}W→^{200}Pb* (Q$_{in}$=-24.204 MeV)				
77.19	1.5668	1.938	0.891	124	521.50	23.68	523.0	22.8
84.61	1.6713	1.997	1.05	125	861.81	121.17	789.0	121.0
92.02	1.7695	2.075	1.151	128	1473.38	318.80	1470.0	320.0
99.43	1.8625	2.04	1.20	130	1153.96	498.99	1150.0	502.0
106.86	1.9512	2.0	1.223	131	853.08	677.26	850.0	678.0
110.56	1.9939	2.035	1.227	132	1067.28	698.27	1070.0	698.0

In order to see the decay pattern with spherical and deformed choice of nuclei, the fragmentation potential and preformation profile are worked out at $E_{c.m.} \approx 110$ MeV.

Fig. 3.6(a) shows the comparison of fragmentation potential V(R) as a function of mass number A_2 at $E_{c.m.} \approx 110$ MeV for three different entrance channels with spherical choice of fragmentation. Fig. 3.6(b) is same as that of Fig. 3.6(a) but with effect of β_2-deformation included. Fig. 3.6(a) shows that, at ℓ=0$\hbar$ the behavior of potential energy surface is quite similar for the three entrance channels. However with increase in ℓ-value, the fragmentation behavior changes significantly. Further-

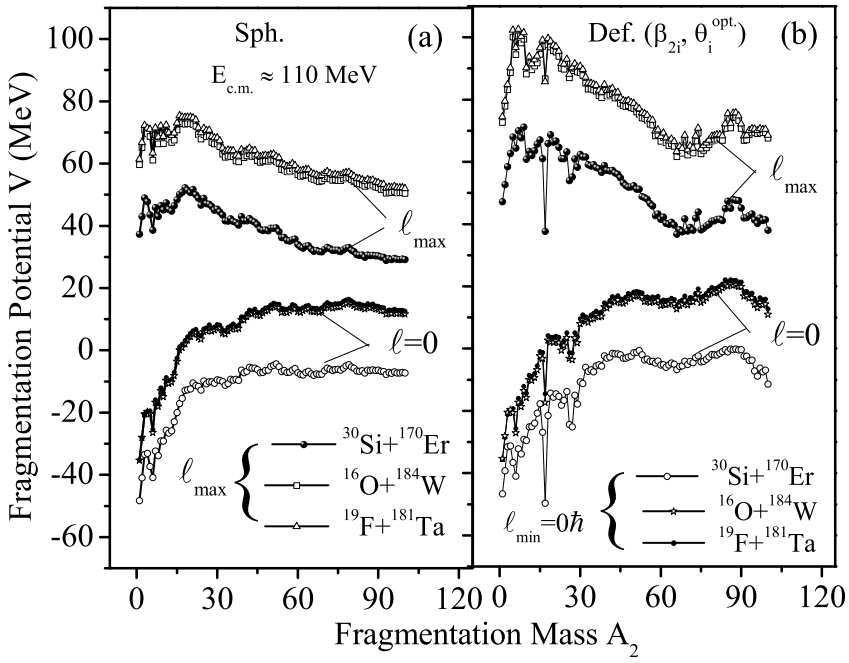

Figure 3.6: Fragmentation potential V(MeV) as a function of fragment mass A_2 at fixed $E_{c.m.}$ for three entrance channels with (a) spherical and (b) deformed choice of fragmentation. (For ℓ_{max} see Table 3.1)

more at ℓ=0$\hbar$, ER contribution is dominating while at ℓ_{max} the symmetric fission products start competing with ER. It is observed that the magnitude of fragmentation potential is lower for ^{30}Si+^{170}Er. It is relevant to mention here that, the Q-value and the asymmetry of the reaction play significant role in deciding the decay pattern of a compound system. The change in behavior of potential energy surface is also observed with the inclusion of deformations. Also the mode of fission distribution shifts from symmetric to asymmetric as we move from spherical to deformed choice of fragmentation.

For spherical choice, the fission window is seen for A_2=65-100 for all the three entrance channels. However with the inclusion of deformations the fragmentation profile changes significantly particularly in fissioning region. The Si-induced reaction exhibits double humped structure where symmetric as well asymmetric dips are distinctly visible respectively at A_2=58 to 84 and A_2=91 to 100. On the other hand F- induced and O-induced reactions show prominence of asymmetric fission window with almost negligible contribution of symmetric fragments. This point is

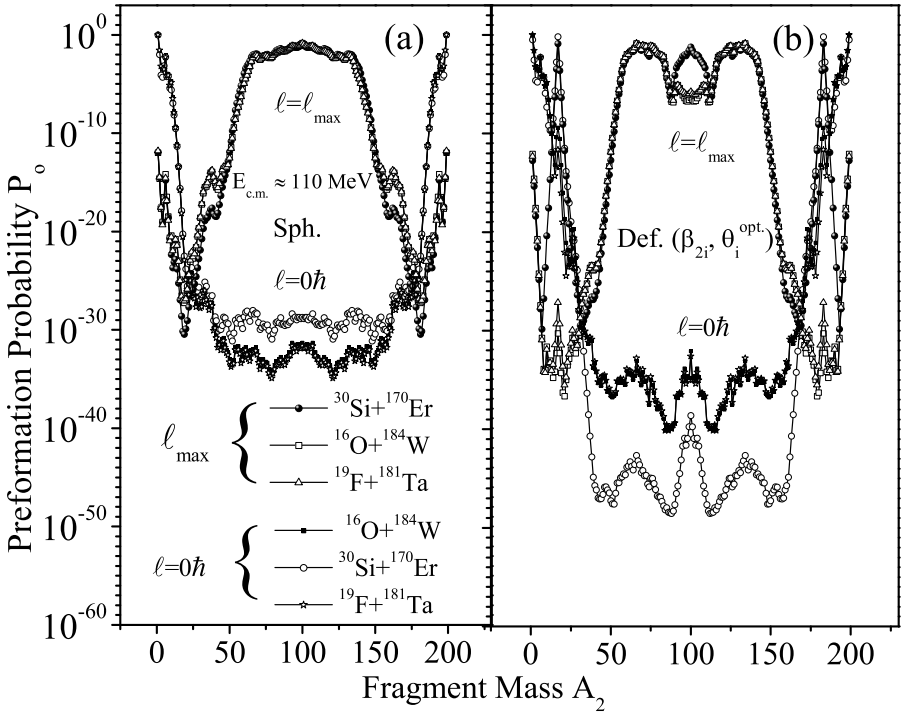

Figure 3.7: Preformation Probability P_0 as a function of fragment mass A_2 for three different incoming channels for (a) spherical and (b) deformed choice of nuclei. (For ℓ_{max} see Table 3.1)

emphasized further in the behavior of preformation factor depicted in Fig.3.7.

It is clear from Fig.3.7 that the behavior of preformation probability P_0 with fragment mass A_2 is symmetric for spherical choice of fragment, however it shows to asymmetric fission for deformed choice of fragments. Although the behavior of preformation probability with A_2 is similar for all three reactions for spherical choice of fragments but same is not true for deformed fragmentation. From Fig. 3.7(b) one can clearly observe that the preformation profile of ^{30}Si channel is quite different than that for ^{19}F and ^{16}O induced reactions. Therefore, it is evident that the deformation and orientation degree of freedom play an important role in the decay mechanism of ^{200}Pb* and the entrance channel dependence seem evident in the deformed fragmentation process. Henceforth one may conclude that by varying target-projectile combination, significant modification is observed in the decay path of ^{200}Pb* nucleus.

Fig. 3.8 shows the variation of neck-length parameter ΔR as a function of $E_{c.m.}$

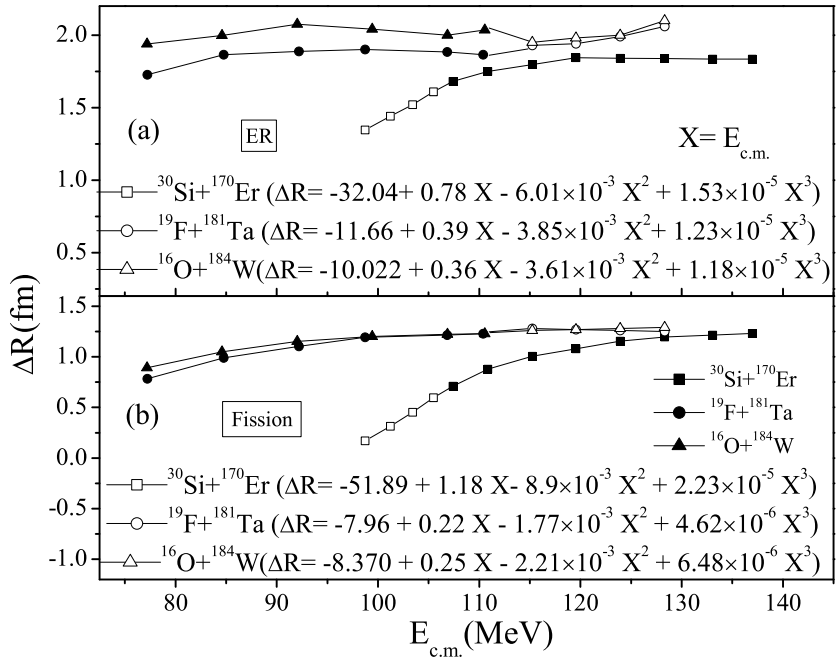

Figure 3.8: Neck-length parameter ΔR as a function of $E_{c.m.}$ for spherical choice of nuclei of CN ^{200}Pb* formed by using three entrance channels. Filled and open symbols mark calculations with DCM and predicted values of ΔR by polynomial fitting of order three respectively for (a) ER and (b) fission cross-section.

for the ER (Fig. 3.8 (a)) and fission cross-section (Fig. 3.8 (b)) for the chosen entrance channels using spherical choice of fragmentation. The comparison of Fig. 3.8 (a) and Fig. 3.8 (b) clearly show that ΔR for ER process is higher than that for fission, independent of the choice of entrance channel. Using the systematics of ΔR values for experimental data, the neck-length parameter ΔR is extrapolated by using polynomial fitting of order 3. In other words we have estimated the ΔR values for energies above 110 MeV for ^{16}O and ^{19}F induced reactions and energies below 107 MeV for relatively symmetric ^{30}Si induced channel, so as to obtain cross-sections in energy range $E_{c.m.}$ =98-128 MeV for all the three channel. The filled symbols in Fig. 3.8 correspond to fitted ΔR values in reference to data of [1–4], and the open symbols correspond to the extrapolating ΔR values obtained using polynomial fitting. The corresponding cross-sections and ℓ-values are predicted and the same are listed in Table 3.2. An experimental verification is called for these predicted cross-sections. The main purpose of extrapolation of ΔR in Fig. 3.8 is to provide

Table 3.2: Predicted ER and Fission cross-sections for ^{200}Pb* system by polynomial fitting of order 3, using the DCM at different $E_{c.m.}$'s for three different entrance channel ^{30}Si+^{170}Er,^{19}F+^{181}Ta and ^{16}O+^{184}W.

$E_{c.m.}$	Temp.	ΔR (fm)		ℓ_{max}	σ_{DCM}(mb)	
(MeV)	(MeV)	ER	Fission	($\hbar$)	ER	Fission
			^{30}Si+^{170}Er$\rightarrow^{200}$Pb*			
98.72	1.3663	1.345	0.170	121	0.198	2.16×10^{-3}
101.21	1.412	1.44	0.315	121	0.902	1.13×10^{-2}
103.42	1.447	1.52	0.453	122	3.42	7.68×10^{-2}
105.47	1.479	1.61	0.595	123	13.2	4.82×10^{-1}
			^{19}F+^{181}Ta$\rightarrow^{200}$Pb*			
115.24	2.052	1.93	1.28	134	549.0	940.0
119.57	2.099	1.94	1.27	134	552.0	882.0
123.93	2.146	1.99	1.26	135	830.0	788.0
128.31	2.192	2.06	1.25	135	1150.0	722.0
			^{16}O+^{184}W$\rightarrow^{200}$Pb*			
115.24	2.046	1.95	1.26	131	476.0	860.0
119.57	2.094	1.98	1.27	135	803.0	884.0
123.93	2.141	2.00	1.28	138	1060.0	886.0
128.31	2.187	2.10	1.29	136	1050.0	842.0

the ER and fission cross-section in an comprehensive energy range i.e. $E_{c.m.}$ =98-128 MeV.

To study the temperature dependence on decay structure of ^{200}Pb*, the comparison of preformation profile P_0 is made at extreme common energies i.e. at 98 MeV and 128 MeV respectively using spherical fragmentation for all the three channels. From Fig. 3.7(a), symmetric fragments contribution is evident for all the chosen reactions. However, Fig. 3.9 shows clearly that though structure is almost same at extreme energies, but significant difference in magnitude is observed in Si-channel as shown in Fig. 3.9(a). It means that, the effect of energy is more prominent in symmetric channel as compared to asymmetric channels (see Fig. 3.9(a) and Fig. 3.9(b)). The estimated neck length parameter values and consequent prediction of cross-sections can be exploited to have further understanding of the fission dynamics

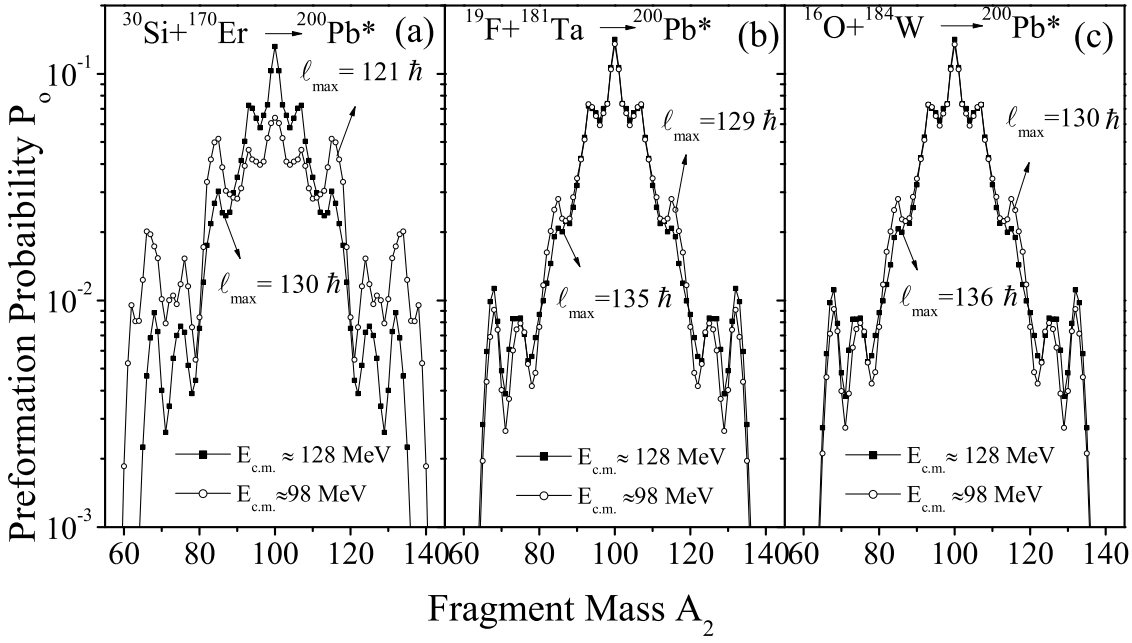

Figure 3.9: Preformation Probability P_0 as a function of fragment mass A_2 plotted at $E_{c.m.} = 98$ MeV and 128 MeV for (a) ^{30}Si+^{170}Er (b) ^{19}F+^{181}Ta and (c) ^{16}O+^{184}W reactions.

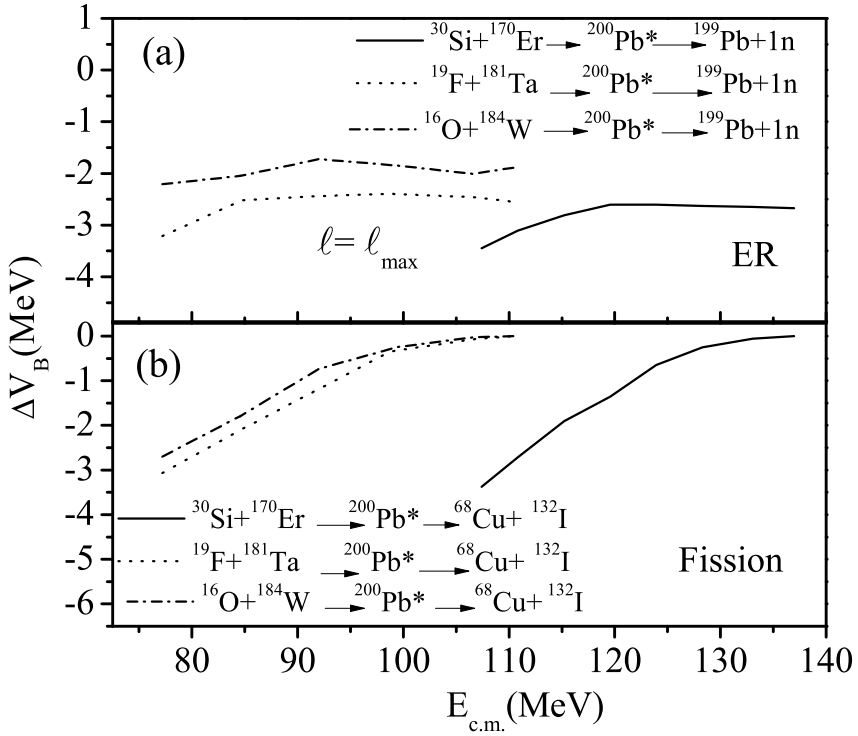

Figure 3.10: Barrier-lowering parameter ΔV_B varying as center of mass energy $E_{c.m.}$ for highest contributing fragments at $\ell = \ell_{max}$ (a) ER (b) Fission

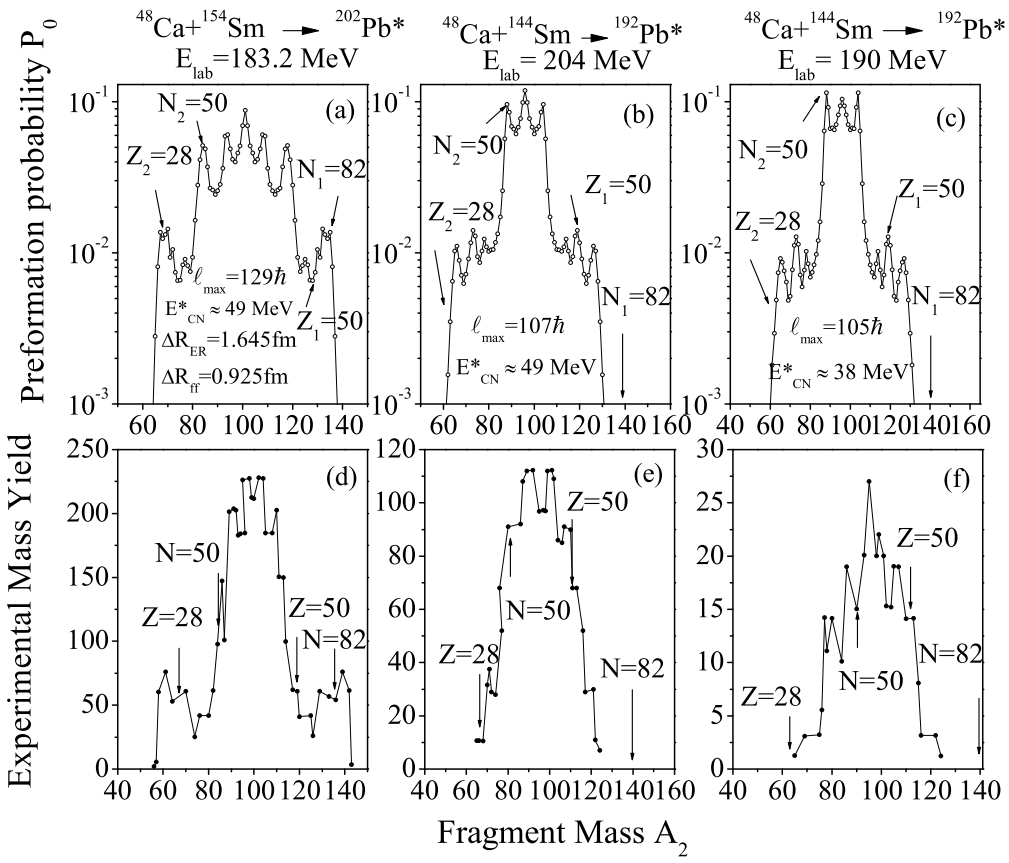

Figure 3.11: Preformation Probability P_0 (upper panel) and Experimental Mass Yield (lower panel), plotted as a function of fragment mass A_2.

of ^{200}Pb*. The barrier modification effect is also worked out as an in-built property of fitting parameter, the neck-length parameter ΔR. The barrier modification ΔV_B depends on the barrier height V_B and barrier penetration point $V(R_a)$ as shown in Eq.(2.52) of chapter 2. Fig. 3.10(a) and Fig. 3.10(b) show the variation of barrier lowering parameter ΔV_B as a function of $E_{c.m.}$ for ER and fission cross-sections respectively. One may clearly see that ΔV_B variation follow the trend of neck length parameter "ΔR" depicted in Fig. 3.8. Henceforth, it is evident that, barrier modification is an inbuilt parameter in DCM, which is uniquely fixed in reference to ΔR values and is of huge importance to address the data particularly at near and below barrier region.

Finally, in order to study the behavior of different isotopes around ^{200}Pb* region, ^{192}Pb* and ^{202}Pb* nuclei formed via ^{48}Ca+^{144,154}Sm reactions are investigated in the framework of DCM. Preformation probability P_0 (equivalently the mass yield) and

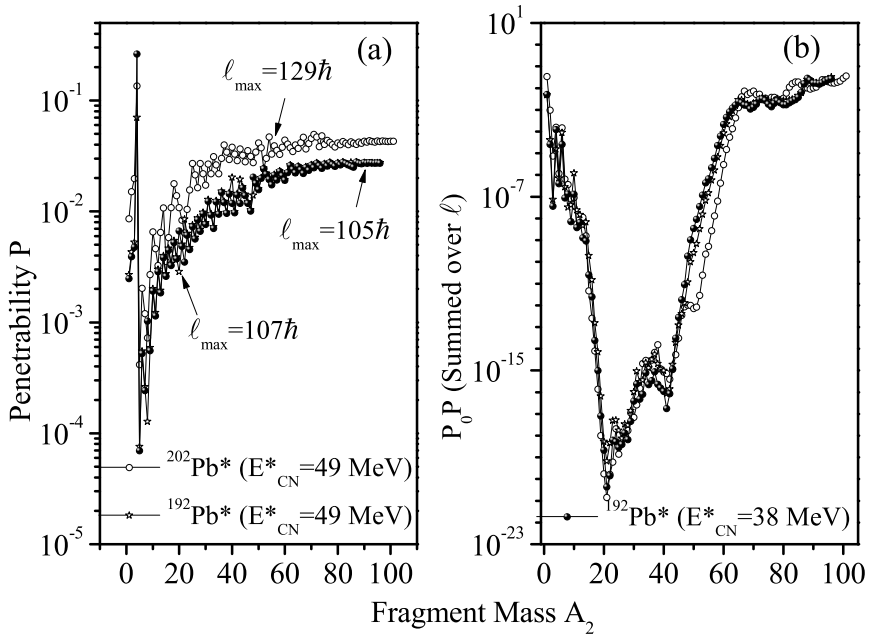

Figure 3.12: (a) Penetrability P at ℓ=ℓ_{max} and (b) The ℓ-summed P_0P as a function of fragment mass A_2 for two incoming channels.

average total kinetic energy <TKE> are calculated for decaying fragments of the above mentioned reactions at E_{lab}=183.2 MeV for ^{202}Pb* and at E_{lab}=204 MeV, 190 MeV for ^{192}Pb*. The available evaporation residue and fission data [23, 24] of ^{48}Ca+^{154}Sm→^{202}Pb*→A_1+A_2 reaction is addressed by taking ΔR_{ER}= 1.645fm and ΔR_{ff}=0.925fm. Since, no experimental data is available for ^{48}Ca+^{144}Sm reaction, so same neck-length is used for calculating preformation probability P_0, penetrability P, and <TKE>. The relatively higher values of angular momentum ℓ_{max} are due to the moment of inertia in sticking limit (for further details see Ref. [25]). As, nuclear structure effects appear in DCM via preformation probability P_0, so the structural pattern of experimental mass yield is compared with P_0, in Fig. 3.11. The preformation factor of ^{202}Pb* at E^*_{CN}=49 MeV is shown in Fig. 3.11(a) and that for ^{192}Pb* at E^*_{CN}=49 MeV and E^*_{CN}=38 MeV in Fig. 3.11(b) and Fig. 3.11(c) respectively. A near symmetric mass distribution is observed, with emergence of shoulders corresponding to magic shells at Z_2=28, N_2=50 and N_1=82. These secondary peaks are relatively suppressed for neutron deficient ^{192}Pb* nucleus in agreement with [26, 27].

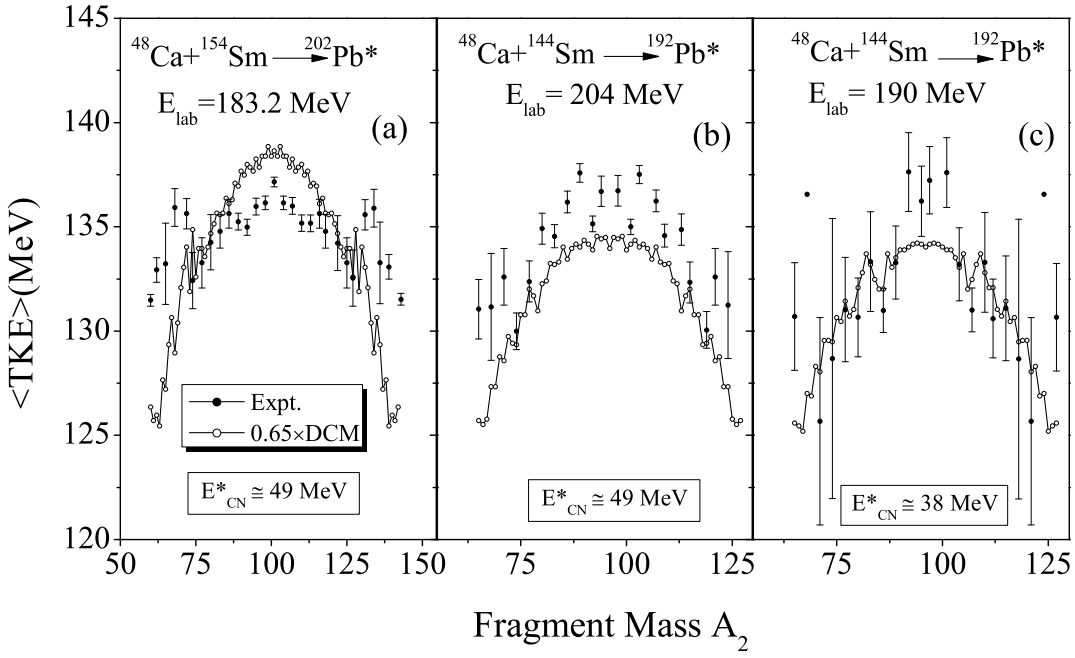

Figure 3.13: Average total kinetic energy <TKE> and available experimental data plotted as a function of fragment mass A_2.

The preformation probability plotted in upper panel of Fig. 3.11 finds nice comparison with structural distribution of mass yields plotted in the lower panel.

Fig. 3.12(a) shows the barrier penetrability P as a function of fragment mass A_2 at maximum angular momentum for two channels. It imparts following information. (i) The penetrability P of light mass fragments particularly for α-particle is significantly large. (ii) In general P increases as a function of fragment mass and starts saturating in fission region. (iii) Independent of entrance channel effect the α nucleus structure is visible in IMF and HMF region, which start disappearing near the fission window. In Fig. 3.12(b), summed up P_0P is plotted as a function of fragment mass A_2 for two incoming channels i.e. ^{48}Ca+^{154}Sm at E^*_{CN}=49 MeV and ^{48}Ca+^{144}Sm at E^*_{CN}=49 and 38 MeV. In other words, for each fragment, the ℓ-summation of P_0P is worked out over all contributing angular momentum values upto ℓ_{max} to demonstrate the collective role of these quantities. It is observed that the product P_0P provide an interesting structure as function of fragment mass A_2. One may notice that this structural distribution is mainly influenced via the preformation profile as the penetrability contributes mainly towards the magnitude as

described in earlier work [28]. A closure look of Fig. 3.12(b), clearly show that the ER and fission cross-sections compete each other as, P_0P product is highest for these fragments. This observation is in agreement with measured data of Ref. [23,24]. The chosen reaction channels seems to impart similar behavior for ER to fission region.

In Fig. 3.13, the average total kinetic energy <TKE> of two systems is plotted as fragment mass A_2. The calculated <TKE> is higher in magnitude, which suggests that comparatively smaller ℓ-values contribute towards <TKE> calculations, as depicted in [29, 30]. So in order to compare the DCM calculated <TKE> values with experimental data, a scaling factor of 0.65 is used as shown in Fig. 3.13. After rescaling, the calculated <TKE> seem to provide reasonable comparison with the experimental data.

3.3 Conclusions

In this chapter, the formation and decay process of ^{200}Pb* formed via three different entrance channels i.e. ^{30}Si+^{170}Er, ^{19}F+^{181}Ta and ^{16}O+^{184}W is addressed. Calculations have been done in the frame work of Wong model and DCM to investigate respectively the fusion and decay path of ^{200}Pb* using spherical and deformed choice of fragments. The ℓ-summed Wong model is shown to give reasonable description of experimental data and deformation effects seem to influence the formation process of ^{200}Pb* nucleus. The entrance channel dependence is explored in context of deformation and angular momentum effects. On the other hand dynamical cluster decay approach is used to give description of ER and fission cross-section over wide range of incident energies, by empirically fitting the neck-length parameter ΔR, which incorporate the neck formation effects. The deformations and orientation effects are shown to play significant role in the decay process as well. Beside this some signature of entrance channel dependence is seen in the deformed fragmentation process of ^{200}Pb* nucleus. The ER and fission cross-sections are predicted for all the three channels. An experimental verification is called for predicted cross-sections in en-

ergy range $E_{c.m.}$ = 98-128 MeV. Finally the behavior of neighboring isotopes $^{192}Pb^{*}$ and $^{202}Pb^{*}$ is analyzed in terms of total average kinetic energy, penetrability and mass yield distribution patterns.

After addressing the formation and decay paths of $^{200}Pb^{*}$ formed via various heavy ion induced reactions, the dynamical cluster decay model is further applied to explore the isospin and deformation effects on lighter nuclei such as Zr, Kr, Sn etc by fixing the $^{16,18}O$ nuclei as incoming projectiles (beam), and the results obtained are discussed in next chapter.

Bibliography

[1] D. J. Hinde, J. R. Leigh, J. O. Newton, W. Galster, and S. Sie, Nucl. Phys. A **385**, 109 (1982).

[2] G. Mohanto *et al.*, Nucl. Phys. A **890-891**, 62-76 (2012).

[3] P. D. Shidling *et al.*, Phys. Rev C **74**, 064603 (2006).

[4] J. S. Forster, I. V. Mitchell, J. U. Andersen, A. S.Jensen, E. Laegsgaard, W. M. Gibson, and K. Prichett, Nucl. Phys. A **464**, 497 (1987).

[5] C. Y. Wong, Phys. Rev. Lett. **31**, 766 (1973).

[6] R. Kumar, M. Bansal, S. K. Arun, and R. K. Gupta, Phys. Rev. C **80**, 034618 (2009).

[7] R. Kumar, Phys. Rev. C **84**, 044613 (2011).

[8] D. Jain, R. Kumar, M. K. Sharma and R. K. Gupta, Phys. Rev. C **85**, 024615 (2012).

[9] D. Jain, R. Kumar, and M. K. Sharma, Phys. Rev. C **87**, 044612 (2013).

[10] B. B. Singh, M. K. Sharma, and R. K. Gupta, Phys. Rev. C **77**, 054613 (2008).

[11] R. Kumar, and R. K. Gupta, Phys. Rev. C **79**, 034602 (2010).

[12] R. K. Gupta, in *Cluster in Nuclei*, Lecture Notes in Physics 818, Vol. I, edited by C. Beck (Springer-Verlag, Berlin, 2010), p. 223.

[13] R. K. Gupta, S. K. Arun, R. Kumar, and M. Bansal, Nucl. Phys. A **834**, 176c (2010).

[14] M. K. Sharma, S. Kanwar, G. Sawhney, R. K. Gupta, and W. Greiner, J. Phys. G: Nucl. Part. Phys. **38**, 055104 (2011).

[15] M. Kaur, R. Kumar, and M. K. Sharma, Phys. Rev. C **85**, 014609 (2012).

[16] K. Sandhu, M. K. Sharma and R. K. Gupta, Phys. Rev. C **85**, 024604 (2012).

[17] G. Kaur and M. K. Sharma, Phys. Rev. C **87**, 044601 (2013).

[18] M. Kaur and M. K. Sharma, Phys. Rev. C **85**, 054605 (2012).

[19] G. Sawhney, R. Kumar, and M. K. Sharma, Phys. Rev. C **86**, 034613 (2012).

[20] G. Kaur, D. Jain, R. Kumar and M. K. Sharma, Nucl. Phys. A **916**, 260-274 (2013).

[21] R. Kumar, K. Sandhu, M. K. Sharma and R. K. Gupta, Phys. Rev. C **87**, 054610 (2013).

[22] R. K. Gupta, M. Balasubramanium, R. Kumar, N. Singh, M. Manhas, and W. Greiner, J. Phys. G: Nucl. Part. Phys. **31**, 631 (2005).

[23] A. M. Stefanini *et al.*, Eur. Phys. J. A **23**, 473 (2005).

[24] G. N. Knyazheva *et al.* Phys. Rev. C **75**, 064602 (2007).

[25] G. Sawhney, R. Kumar, Rajni and M. K. Sharma AIP. Conf. Proc. **1524**, 174 (2013).

[26] M. G. Itkis *et al.*, Nucl. Phys. A **724**, 136-147 (2004).

[27] S. Kanwar *et al.*, Int. J. Mod. Phys. E **18**, 1453-1467 (2009).

[28] M.Sharma *et al.*, J. Phys. G: Nucl. Part. Phys. **38**, 105101 (2011).

[29] K. Sandhu *et al.* ,Nucl.Phys. A **921**, 114-130 (2013).

[30] B. B. Singh *et al.*, Int. J. Mod. Phys. E **15**, 699 (2006).

Chapter 4

Decay of Zr, Kr and Sn isotopes formed in ^{16,18}O-induced reactions

4.1 Introduction

In previous chapter, the entrance channel effects were explored while addressing the dynamics of heavy mass nucleus ^{200}Pb*. Here in present chapter, the emphasis is made on the dynamical behavior of light mass systems such as Kr, Zr and Sn isotopes formed via ^{16,18}O induced reactions. The role of iso-spin (N/Z ratio) and deformations is probed by analyzing the decay patterns of various nuclei. In all these studies, the excitation energy (temperature) and angular momentum effects are duly examined.

In order to investigate different phenomena in nuclear physics, low energy heavy ion reactions have been extensively worked out during last few decades. The vigorous research carried out in this zone aided in further understanding of nuclear structure and associated dynamical aspects which are of great importance for the comprehensive analysis of diverse reaction mechanisms. To have an apparent picture of various aspects, the reaction dynamics have been explored under various extreme conditions and had eventually led to numerous interesting nuclear phenomena such as production of exotic nuclei, super heavy synthesis, execution of reactions with

loosely bound and/or tightly bound nuclei, influence of impact parameter, shell closure, deformation and orientation effects etc. All theses aspects provide an opportunity to understand the nuclear reaction dynamics and related structure effects. Despite of prolonged efforts and extensive work in this area, the nuclear reaction dynamics continues to captivate our interest further and inspires to explore the cause of occurrence and consequences of various other interesting phenomena observed in this domain.

The dynamics of nuclear reaction can be better understood by carrying out a systematic study of various decay processes of nuclei formed in heavy ion reactions. In view of this, the work presented in this chapter involves the study of decay cross-sections of various nuclei in mass range A $\sim$ 76 - 110, formed in ^{16}O and ^{18}O induced reactions. Recently an experiment [1] was conducted to study the formation of Zr compound nucleus using stable magic ^{16}O projectile and medium mass ^{76}Ge target. The complete fusion cross-sections with major contribution from evaporation residue are measured over a wide range of center-of-mass energies, $E_{c.m.}$ =31.2-50.1 MeV. Interestingly, the fusion cross-sections of Zr isotopes formed via the same reaction channel i.e. ^{16}O+^{70,72,74,76}Ge were also examined in another experiment [2] at similar energy range. In addition to this, the fusion cross-sections for the ^{92}Zr* isotope formed via ^{18}O induced reaction were also measured in [1].

Based on these experiments, a comprehensive theoretical description of decay processes and factors influencing the dynamics of ^{16}O+^{70,72,74,76}Ge and ^{18}O+^{74}Ge reactions is studied using the dynamical cluster decay model (DCM) [3–8]. Generally, the fusion cross-sections are considered to have contribution from both light particle (LP) [σ_{LP} involving emission of neutron, proton, alpha particle with $A_2\leq$ 4], and the fission cross-section, $\sigma_{fission}$. Beside this, one may have significant contribution from the intermediate mass fragments (IMF)(5$\leq$A$_2\leq$20), as such rare decay mechanism do contribute in light and intermediate mass region. Therefore σ_{fusion}=σ_{LP}+σ_{IMF}+$\sigma_{fission}$. However, for the nuclei under consideration, the σ_{fusion}

have major contribution from σ_{LP} alone, while the contribution of σ_{IMF} and $\sigma_{fission}$ is suggested to be small. It is worth mentioning that the DCM having the effect of deformations and optimum orientations [9] included in it, treats all decay processes [i.e., light particle (LPs), intermediate mass fragments (IMFs), and symmetric/asymmetric fission fragments] on equal grounding. The detailed analysis of temperature, angular momentum effects, preformation factor, barrier modification, etc., is worked out in context of the reactions under investigation. Moreover, the systematic study of even mass Zr isotopes extend a possibility to explore the role of deformation/orientation degree of freedom and effect of iso-spin (N/Z ratio) along with the option to address entrance channel effect for $^{92}Zr^*$ system formed via $^{16}O+^{76}Ge$ and $^{18}O+^{74}Ge$ reactions.

In addition to this, the influence of ^{16}O and ^{18}O projectile is analysed while addressing the dynamics of relatively lighter mass $^{76}Kr^*$ nucleus having large quadrupole deformation (β_2=0.4) as compared to $^{92}Zr^*$ nucleus (β_2=0.053). In view of this, $^{76}Kr^*$ [10] system formed via two incoming channels i.e. $^{16}O+^{60}Ni$ and $^{18}O+^{58}Ni$, provides another opportunity to examine the role of entrance channel, within energy range similar to that of Zr^* isotopes. Apart from this, the role of projectile and isospin (N/Z ratio of CN) is further explored for decay of proton magic $^{108,110}Sn^*$ [11] isotopes formed in $^{16}O+^{92}Mo$ and $^{18}O+^{92}Mo$ reactions respectively.

The motivation of the present study is to analyze the decay patterns of deformed and spherical magic nuclei formed in $^{16,18}O$ induced reactions, as it may impart useful information regarding the overall behavior of reaction dynamics. Thus, our main aim in the present work is (i) to address the contribution of dominant LP decay mode for Zr, Kr and Sn isotopes. (ii) to explore the contribution of IMF and fission channels, if any (iii) to analyze the role of deformations and carry out comparative study of various even mass Zr isotopes and (iv) to study the role of entrance channel for deformed $^{92}Zr^*$ and $^{76}Kr^*$ systems and role of projectile mass for spherical magic Sn nuclei. In all these studies the effect of excitation energy or

equivalently temperature is duly incorporated.

The chapter is organized as follows. The calculations and results are presented in Section 4.2. The conclusions drawn are discussed in Section 4.3.

4.2 Calculations and Results

In this section, the fusion excitation functions of $^{86,88,90,92}Zr^{*}$ nuclei formed in $^{16}O+^{70,72,74,76}Ge$ reactions are studied using DCM in terms of LP, IMF and fission decay modes. To analyze the dynamics of Zr isotopes, the potential energy surfaces (PES) are analyzed in terms of fragmentation potential which helps to understand the forces acting on the fragments (originating from different potential components) and thus estimating the relative stability of decaying fragments. The influence of such fragmentation interaction is then exploited in terms of preformation behavior of decaying fragments. For the intermediate mass Zr nucleus, the role of deformation and orientations is investigated by taking into account spherical choice of fragments and with inclusion of quadrupole deformation β_{2i} in reference to optimum (θ_i^{opt}) orientation approach [9]. It is evident that, for coplanar nuclei, the orientation gets optimized (uniquely fixed) by the signs of their quadrupole deformations. These optimum orientations are obtained for hot compact (and cold elongated) configuration of any two colliding nuclei. In the present work, the orientations are taken from Table 1 of [9]. Also, the entrance channel dependence is examined for $^{92}Zr^{*}$ system formed via $^{16}O+^{76}Ge$ and $^{18}O+^{74}Ge$ channels. Similar results are further tested for relatively light mass $^{76}Kr^{*}$ system formed via $^{16}O+^{60}Ni$ and $^{18}O+^{58}Ni$ reactions. Besides this, the role of projectile mass is also investigated for $^{108,110}Sn^{*}$ nuclei. This section is divided into three parts where the decay of Zr isotopes addressed in section-4.2.1, followed by investigation of entrance channel effects in section-4.2.2. Finally the effect of projectile mass is explored in section-4.2.3 of this section.

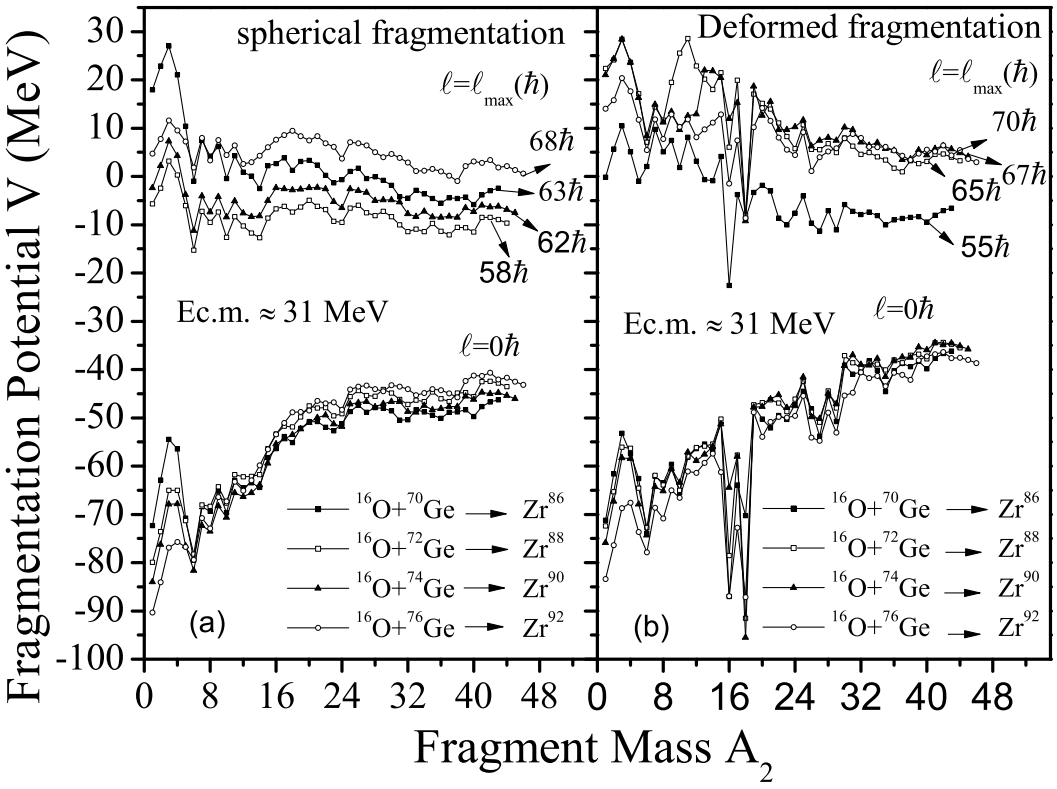

Figure 4.1: Fragmentation potential V(MeV) as a function of fragment mass A_2 for decay of $^{86-92}$Zr* isotopes, plotted at extreme $\ell(\hbar)$ values for (a) spherical and (b) deformed choice of nuclei.

4.2.1 Isotopic analysis of Zr-nuclei formed in ^{16}O-induced reactions

For a comparative study of the decay mechanism of various Zr isotopes, the calculations are carried out for ^{86,88,90,92}Zr* nuclei at comparable lowest as well as highest center of mass energy i.e. $E_{c.m.}\sim$ 31.0 MeV and $E_{c.m.}\sim$ 48.0 MeV. Fig. 4.1 shows the fragmentation potential V(A_2) at $E_{c.m.}\sim$ 31.0 MeV, for ^{16}O+^{70,72,74,76}Ge reactions giving $^{86-92}$Zr* compound nuclei, at extreme ℓ values, i.e. ℓ=0$\hbar$ and ℓ=$\ell_{max}(\hbar)$. In order to study the role of deformations, we have plotted the fragmentation potential for spherical approach and with inclusion of quadrupole (β_{2i}) deformation as shown in Fig. 4.1(a) and Fig. 4.1(b) respectively. The characteristic behavior of the fragmentation potential for both cases is different at two extreme ℓ-values. At lower ℓ-values the LPs form the dominant decay path where as the IMF and fission

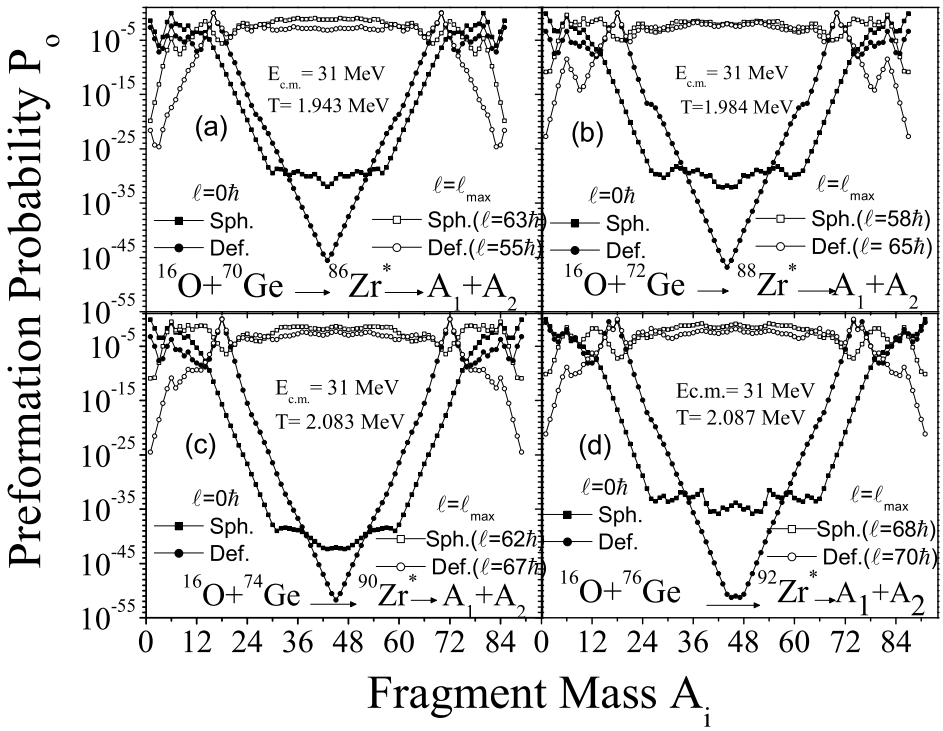

Figure 4.2: Variation of Preformation probability P_0 as a function of fragment mass, for the decay of Zr isotopes, plotted for $\ell = 0\hbar$ and $\ell = \ell_{max}$ values, for spherical and deformed nuclei at $E_{c.m.}$=31 MeV

Table 4.1: The ER and IMF cross-sections for five Compound systems, calculated using the DCM at lowest $E_{c.m.}$=31.0 MeV compared with the experimental data [1, 2]. It may be noted that P and T represents projectile and target respectively.

S.No.	P	T	CN	$E_{c.m.}$	Temp.	ΔR (fm)		ℓ_{max}	$\sigma_{Expt.}$	σ_{DCM}(mb)		σ^{DCM}_{Total}
				(MeV)	(MeV)	ER	IMF	($\hbar$)	(mb)	ER	IMF	(mb)
Spherical Approach												
1	^{16}O	^{70}Ge	^{86}Zr	31.3	1.943	1.53	0.10	63	0.36	0.34	0.009	0.34
2	^{16}O	^{72}Ge	^{88}Zr	31.1	1.984	1.05	0.40	58	0.41	0.32	0.070	0.39
3	^{16}O	^{74}Ge	^{90}Zr	31.1	2.083	1.00	0.20	62	0.47	0.48	0.019	0.50
4	^{16}O	^{76}Ge	^{92}Zr	31.2	2.087	0.66	0.30	68	0.37	0.36	0.092	0.45
5	^{18}O	^{74}Ge	^{92}Zr	31.0	2.153	0.80	0.17	69	0.89	0.80	0.064	0.87
Deformed Approach												
1	^{16}O	^{70}Ge	^{86}Zr	31.3	1.943	1.70	0.80	55	0.36	0.36	0.007	0.36
2	^{16}O	^{72}Ge	^{88}Zr	31.1	1.984	2.00	0.93	65	0.41	0.20	0.070	0.41
3	^{16}O	^{74}Ge	^{90}Zr	31.1	2.083	2.00	0.88	67	0.47	0.43	0.020	0.47
4	^{16}O	^{76}Ge	^{92}Zr	31.2	2.087	1.27	0.60	70	0.37	0.36	0.005	0.36
5	^{18}O	^{74}Ge	^{92}Zr	31.0	2.153	1.2	0.63	64	0.89	0.88	0.011	0.89

component start appearing only at higher ℓ- values. It suggests that the centrifugal potential plays a significant role in deciding the dominant decay mode. This observation is persistent, independent of deformation effects, and hence prompt us to look for the IMF and fission component along with anticipated LP channel.

For both the choices of fragmentation (spherical and deformed), it is observed that the behavior of all isotopes is almost similar at minimum angular momentum whereas, the effect of iso-spin is much evident at maximum ℓ-value. For spherical choice, apart from the lightest isotope $^{86}Zr^*$, the magnitude of fragmentation potential follows a systematic trend and increases with addition of 2n, being minimum for light mass $^{88}Zr^*$ and maximum for heavy mass $^{92}Zr^*$ isotope. This anomalous behavior for $^{86}Zr^*$ isotope may be associated with relatively higher quadrupole deformation (β_2 $\sim$0.25) of ^{70}Ge target nucleus [12]. However, with inclusion of deformations a systematic trend in the potential energy surfaces (PES) is observed for all the Zr isotopes, showing increase in magnitude of potential with increase in iso-spin (N/Z) ratio. Although the difference in magnitude is very small except for the lighter Zr-isotope. It is worth noting that, this effect of iso-spin studied using DCM for Zr isotopes is similar to that observed for the heavy mass $^{250-258}$Fm* nuclei (for details see [6, 13, 14]). Since the decay of $^{88}Zr^*$ isotope is more favorable for spherical choice and is replaced by lightest isotope $^{86}Zr^*$ when quadrupole deformation is incorporated in the calculations, it may be concluded that systematics of Zr isotopes vary with the inclusion of β_2-deformation. Interestingly, with some deeper minima appearing in the intermediate mass fragments (IMF) region, change in structure is also observed with the inclusion of β_2-deformation, at extreme ℓ-values. Also, α-structure is more prominent for the deformed fragmentation and for lighter mass fragments. The above results are also supported from Fig.4.2 which shows variation of preformation probability P_0 as a function of fragment mass A_i (i=1,2). It is observed that on including β_2-deformation, the change in structure of Zr isotopes is observed which is more significant for the ER and IMF region. This suggests

Table 4.2: The LP, IMF and fission cross-sections for Zr isotopes, at highest energy $E_{c.m.}$=48 MeV, for spherical choice of nuclei (upper panel) and with inclusion of deformation (lower panel), compared with the experimental data of [1, 2]. Also shown are the best fit neck-length and angular momentum values.

P	T	CN	$E_{c.m.}$ (MeV)	Temp. (MeV)	ΔR (fm)		ℓ_{max} ($\hbar$)	σ_{DCM} (mb)			$\sigma^{Cal.}_{Total}$ (mb)	$\sigma^{Expt.}_{Fusion.}$ (mb)
					LP	IMF/ fission		LP	IMF	fission		
^{16}O	^{70}Ge	^{86}Zr*	48.5	2.370	2.00	1.18	58	756.0	103.0	3.36	862.0	863.0
^{16}O	^{72}Ge	^{88}Zr*	48.4	2.393	1.96	1.15	61	761.0	113.0	2.26	876.0	875.0
^{16}O	^{74}Ge	^{90}Zr*	48.4	2.471	1.84	1.05	65	749.0	69.5	1.22	819.0	821.0
^{16}O	^{76}Ge	^{92}Zr*	48.1	2.458	1.70	0.92	67	752.0	22.0	0.33	774.0	773.0
^{18}O	^{74}Ge	^{92}Zr*	49.0	2.536	1.81	0.82	68	840.0	11.4	0.09	851.4	847.9
^{16}O	^{70}Ge	^{86}Zr*	48.5	2.370	1.86	1.05	55	863.0	1.05	0.50	864.0	863.0
^{16}O	^{72}Ge	^{88}Zr*	48.4	2.393	2.00	1.16	65	769.0	83.0	25.0	878.0	875.0
^{16}O	^{74}Ge	^{90}Zr*	48.4	2.471	1.94	1.10	67	772.0	39.5	7.75	819.2	821.0
^{16}O	^{76}Ge	^{92}Zr*	48.1	2.458	1.75	0.94	70	767.0	12.1	1.36	780.0	773.0
^{18}O	^{74}Ge	^{92}Zr*	49.0	2.536	1.81	0.92	67	833.0	10.0	0.15	843.1	847.5

that role of deformations is more evident in the ER and IMF region whereas, no such effect is evident in the fission region. The fragment mass distribution at maximum angular momentum, $\ell = \ell_{max}$, is symmetric for all isotopes of Z=40 nucleus, for both spherical and deformed approach. Thus it may be concluded that in the decay of even mass Zr isotopes, the mass distribution in ER and IMF region gets influenced with the inclusion of deformation effects. In reference to the measured experimental fusion cross-sections, the decay cross-sections for Zr isotopes formed via ^{16}O+ ^{70,72,74,76}Ge reactions have been calculated by simultaneous fitting, using only parameter of the model, neck-length parameter (ΔR). In agreement with the experimental observations the DCM calculations also support the dominance of ER decay mode towards the total fusion cross-sections. At relatively smaller neck, very small contribution of IMFs is observed and symmetric fission component is found to be negligibly small. The ER and IMF cross-sections of $^{86-92}$Zr isotopes calculated using quadrupole static $\beta_{2i}(0)$ deformed choice of nuclei, are tabulated in Table 4.1

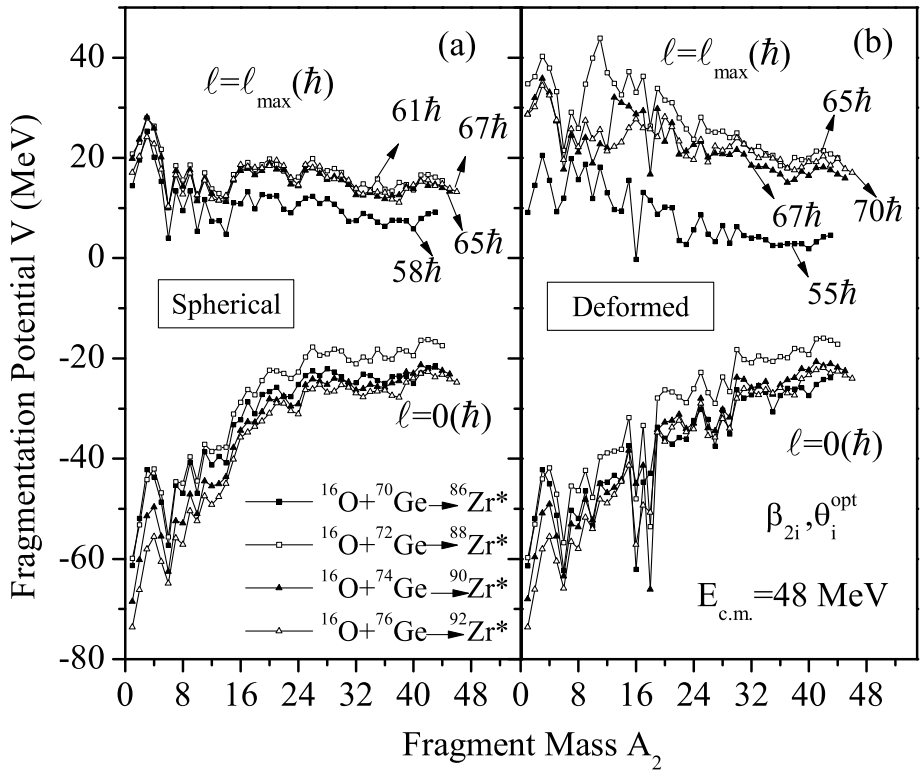

Figure 4.3: Same as Fig. 4.1 but at $E_{c.m.}$=48 MeV

(σ_{ff} is not shown as their contribution is negligibly small) and results are compared with the experimental fusion cross-section ($\sigma_{expt.}$). The corresponding ΔR and ℓ_{max} values are also listed in the Table. The different ΔR for the spherical and deformed approach shows the different time scales to which they occur, subject to the nature of dynamics of compound nucleus formed. The deformed choice requires large ΔR in comparison to spherical approach, indicating that decay for deformed nuclei occurs at an early stage and that with spherical choice evolve at relatively later instant.

Further, to see the effect of center of mass energy on decay structure of different isotopes of Zr, the comparison of fragmentation potential is plotted at $E_{c.m.}$=48.0 MeV. From Fig. 4.3(a), it is evident that, for spherical approach the structure of fragmentation potential is identical for all four Zr isotopes at extreme ℓ-values. Broadly speaking, the magnitude also appears to be overlapping except for $^{86}Zr^*$ nucleus, where it seems distinctly small at higher angular momentum. From these observations it may be concluded that, for spherical choice of fragmentation, the

decay of Zr isotopes is not influenced much by the change in iso-spin ratio. On the other hand, from the variation of fragmentation potential plotted in Fig. 4.3(b), it is noticed that, with inclusion of deformations the α- nucleus structure is pronounced and change in structure and magnitude of PES is observed for $^{86}Zr^*$ and $^{92}Zr^*$ system. This effect is more distinctly visible at higher ℓ-value. Thus it may be concluded that with inclusion of deformations the iso-spin effect becomes prominent in accordance with the result observed at lowest energy. The fragmentation behavior of different isotopes of Zr-systems gets modified thus changing the relative contribution of fragments as compared to spherical case. Conclusively, it may be said that, in reference to spherical approach, the fragmentation potential gets influenced with inclusion of deformations. It is worth noting in Fig. 4.3(b) that the fragmentation potential for chosen isotopes do not follow a systematic pattern. The heaviest two isotopes, i.e. $^{90,92}Zr^*$ are stable isotopes of Zirconium and the potential corresponding to them is in between the potential of nuclei lying on neutron deficient side of stability i.e. $^{86}Zr^*$ and $^{88}Zr^*$ isotopes. In terms of DCM calculations, lower fragmentation analogous to higher preformation probability, consequently results in relatively more favorable decay. Thus, the lightest isotope having minimum potential forms the most favorable decay isotope while the $^{88}Zr^*$ system having the maximum potential seems least favorable towards the decay process. This is further supported by larger half-life of $^{88}Zr^*$ isotope [15] as compared to other systems under consideration. One may remind here that, at lowest energy (see Fig. 4.1(b)), a systematic trend in the potential energy surface is observed for all the Zr isotopes, showing increase in magnitude of potential with increase in iso-spin (N/Z) ratio. This observation suggest that, the decay behavior of Zr-isotopes significantly affected by the center of mass energy of compound nucleus.

As deformations and related optimum orientations are found to play an important role in the dynamics of Zr nuclei, the further study is carried out for the use of quadrupole deformed approach only. The relative behavior of Zr isotopes and

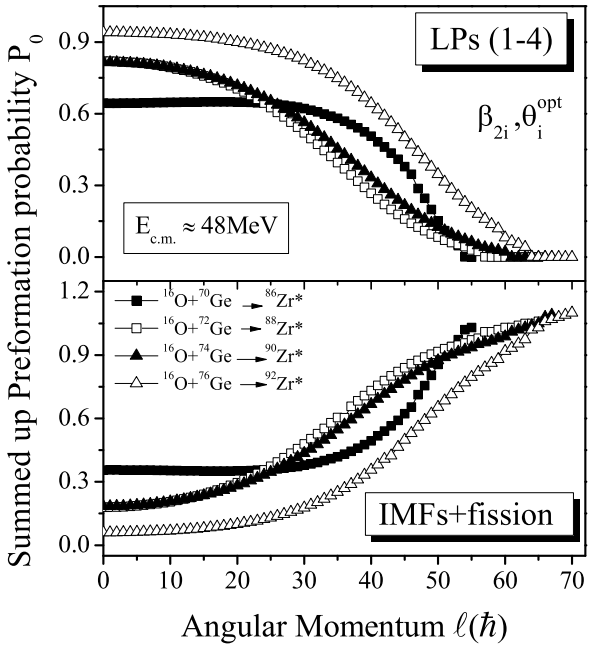

Figure 4.4: Summed up Preformation Probability P_0 as a function of Angular momentum $\ell(\hbar)$ at highest energy $E_{c.m.}$=48 MeV. Upper panel shows the P_0 for LPs and lower panel for IMF+fission.

characteristic behavior of LPs and IMFs+fission fragments is studied through the variation of summed up preformation probability P_0 plotted as a function of angular momentum ℓ as shown in Fig. 4.4 at center of mass energy of $E_{c.m.}$=48.0 MeV. The summed up P_0 represents the sum of preformation probability of all fragments corresponding to given angular momentum, ranging from ℓ=0$\hbar$ to ℓ_{max}. For the light particles (LPs), the preformation probability is summed up for fragments with mass, A_2 =1-4 (shown in upper panel of Fig. 4.4). On the other hand, for intermediate mass fragments + fission fragments it is summed up for fragments, A_2=5 to A_2=$A_{CN}/2$, where A_{CN} is mass of compound nucleus (shown in lower panel of Fig. 4.4). The summed up P_0 for complementary fragments form the mirror image and hence are not shown here. For all the Zr isotopes under study, the summed up P_0 for LPs is more at lower angular momentum and decreases with increase in ℓ-value. On the contrary IMF+fission contribution increases with increase in ℓ-value. This observation is consistent with the results stated in Fig. 4.3.

The characteristic behavior of the summed-up preformation probability (P_0) for

LPs and for IMF+fission fragments does not change significantly for a large range of angular momentum values. However, after a certain limit, a fine shift in the variation of P_0 can be seen. After ℓ=20$\hbar$, the LPs contribution starts decreasing at the cost of gain in IMF+fission component. For both LPs and IMF+fission fragments, the summed up preformation probability P_0 of different Zr isotopes start overlapping above $\sim$50$\hbar$. With decrease in ℓ-value, the summed up preformation probability of the lightest isotope (^{86}Zr*) and heaviest isotope of ^{92}Zr* can be identified separately. Thus from this variation it may be concluded that the angular momentum plays a crucial role in the dynamical evolution of Zr isotopes. Table 4.2 shows the results of DCM-calculated individual cross sections of LPs, IMFs and fission fragments at highest common center-of-mass energy ($E_{c.m.}$$\sim$48.0MeV) for all the Zr isotopes. The sum of the calculated cross-section $\sigma_{fusion}^{Cal.}$ and other relevant quantities are presented, together with the available measured experimental data ($\sigma_{fusion}^{Expt.}$), for the use of spherical approach and with inclusion of qaudrupole (β_{2i}) deformation. The results for ^{92}Zr* nucleus formed via ^{18}O induced reaction are discussed later in section 4.2.2. From the table it is observed that, for the decay of $^{86-92}$Zr* isotopes formed in the ^{16}O+^{70,72,74,76}Ge reaction the LPs form the dominant decay mode as compared to IMF/fission decay channel for both the spherical and deformed approach. This observation is in accordance with the experimental observation [1, 2]. On comparing the contribution of decay channels of different Zr isotopes, except for the lightest nuclei ^{86}Zr*, it is observed that with increase in mass and hence the iso-spin (N/Z) ratio of CN, the relative contribution of the IMF/fission fragments decreases gradually and finally turns out to be significantly small for the heaviest isotope ^{92}Zr* for which the LPs nearly saturate the measured fusion cross-sections. This observation remains consistent for the deformed approach also except for the fact that LP and IMF contribution is marginal for the lightest isotope of Zr. Moreover, it is observed that the neck-length parameter 'ΔR' decreases and the corresponding angular momentum increases for all for isotopes of Zr formed in ^{16}O

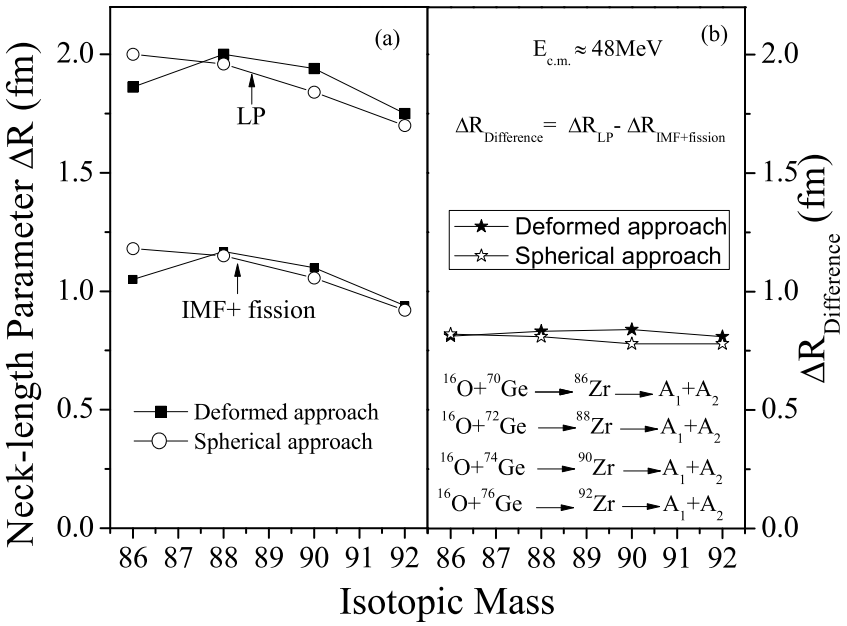

Figure 4.5: (a) Empirically fitted neck-length parameter ΔR and (b) difference of ΔR for LP and IMF+fission plotted as a function of isotopic mass of Zr isotopes for spherical and deformed approach.

induced reaction. The only exception is $^{86}Zr^*$ nucleus where ΔR is relatively small for deformed choice of fragmentation.

Fig. 4.5(a) illustrates the variation of neck-length parameter, ΔR as a function of isotopic mass for the use of spherical as well as quadrupole deformed approach. From the variation of simultaneously implied ΔR for best fit to DCM calculated LPs and IMF/fission cross-sections it is observed that for LP decay the neck-length parameter is higher as compared to that for IMF/fission decay channel. This observation is independent of the consideration of deformation effects and is in agrement with [6–8]. The different ΔRs for the two processes, LPs and IMF/fission suggest that they occur in different time scales, subject to the nature of dynamics of compound nucleus formed. As depicted in Fig. 4.5(a), the LPs require large ΔR in comparison to IMF/fission, indicating that LP emission occurs at early stage and IMF/fission process evolve at relatively later extent. Fig. 4.5(b) shows the ΔR_{diff}(=ΔR_{LP} - $\Delta R_{IMF+fission}$) as a function of isotopic mass. This difference is

remains almost constant ($\sim$ 0.8 fm), for the different decay paths of various Zr-isotopes. One may observe that even for constant ΔR_{diff}, the iso-spin ratio of CN influences the appropriate neck formation and hence the decay time of a given CN. The total cross-section ($\sigma_{fusion}^{Cal.}$) of DCM calculated within one parameter fitting ΔR, for all the four cases at highest center-of-mass energy, is found to have a nice agreement with the available experimental data [1, 2].

4.2.2 Role of incoming channel in the decay of ^{92}Zr and ^{76}Kr compound nuclei

It is generally believed that the formation and decay of CN are two independent processes. Besides for the requirement of various conservation laws, it can be disintegrated in various ways depending on the mass of target-projectile combination, deformation of colliding nuclei and energy involved. However, as an exception to Bohr independence hypothesis, there may be a possibility that the decay channel retains the memory of colliding partners. Thus, after studying the role of iso-spin on the dynamics of even mass Zr isotopes, we further aim to investigate the role of entrance channel on the decay of heaviest Zr isotope formed via ^{16}O+^{76}Ge$\rightarrow^{92}$Zr* and ^{18}O+^{74}Ge$\rightarrow^{92}$Zr* channels in reference to data of [1].

The preformation probability P_0 is plotted as a function of fragment mass A_2 in Fig. 4.6(a). Despite having different ℓ_{max} values for both the channels, the fragmentation potential remains almost identical in the fissioning region. Some variations are observed in IMF/HMF (heavy mass fragments) region but the contribution of these decay paths is much lower than the dominant LP component. Therefore, one may assume that fragmentation behavior is not influenced much while changing ^{16}O beam with ^{18}O in the way of formation of ^{92}Zr* nucleus. Further, by carrying out a comparative study of summed up preformation probability of both the channels in Fig. 4.6(b) it is observed that although the characteristic behavior of LPs and IMF+fission fragments is different at lower versus higher ℓ-values, the variation of

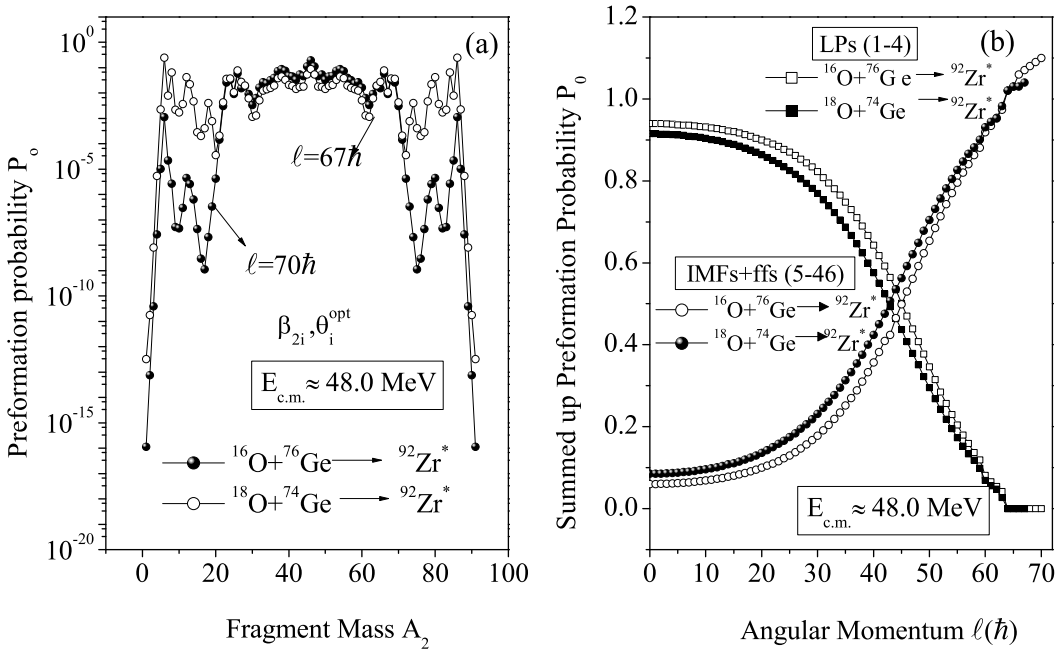

Figure 4.6: (a) Preformation Probability P_0 as a function of fragment mass A_2 for the decay of ^{92}Zr* formed via two incoming channels ^{16}O+^{76}Ge and ^{18}O+^{74}Ge at ℓ=$\ell_{max}(\hbar)$ for deformed choice of nuclei (b) Summed up Preformation Probability P_0 as a function of angular momentum $\ell(\hbar)$ for LPs and IMF+fission fragments.

P_0 is almost identical for both the reactions. Although, difference in magnitude of P_0 is observed being relatively smaller for ^{18}O induced reaction (ℓ_{max}=67$\hbar$) as compared to that for ^{16}O induced reaction (ℓ_{max}=70$\hbar$). The light particle contribution to the summed-up P_0 is maximum at lower ℓ-value, whereas the same gets reduced at higher angular momentum and vice versa for IMFs+fission fragments for both the reaction channels. It is also observed that LPs and IMFs+fission fragments share almost same $P_0\simeq$0.5 at a particular angular momentum, *i.e.* at $\sim$45$\hbar$ and 50$\hbar$ for ^{18}O and ^{16}O induced reactions respectively.

To investigate further, we have plotted the barrier-lowering parameter [16] at different ℓ's for the decay of ^{92}Zr* nucleus, formed in the above mentioned reaction channels and is shown in Fig. 4.7. The variation of ΔV_B is almost similar for both the reaction channels. Independent of choice of entrance channel, the magnitude of ΔV_B is minimum at higher angular momentum and increases as the angular momentum decreases. Further, ΔV_B is lowest for LPs as compared to IMF+fission

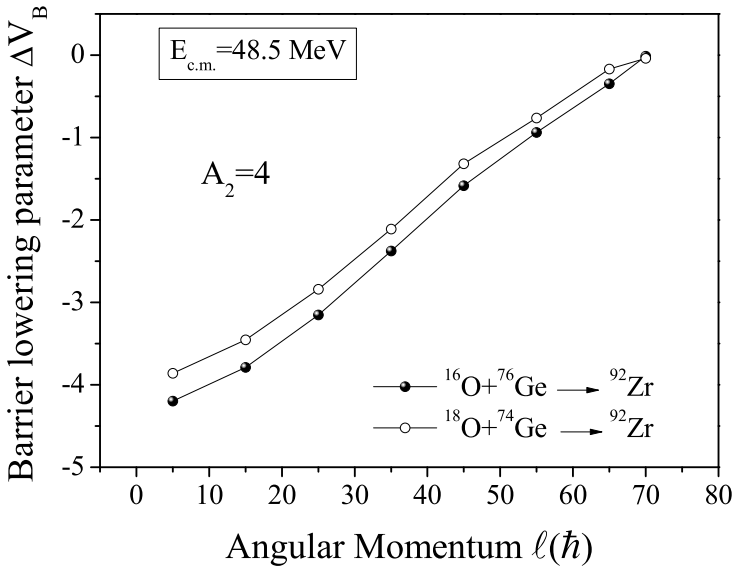

Figure 4.7: Barrier lowering parameter ΔV_B as a function of angular momentum ℓ for the decay of ^{92}Zr* nuclei formed in ^{16}O+^{76}Ge and ^{18}O+^{74}Ge reactions.

fragments (not shown here) which indicates that relatively lesser barrier modification is needed for LPs as compared to IMF+fission decay for both the entrance channels. In other words, the behavior of barrier lowering parameter is almost similar for both reactions. Concludingly, the observations drawn from Fig. 4.6 and Fig. 4.7 indicate that the decay of ^{92}Zr* nucleus is almost independent of the choice of entrance channel.

So far the role of incoming channel has been studied in ^{92}Zr* nucleus formed in ^{16}O and ^{18}O induced reactions. As a next step, an attempt is made to check the consistency of above results in reference to much lighter mass ^{76}Kr* nucleus, which is also formed via reactions involving same projectiles. Interestingly, both these reactions form an ideal case to explore the effect of entrance channel in reactions involving ^{16,18}O projectiles. Apparently, both ^{16}O+^{60}Ni and ^{18}O+^{58}Ni reactions studied here involve spherical magic projectile and target nucleus, giving rise to deformed magic CN and thus form a subject of great interest. In framework of DCM, the decay of deformed magic ^{76}Kr* nucleus is studied in form of LP emission in reference to the available experimental data [10]. The calculations have been made at two comparable center-of-mass energies, $E_{c.m.}$∼31 MeV and $E_{c.m.}$∼48 MeV. Fig. 4.8 (a) and (b)

illustrate the fragmentation potentials V (MeV) for the decay of the parent nucleus ^{76}Kr* at $E_{c.m.}$∼31 and 48 MeV at corresponding extreme ℓ values, ℓ_{max}= 41$\hbar$ and ℓ_{max}= 42$\hbar$ respectively. From the figure it is observed that the structure of fragmentation potential is almost similar for both the reactions. An increase in magnitude of PES is observed while going from ^{16}O to ^{18}O induced reaction. The fragmentation potential for both the reactions is higher in magnitude at $E_{c.m.}$∼48 MeV as compared to $E_{c.m.}$∼31MeV. Based on the fragmentation potential in Fig. 4.8 (a) and (b), the preformation probability P_0 is plotted in Fig. 4.8 (c) and (d) as a function of light mass fragment A_2 for both the reaction channels. It is relevant to mention here that, in framework of DCM, cross sections follow the trend of preformation probability P_0, which means that structure effects are addressed via preformation probability of decaying fragments. Figs. 4.8 (c) and (d) show that no much change on structure is evident for both the reactions at extreme energies. Interestingly, despite of difference in fragmentation potential for two channels, the variation of P_0 for both reaction starts overlapping particularly at higher incident energies. Only a small difference in structure for IMF/HMF region is observed at lowest energy which may be neglected as the LPs form the dominant decay mode for ^{76}Kr* nucleus. All these results indicate that no significant signature of entrance channel is observed in the decay of ^{76}Kr* nucleus as well. The DCM calculated σ_{LP} for ^{76}Kr* system show a nice agreement with the experimental data. An explicit representation of the results obtained from these calculations (for β_2 deformation) is given in Table 4.3, where the calculated LP cross sections at both energies for ^{16}O+^{60}Ni and ^{18}O+^{58}Ni reactions are presented along with corresponding neck length values and the experimental data [10].

4.2.3 Effect of projectile mass in the decay of Sn* nuclei

In this chapter, a description of various nuclei formed in ^{16,18}O reactions has been presented by focussing on various features such as deformation and orientation ef-

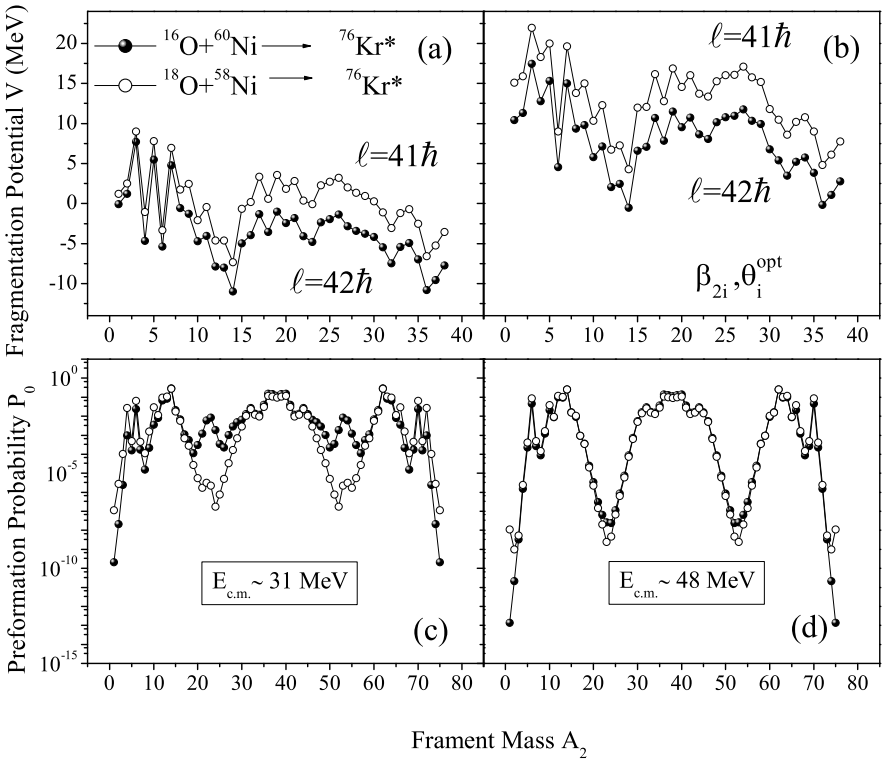

Figure 4.8: Fragmentation potential (a, b panel) and Preformation Probability P_0 (c, d panel), plotted as a function of fragment mass A_2 for ^{16}O+^{60}Ni→^{76}Kr*, ^{18}O+^{58}Ni→^{76}Kr* reactions at extreme center of mass energies i.e. $E_{c.m.}$=31 MeV and 48 MeV.

Table 4.3: The LPs cross-sections for ^{76}Kr* and ^{108,110}Sn* systems, calculated using DCM, at extreme $E_{c.m.}$'s for different entrance channel compared with respective experimental data [10, 11].

Projectile	Target	CN	$E_{c.m.}$ (MeV)	Temp. (MeV)	ΔR (fm) LP	$\ell_{max}(\hbar)$	σ_{LP}^{DCM}(mb)	$\sigma_{Expt.}$(mb)
^{16}O	^{60}Ni	^{76}Kr*	31.6	1.988	1.350	41	22.9	23
^{16}O	^{60}Ni	^{76}Kr*	47.4	2.424	1.863	42	665	668
^{18}O	^{58}Ni	^{76}Kr*	31.2	2.214	1.419	41	54.6	55
^{18}O	^{58}Ni	^{76}Kr*	48.8	2.653	1.938	42	789	789
^{16}O	^{92}Mo	^{108}Sn*	42.6	1.704	1.06	73	2.50	2.56
^{16}O	^{92}Mo	^{108}Sn*	48.9	1.856	1.42	74	136	133
^{18}O	^{92}Mo	^{110}Sn*	42.0	1.856	0.994	77	1.96	1.96
^{18}O	^{92}Mo	^{110}Sn*	48.7	2.00	1.337	78	95.3	95

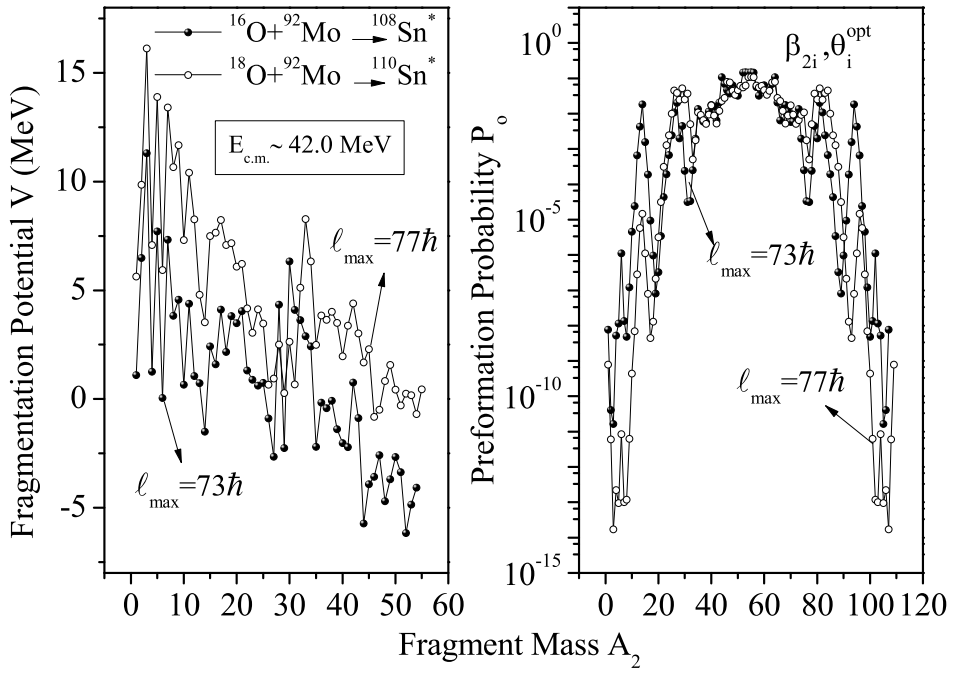

Figure 4.9: Variation of (a) Fragmentation Potential V (MeV) (b) Preformation Probability P_0 for the decay of ^{108,110}Sn* as a function of fragment mass A_2 at lowest energy i.e. $E_{c.m.}$~31 MeV.

fects, role of iso-spin (N/Z ratio) and mass of CN formed besides exploring the effect of incoming channel, by studying the decay of CN formed through different projectile and target combinations. Further, in order to have a comprehensive picture of this analysis, we have also made an attempt to study the role of above mentioned projectiles in the reactions involving same target nucleus. With this interest the decay of proton magic ^{108,110}Sn* nuclei formed via ^{16,18}O+^{92}Mo reactions is studied. In framework of DCM the calculations for the decay of ^{108,110}Sn* nuclei studied in form of LP emission have been done in reference to the experimental data of [11]. Fig. 4.9 shows the the fragmentation potential as a function of light fragment mass A_2 and preformation probability P_0 as a function of fragment mass A_i, i = 1, 2, for the decay of ^{108,110}Sn* nuclei, calculated for ℓ_{max}=73ħ and ℓ_{max}=77ħ corresponding to ^{16}O+^{92}Mo and ^{18}O+^{92}Mo reactions, at $E_{c.m.}$~42 MeV and with the inclusion of quadrupole deformation.

It is observed that, except for the difference in structure of PESs for IMF/HMF region, the fragmentation potential is almost identical with the presence of α- nucleus

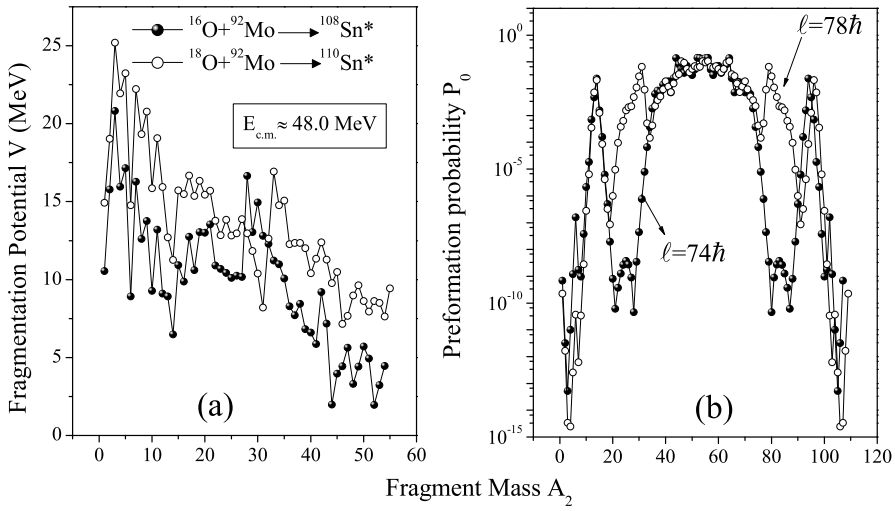

Figure 4.10: Same as Fig. 4.9 but plotted at highest energy i.e. $E_{c.m.}\sim$ 48 MeV.

structure in both the channels. Moreover, the variation of preformation probability illustrates near symmetric mass distribution for both the reactions, with a very small difference observed in IMF/HMF region. The results are consistent with those obtained at relatively higher incident energy ($\sim$ 48 MeV) as depicted in Fig. 4.10. These observations give us an idea that the decay of ^{108,110}Sn* isotopes is independent of mass of projectile involved and does not effect the decay process of ^{108,110}Sn* nuclei.

Finally, Fig. 4.11 (a) and (b) presents a comparative description of all the three systems formed in ^{16}O induced and ^{18}O induced reactions respectively in form of summed up preformation probability P_0 as a function of angular momentum ℓ upto ℓ_{max}. From Fig. 4.11 (a) it is observed that a systematic trend in variation of P_0 is observed for the ^{76}Kr*,^{92}Zr* and ^{108}Sn* nuclei. At lower ℓ-values, the aggregated preformation factor is higher and almost same for three nuclei. After certain ℓ-value, which is lowest for lighter nuclei ^{76}Kr* and increases from 37$\hbar$ to 52$\hbar$ with increase in mass of CN from ^{92}Zr* to ^{108}Sn, the preformation factor adopt a downwards trend with increase in ℓ-values. In Fig. 4.11 (b), the results are plotted for ^{76}Kr*,^{92}Zr* and ^{110}Sn* nuclei formed via ^{18}O channel. It is observed that the general trend of P$_o$ for all three systems is similar to that observed for ^{16}O induced reaction.

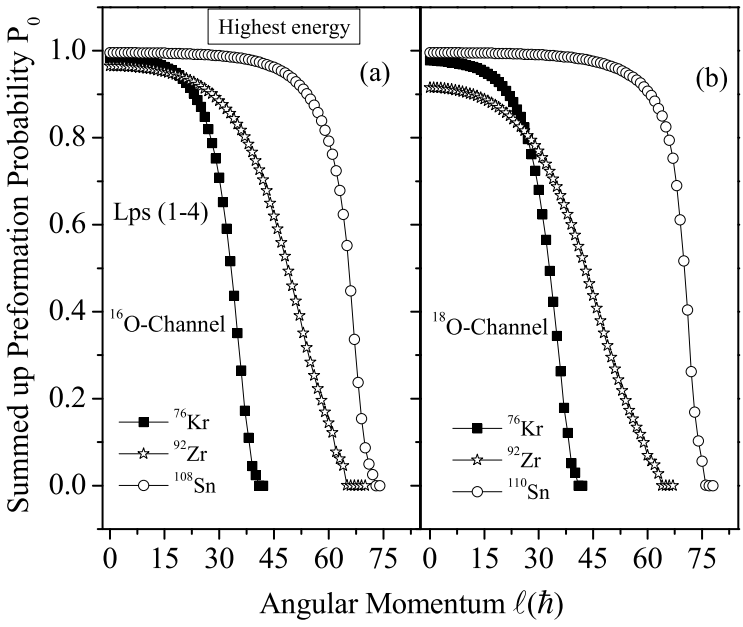

Figure 4.11: Summed up Preformation Probability P_0 plotted as a function of angular momentum ℓ for ^{16}O and ^{18}O induced reactions.

4.3 Conclusions

In this chapter, we have studied the decay process of different compound systems formed via ^{16,18}O induced reactions. DCM is used to investigate isotopic dependance, entrance channel effects and role of projectile mass by using spherical and deformed choices of fragmentation. The theoretically calculated decay cross-sections find nice agreement with experimental data. The deformations and orientation effects are shown to play significant role in the isotopic analysis of Zr systems. Moreover the entrance channel independence is examined for heaviest ^{92}Zr* isotope formed through ^{16,18}O induced reactions and this result seems consistent with decay pattern of ^{76}Kr* system formed with same projectiles. Beside this, effect of target mass in the decay mechanism of deformed magic ^{108,110}Sn* systems is also worked out. The present set of calculations provide a comprehensive description of decay patterns observed in ^{16,18}O induced reactions and inturn provide useful insight regarding the dynamics of light mass nuclei.

It may be noted that the rotational energy component for the calculations per-

formed in chapters 3 and 4, is estimated using sticking choice of moment of inertia. In the subsequent chapter, an attempt is made to explore the relative effect of sticking verses non-sticking choice of interaction in view of dynamical evolution of nuclei formed in heavy ion induced reactions.

Bibliography

[1] H. M. Jia, C. J. Lin, F. Yang, X. X. Xu, H. Q. Zhang, Z. H. Liu, L. Yang, S.T. Zhang, P. F. Bao, and L. J. Sun, Phys. Rev. C **86**, 044621 (2012).

[2] E. F. Aguilera, J.J. Kolata, and R. J. Tighe, Phys. Rev. C **52**, 6 (1995).

[3] R. K. Gupta, M. Balasubramaniam, R. Kumar, D. Singh, C. Beck, Nucl. Phys. A **738**, 479c (2004).

[4] M. Kaur, and M. K. Sharma, Eur. Phys. J. A **50**, 61 (2014).

[5] Rajni, R. Kumar and M. K. Sharma, Phys. Rev. C **90**, 044604 (2014).

[6] G. Sawhney, G. Kaur, M. K. Sharma, and R. K. Gupta, Phys. Rev. C **88**, 034603 (2013).

[7] G. Kaur and M. K. Sharma, Phys. Rev. C **87**, 044601 (2013).

[8] G. Kaur, D. Jain, R. Kumar, and M. K. Sharma, Nucl. Phys. A **916**, 260 (2013) .

[9] R. K. Gupta, M. Balasubramanium, R. Kumar, N. Singh, M. Manhas, and W. Greiner, J. Phys. G: Nucl. Part. Phys. **31**, 631 (2005).

[10] A. M. Borges, C. P. da Silva, D. Pereira, L. C. Chamon, E. S. Rossi, Jr. and, C. E. aguiar, Phys. Rev. C **46**, 6 (1992).

[11] M. Benjelloun, W. Galster and, J. Vervier, Nucl. Phys. A **560**, 715-732 (1993).

[12] Hamilton J H *et al.*, J. Phys. G: Nucl. Part. Phys. **10**, L87-L91 (1984).

[13] M. Kaur, M. K. Sharma and R. K. Gupta, Phys. Rev. C **86**, 064610 (2012).

[14] G. Kaur and M. K. Sharma, Nucl. Phys. A **884**, 36 (2012).

[15] E. K. Hyde and G. D. O'Kelley, Phys. Rev. **82**, 6 (1951).

[16] S. K. Arun, R. Kumar and R. K. Gupta, J. Phys. G:Nucl. Part. Phys. **36**, 085105 (2009).

Chapter 5

Role of sticking vs non-sticking limits of moment of inertia in the dynamics of Rn compound system

In previous chapter, the dynamical effects of light mass nuclei were explored in view of N/Z ratio, excitation energy, deformation and orientation etc. Here in this chapter, the role of rotational energy is tested in the dynamics of two isotopes of Rn compound nucleus *i.e.* ^{214}Rn* and ^{216}Rn* nuclei using the sticking ($I_{\rm S}$) and the non-sticking ($I_{\rm NS}$) limits of moment of inertia. Beside this, the nuclear deformation effects i.e. quadrupole β_2 (static and dynamic) and higher order static deformation up to β_4 are duly incorporated. In previous chapters, the deformation effects were included upto β_2 only. Furthermore, the influence of increase in energy and neutron number is analyzed in reference to ER survival probability of Rn compound nucleus.

5.1 Introduction

The study of fusion-fission dynamics in heavy-ion-induced reactions remain a subject of vigorous research during last few decades. The time evolution of the composite system and the parameters on which the dynamics depends are still not fully under-

stood. Perhaps, a organized study of these reactions can divulge information about the complex dynamics engrossed in the process. Evaporation residues (ERs) are considered as signature of compound nucleus (CN) formation, and substantial attempts are devoted to address dynamical behavior of light, heavy and superheavy nuclei. The production of superheavy elements are determined by the capture probability of the projectile-target systems inside the interaction barrier, with a probability of forming a fully equilibrated CN and finally the survival probability of this heavy nucleus is examined against the fission decay. Evaporation residue is the heavy residual nucleus that survives the fission and its existence crucially rely on the competition between fission, heavy fragment emission and γ evaporation channels of CN. As a consequence, the ER channel serves as a sensitive probe to investigate the fission dynamics particularly in pre-saddle region [1–3].

The ER cross-sections have been measured for a number of compound nuclei in mass region ≥ 200, where fission forms an important decay channel. Recently, an experiment [4] was performed at 15 UD Pelletron accelerator facility of the IUAC, in order to measure the evaporation residue cross-sections of ^{16,18}O+^{198}Pt reactions forming ^{214,216}Rn* compound systems over a wide range of center of mass energies. In order to measure the fission excitation functions of ^{16,18}O+^{198}Pt reactions, GPSC experiment [5] was conducted at a beam energy range of 85-107 MeV.

The fusion evaporation and fusion-fission (ff) processes are affected by the excitation energy of projectile (or corresponding temperature), total angular momentum and associated moment of inertia etc. Considering this, present work involves the study of ER and ff processes where angular momentum effects are explored via two approaches of moment of inertia called as sticking I_S and non-sticking I_{NS} limits [6, 7]. In I_S limit of moment of inertia (MOI), Cindro and Picanic [6] considered the rotation of two touching spheres about their common center of mass, which for two separated spheres gives the "non-sticking" I_{NS} limit of moment of inertia. In the present work, the dynamical cluster decay model (DCM) [8–10] is employed to

address ER and ff cross-sections of ^{214,216}Rn* compound nuclei. In DCM based calculations, the decay cross-sections are mostly estimated within MOI in I_S limit due to the use of proximity potential of Blocki *et al.* [11], which otherwise for fission fragment anisotropy [12], favors I_{NS} limit where intrinsic rotation is absent owing to the small separation distance between fragments. Beside the role of moment of inertia, the effect of multipole deformation is also tested in the decay of ^{214,216}Rn* compound nuclei. The calculations are done by considering the fragments to be spherical, static and dynamic quadrupole deformed (β_2) with optimum orientations [13] and static hexadecapole deformed (β_4(T=0)) with compact orientations [14]. The ground state deformations are taken from the work of [15]. It is to be noted here that, the static deformation finds its origin in the shell effects. At higher energies, the shell effects disappear and the deformation effects get minimized reaches towards zero. In that case, the deformation parameter changes with temperature and the same effect may be included by employing dynamic deformations as suggested in [16]. In this chapter, a comparative analysis of I_S and I_{NS} limit of moment of inertia is worked out in terms of barrier characteristics, preformation probability and barrier lowering effects along with role of deformation and orientation of decaying fragments. It is observed that, for both the compound nuclei, the barrier height is greater (barrier position is lower) for I_{NS} limit as compare to moment of inertia in sticking limit. Moreover, the highest barrier height is obtained with static quadrupole deformation and lowest for static hexadecapole deformation, while spherical and dynamics cases operate between the two. The effect of moment of inertia (MOI) and deformations is further apparent from the preformation probability of decaying fragments as fission window changes significantly for the use of different approaches.

The authors of ^{214,216}Rn* [4, 5] have also performed two independent theoretical calculations in order to address ER and fission data. Under statistical model, Kramers's fission width is used as free parameter to fit the experimentally extracted ER data, however PACE2 code is employed to address fission data. DCM has the

advantage to treat both the decay processes *i.e.*, ER and fission fragments on equal footing. The reason behind choosing above mentioned reactions is that, the experimental data for ER and ff cross-sections are available in same center of mass energy range, which on earlier occasions was accounted individually either for evaporation or ff channels [10, 17–20] within I_S or I_{NS} limit of MOI. In DCM, the experimental data is addressed by optimizing the neck-length ΔR, and the calculated ER shows good comparison with available data for I_S approach for all considered choices of deformations, except for ff data at highest energy, which could be addressed only after the inclusion of higher order static deformations (upto $\beta_4(0)$). On the other hand I_{NS} limit seems suitable only for ER channel. Beside this, the effect of increase in energy and neutron number on the survival probability of Rn system is estimated in view of sticking limit of interaction.

The purpose of this work is three fold (i) to analyze the effect of sticking vs non-sticking moment of inertia in context of ER and ff processes. (ii) to see the role of quadrupole and hexadecapole deformations and corresponding orientations degree of freedom. (iii) to address the survival probability of ^{214,216}Rn* nuclei against fission. The chapter is organized as follows. The Calculations and results are described in Section 5.2 and the results are summarized in Section 5.3.

5.2 Calculations and Results

The feasibility of moment of inertia (MOI) in sticking and/or non-sticking limit is tested for ER and ff paths in terms of barrier characteristics, preformation probability and barrier lowering effects etc. The role of static and dynamic deformation upto β_2 and higher multipole static deformations upto β_4 are worked out for better understanding of dynamical paths governed in view of ^{16,18}O+^{198}Pt reactions. Moreover, ER survival probability of ^{16,18}O+^{198}Pt channels against fission is also estimated. Finally, the ff cross-sections for both the channels are predicted, wherever experimental data is not available.

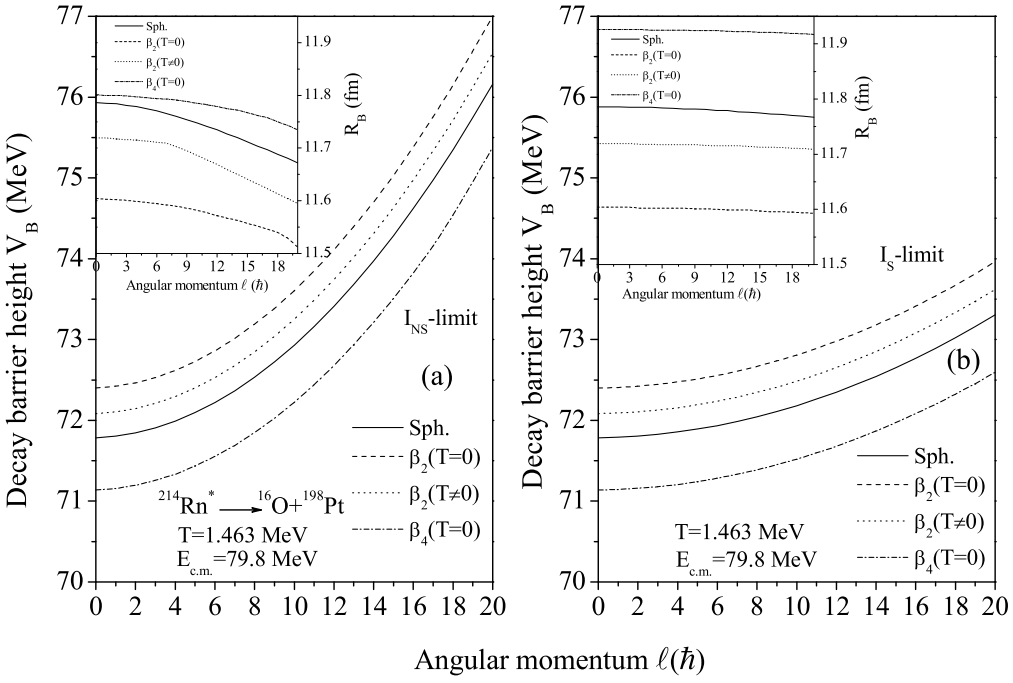

Figure 5.1: The decay barrier height V_B and barrier position R_B (shown in inset) of $^{214}Rn^*$ compound nucleus plotted as a function of angular momentum ℓ calculated with (a) non-sticking limit I_{NS} and (b) sticking limit I_S of moment of inertia including spherical, static and dynamics β_2 deformations and static higher order β_4 deformation of nuclei.

5.2.1 Effect of sticking and non-sticking interactions on barrier characterstics

We first probe the relative role of different limits of moment of inertia 'I' i.e. sticking (I_S) and non-sticking (I_{NS}) limits in the total interaction potential. For the purpose, we have plotted the decay barrier heights V_B and barrier positions R_B as a function of angular momentum (ℓ) using both the choices of moment of inertia as illustrated respectively in Fig. 5.1(a) and (b). The variation is shown at fixed center of mass energy $E_{c.m.}$ =79.8 MeV for the decay of CN $^{214}Rn^* \rightarrow {}^{16}O+{}^{198}Pt$. The calculations are made for spherical, static and dynamic quadrupole and static hexadecapole choices of deformations. The ℓ_{max} for I_{NS} choice is $20\hbar$ so the variation of V_B and R_B is plotted in the range ℓ=$0\hbar$ to $20\hbar$, for both the cases. One may notice from Fig. 5.1 that, (i) V_B increases and R_B decreases (shown in inset of Fig. 5.1(a) and (b)) with increase in angular momentum for both non-sticking as well as sticking limits

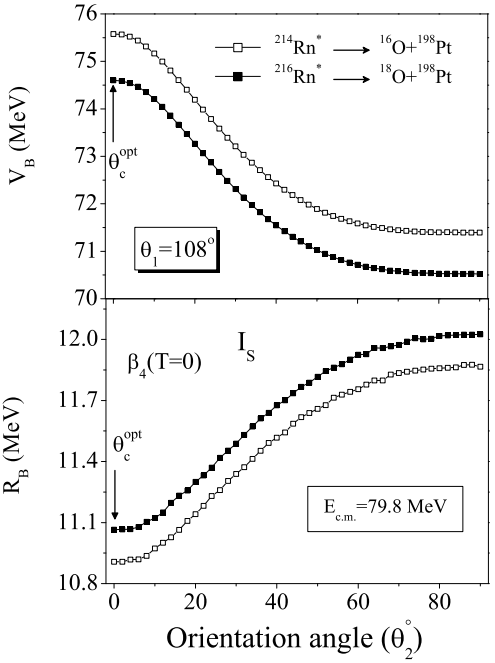

Figure 5.2: Upper panel shows the decay barrier height V_B and lower panel shows the decay barrier position R_B plotted as a function of orientation angle θ for $^{214,216}Rn^{*} \rightarrow {}^{16,18}O+{}^{198}Pt$ with sticking limit of moment of inertia. Deformations are included upto β_4.

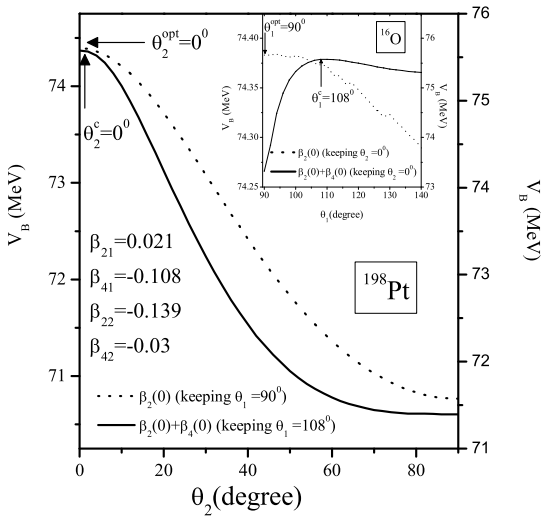

Figure 5.3: Barrier height V_B as a function of orientation angle θ plotted for both quadrupole (scale on left side) and hexadecapole (scale on right side) deformations for ^{198}Pt and ^{16}O (shown in inset) nuclei. θ_1 and θ_2 respectively corresponds to angles of ^{16}O and ^{198}Pt nuclei and β_{2i} and β_{4i} (i=1,2) corresponds to quadrupole and hexadecapole deformation of ^{16}O and ^{198}Pt nuclei.

irrespective of deformation degree of freedom (ii) the increase in barrier height is much steeper for I_{NS} choice as compared to that for I_S (iii) the barrier position within I_{NS} limit shifted more rapidly towards the lower interaction radius in comparison to I_S (iv) the barrier height as well as barrier position gets modified, depending upon the choice of deformation, since lowest barrier height and corresponding highest barrier position is observed for higher order deformation and vice-versa for $\beta_2(0)$ choice of nuclei, with spherical case operating in between the two.

To investigate further, the effect of sticking I_S and non-sticking I_{NS} limits of moment of inertia is studied in view of orientation degree of freedom. Here, the orientation angle for quadrupole deformations are optimized with respect to its signs ($\pm$, zero) [13]. The optimized orientations help to decide the most compact (or elongated) configuration during the formation of compound nucleus via equatorial (or

polar) collision. However, when higher order deformations are taken into account, the optimized orientation criteria do not work i.e. while taking hexadecapole deformation (β_4), the most compact configuration is obtained by fixing the orientation angle for smallest interaction radius R_B and equivalently for the highest interaction barrier V_B for hot orientation approach. In view of this, Fig. 5.2 is plotted, showing the barrier characteristics (i.e. barrier height and barrier position) as a function of orientation angle estimated using hexadecapole deformation, for the decay of Rn nuclei via projectile like fragments ($^{214}Rn^{*}\rightarrow^{16}O+^{198}Pt$, $^{216}Rn^{*}\rightarrow^{18}O+^{198}Pt$).

It is anticipated from the Fig. 5.2 that, for both $^{214}Rn^{*}$ and $^{216}Rn^{*}$ systems, the barrier is highest and most compact at (108^{o},0^{o}) referred as not-belly to belly compact (nbbc) configuration [14]. For further detail, we have plotted Fig. 5.3, showing the individual variation of barrier height for ^{198}Pt and ^{16}O (shown in inset) nuclei as a function of orientation angle θ including both quadrupole β_2 and hexadecapole β_4 deformations. The β_{2i} and β_{4i} (i=1,2) of both nuclei are shown in figure, taken from the work of Moller and Nix [15]. Firstly, we have fixed the angle of one nucleus and varied the other. Here in Fig. 5.3, we have varied the angle of ^{198}Pt (θ_2) and angle corresponding to ^{16}O (θ_1) is fixed. It is observed that, by taking β_2-deformation only, the highest barrier is obtained at θ_2=0^0 (θ_1=90^0) referred as optimum configuration and on adding hexadecapole deformation β_2+β_4, the largest barrier height remain at 0^0 (θ_1=108^0) but corresponds to compact configuration [14]. This means that the deviation in configuration from optimum to compact is due to the influence of large hexadecapole deformation of ^{16}O (β_{21}=0.021, β_{41}=-0.108), whereas deformation of ^{198}Pt seems to play a silent role. In conclusion we found that, on considering quadrupole deformation, the optimum angle is obtained at (90^0,0^0), whereas the same gets shifted to (108^0,0^0), after inclusion of β_4-effect. Same results are obtained for the decay of $^{216}Rn^{*}\rightarrow^{18}O+^{198}Pt$ nucleus. It is important to mention here that, the compactness of nuclei is independent of the choice of the moment of inertia i.e. the same nbbc configuration is observed if we opt for sticking or non-sticking limit

of the moment of inertia. Since the decay barrier height is significantly influenced by the choice of deformations and related orientations of nuclei. Hence, a study comprising of such effects may impart useful information regarding the dynamical behavior of chosen reactions.

5.2.2 Role of moment of inertia and deformations on structure and decay cross-sections of ^{214,216}Rn* compound nuclei

The effect of moment of inertia (I_{NS} and I_S) and deformation is further evident from the Fig. 5.4, which shows the preformation probability P_0 for the decay of ^{214,216}Rn* compound nuclei plotted as a function of fragments mass A_2. Fig. 5.4(a) represents the mass distribution of ^{214}Rn* CN at $E_{c.m.}$=79.8 MeV for spherical, static $\beta_2(0)$, dynamic β_2(T) as well as static higher order deformation $\beta_4(0)$. It is clearly observed from Fig. 5.4(a) that, for ^{214}Rn* compound nucleus, on using I_{NS} limit of moment of inertia, asymmetric fission peaks appear along with some contribution from symmetric window for spherical and β_2(T) choice of nuclei, however for $\beta_2(0)$ and $\beta_4(0)$ deformations, the contribution of symmetric region significantly suppressed. On the other hand, within I_S limit, for spherical choice, the symmetric fission fragments start contributing within mass range A_2=77-107 (and corresponding complementary fragments), whereas, mass yield distribution remain clearly asymmetric for β_2-static, -dynamic and higher order deformations with mass range A_2=74-94, A_2=71-97/103-107 and A_2=69-95 (and corresponding complementary fragments) respectively as shown in Fig. 5.4(b). It may be noted that, the magnitude of both symmetric and asymmetric peaks is much higher in I_S case as comparison to that for I_{NS} approach. It suggest that, the choice of moment of inertia and deformations influence the contribution of fission fragments significantly.

Now to see the impact of moment of inertia on another isotope of Rn i.e. ^{216}Rn*, Fig. 5.4(c) and (d) are plotted. The comparison is made at common lowest center

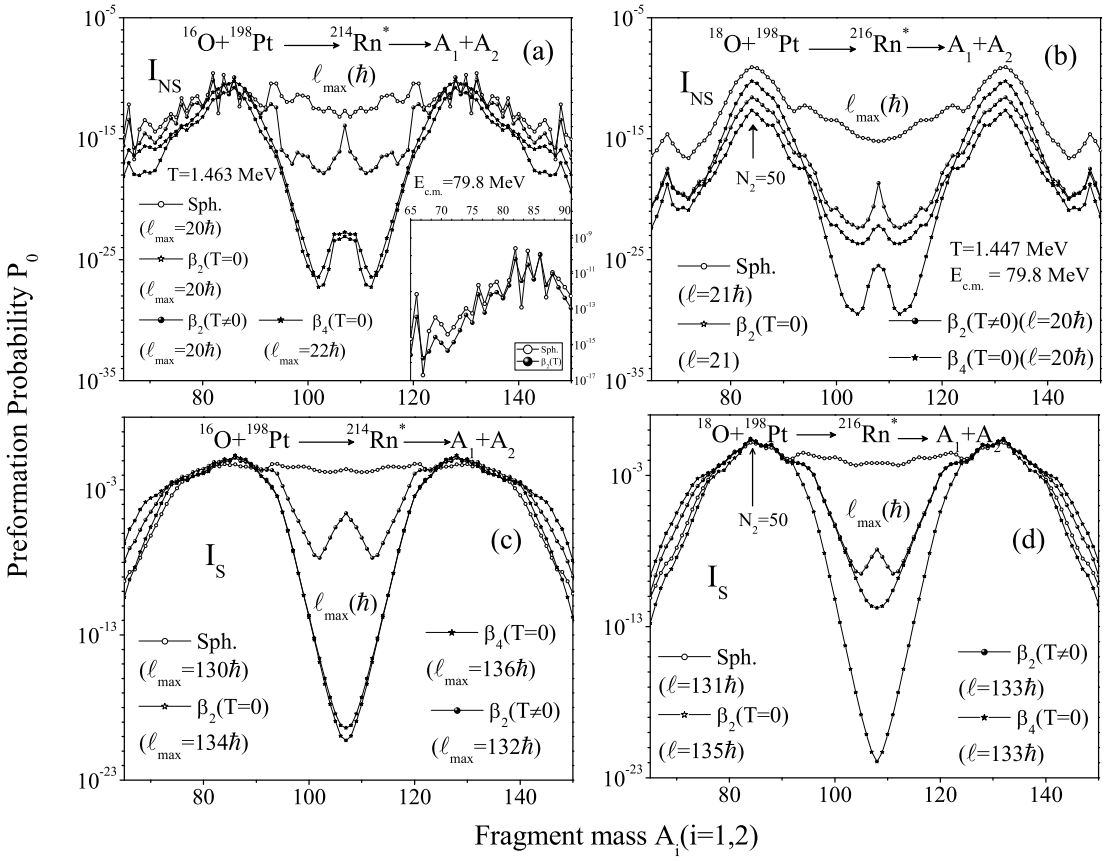

Figure 5.4: Preformation probability P_0 as a function of fragments mass A_2 plotted using both limits of moment of inertia (a),(c) for ^{16}O+^{198}Pt reaction and (b),(d) for ^{18}O+^{198}Pt reaction.

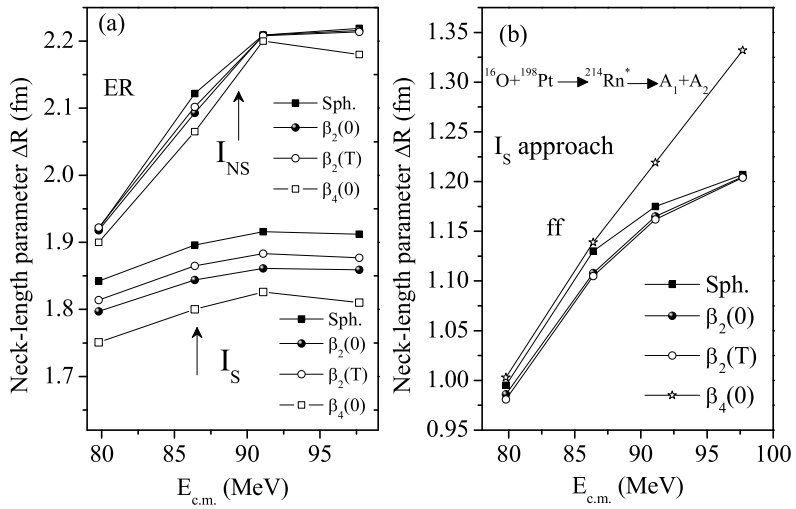

Figure 5.5: Variation of Neck-length parameter ΔR (fm) as a function of $E_{c.m.}$ (MeV) of both choices of moment of inertia for the decay of ^{214}Rn* CN into (a) ER and (b) ff fragments.

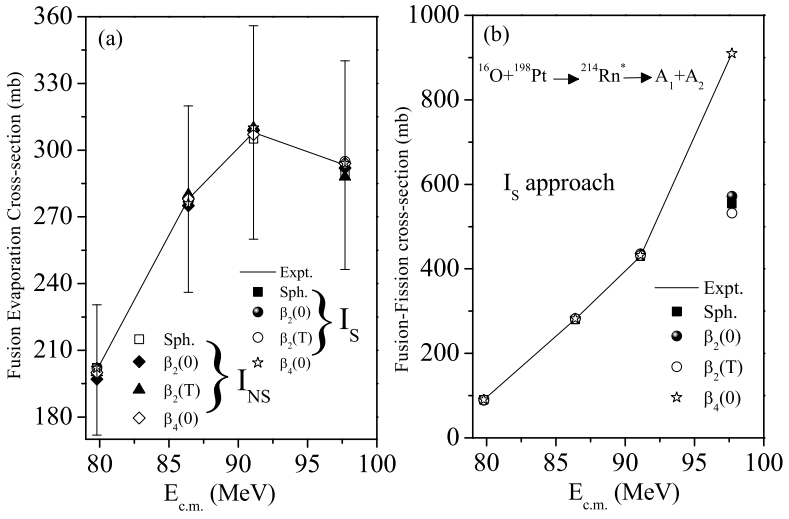

Figure 5.6: Comparison of (a) fusion evaporation and (b) fusion-fission cross-sections with experimental data [4,5] as a function of center of mass energy $E_{c.m.}$ for the decay of CN ^{214}Rn* formed in ^{16}O+^{198}Pt reaction using I_S and I_{NS} approaches.

of mass energy i.e. $E_{c.m.}$=79.8 MeV for both the reactions within sticking as well as non-sticking limit of interactions. On comparing the fission distribution of both compound systems, we observe the following: (i) within I_{NS} limit of MOI the decay of ^{216}Rn* CN show the asymmetric mass distribution for all considered choice of deformation. (ii) interestingly, for ^{216}Rn* compound system, the hump structure at A_2=84 (appearing for both I_{NS} and I_S limit) corresponds to existence of magic shell at N=50, which is not so prominent for neutron deficient system *i.e.* for ^{214}Rn* CN. It is important to note here that, for ^{214}Rn* nucleus the preformation factors for $\beta_2(0)$ and β_2-$\beta_4(0)$ deformations almost overlap with each other within both the choice of MOI (as shown in Fig. 5.4(a) and (b)), thereby suggesting the preformation of the same (symmetric and/or asymmetric) fragments for both the choices. Although, for ^{216}Rn* system, the variation between magnitude of $\beta_2(0)$ and $\beta_4(0)$ deformations is significant, shown respectively in Fig. 5.4(c) and (d). Therefore on broader view, we came to a conclusion that, with increase of two neutron in Rn CN, in addition to marginal change the magnitude of P_0, some structure variation is also perceived within both I_S and I_{NS} limit of MOI.

Table 5.1: The ER and fission cross-sections for $^{216}Rn^{*}$ system, calculated for moment of inertia in sticking limit using the DCM at different $E_{c.m.}$'s for static, dynamic deformations upto quadrupole (β_2) alone and static hexadecapole deformation ($\beta_4(0)$), compared with the experimental data [4, 5].

$E_{c.m.}$	Temp.	ΔR(fm)				$\ell_{max}(\hbar)$				σ_{DCM}(mb)				$\sigma_{Expt.}$(mb)
(MeV)	(MeV)	Sph.	$\beta_2(0)$	β_2(T)	$\beta_4(0)$	Sph.	$\beta_2(0)$	β_2(T)	$\beta_4(0)$	Sph.	$\beta_2(0)$	β_2(T)	$\beta_4(0)$	
Evaporation Residue (ER)														
76.0	1.391	1.807	1.773	1.791	1.740	132	135	134	134	174.0	174.0	175.0	176.0	174.7±25.0
79.8	1.447	1.884	1.846	1.866	1.813	131	135	133	133	302.0	301.9	301.0	300.0	301.9±43.6
91.9	1.614	1.953	1.909	1.932	1.880	132	137	136	135	469.0	472.0	472.0	474.0	472.0±74.1
96.6	1.674	1.957	1.910	1.932	1.857	133	137	136	138	458.0	459.7	458.0	458.0	459.7±73.5
Fusion-Fission (ff)														
76.0	1.391	0.897	0.913	0.859	0.925	137	141	140	138	32.6	31.4	34.2	33.6	32.77
79.8	1.447	0.980	0.981	0.961	1.014	137	140	140	138	78.4	77.0	76.8	76.0	77.21
91.9	1.614	1.198	1.174	1.169	1.253	139	143	142	141	536.0	544.0	540	536.0	536.8
96.6	1.674	1.21	1.215	1.197	1.317	140	144	142	144	500.0	656	624	774.0	776.4

Following the experimental data [4, 5] of ^{214}Rn* and ^{216}Rn* compound systems, we have addressed the ER and ff excitation functions within parameterizations of the neck length "ΔR" using both choices of MOI. The calculations are done by using spherical, temperature independent quadrupole β_2 and higher order $\beta_4(0)$ deformations as well as temperature dependent β_2 deformation. The cross-sections of ER are calculated at those energies, where ff data is available. Fig. 5.5 shows the variation of neck-length ΔR for ER and ff channels as a function of center of mass energy $E_{c.m.}$ for ^{214}Rn* system. Fig. 5.5(a) shows that, the magnitude of neck-length parameter for I_{NS} limit is much higher as compare to I_S limit and it increases with increase in center of mass energy, which is in accordance with the earlier work performed for relatively smaller compound systems ^{96}Tc* [19] using static-β_2 deformed nuclei. However, the present calculations preformed using spherical, $\beta_2(0)$, β_2(T) and $\beta_4(0)$ choices of deformations show similar behavior of ΔR within both I_{NS} and I_S limits. It is clearly observed from Fig. 5.5(a) that, within I_{NS} limit almost same neck-length is required to address ER data for all chosen spherical and deformed cases, which otherwise for I_S limit show deformation dependent behavior. The calculations performed for ff data reveal that, I_{NS} limit of MOI couldn't address the fission excitation function, thus in Fig. 5.5(b) the variation of ΔR for ff is shown only for the case of I_S limit. On comparing Fig. 5.5 (a) and (b), one may observe that, the neck-length for ff ($0.95<\Delta R<1.35$) is less in comparison to ER ($1.75<\Delta R<1.9$). Here the neck-lenght parameter 'ΔR' indicates the time scale of emission of a particular decay mode, so one may presume that ER process is occurring at an earlier instant as compared to that for ff process. The comparison of ER and ff cross-sections with experimental data is further shown in Fig. 5.6(a) and (b) respectively. It is clear from figure that, the data of both ER and ff is nicely addressed for the use of MOI in I_S limit, except at highest energy for ff which is fitted by inclusion of static higher order deformations i.e. $\beta_4(0)$ as shown in Fig. 5.6(b). Although, I_{NS} approach provides feasible addressal of data at all energies only for

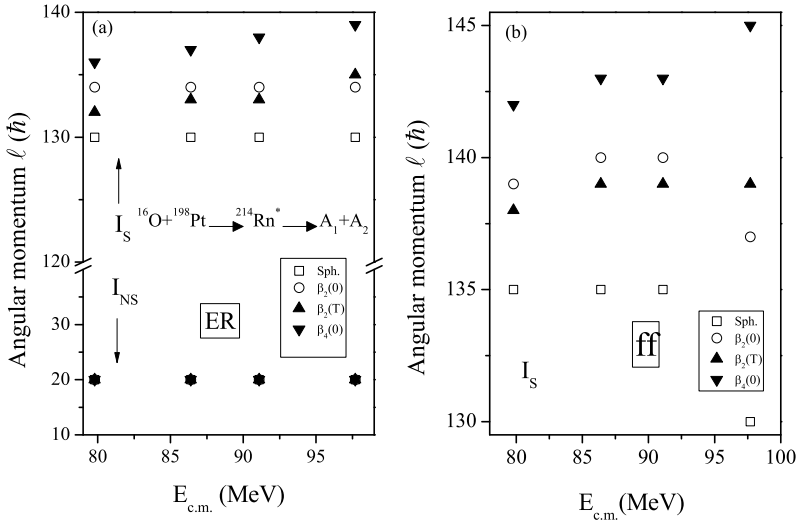

Figure 5.7: Variation of angular momentum ℓ ($\hbar$) calculated with both choices of moment of inertia for ^{16}O+^{198}Pt$\rightarrow^{214}$Rn* reaction (a) for ER and (b) for ff fragments as a function of $E_{c.m.}$.

ER channel, using spherical, $\beta_2(0)$, β_2(T) and $\beta_4(0)$ deformations but is unable to address ff data. This might be because of following reasons, (i) within I_{NS} limit, one of the contributing factor towards cross-sections, the preformation probability of ff fragments is negligibly small i.e. $\sim < 10^{-10}$, which otherwise is significantly large for I_S limit (see Fig. 5.4). (ii) the contributing ℓ-values are much quite small for I_{NS} limit as compared to I_S limit (as shown in Fig. 5.7), which could be the another possible reason for not acquiring the ff data within non-sticking limit. Same observations are obtained for ^{216}Rn* nucleus as depicted in Table 5.1. Therefore one may conclude that, the sticking limit (I_S) of MOI with the effect of higher order of deformation $\beta_4(0)$ support the fission excitation functions, whereas for evaporation residue cross-sections, both I_S and I_{NS} approaches are reasonably good within chosen cases of spherical and deformed fragments.

One interesting fact to be observed here is that, with the increase of two neutron, the ER cross-section is enhanced i.e. ^{216}Rn* has more σ_{ER} than ^{214}Rn*. It is possibly due to the reason that, the decay barrier height of ^{216}Rn* is lower than ^{214}Rn* (^{214}Rn*:V$_B$=75.05 MeV and ^{216}Rn*:V$_B$=74.11 MeV). Since lower is the decay

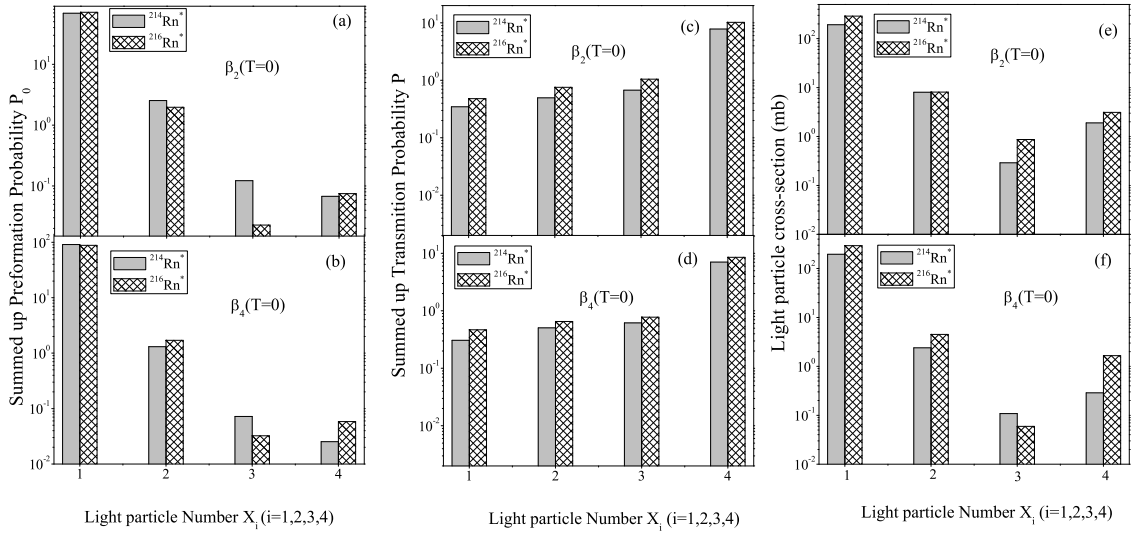

Figure 5.8: The summed up preformation probability P_0, transmission probability P, and particle cross-sections of two compound nuclei $^{214,216}Rn^*$ calculated by using static quadrupole deformation shown in upper panel and hexadecapole deformation shown in lower panel plotted as a function of light mass number X_i (i=1, 2, 3,4).

barrier height, greater would be the decay probability and consequently measured cross-section of the ER fragments for $^{216}Rn^*$ become larger than those of $^{214}Rn^*$ compound nucleus. In order to clarify this point further, an effort is made, where the individual contribution of ER cross-sections of both compound nuclei $^{214,216}Rn^*$ are tested in the form of summed up preformation probability and barrier transmission probability of decaying fragments using static β_2 and β_4 choices of deformed fragments. In view of this, Fig. 5.8 is plotted, showing the variation of summed up preformation factor P_0, barrier penetrability P and ER cross-section σ_{ER} (i.e. A_2=1n, 2n, 3n, 4H) [21] using sticking limit of MOI. It is evident from Fig. 5.8(a) and (b) that, the P_0 show decrement in its values with increase in light mass fragment i.e. $P_0{}^{1n}>P_0{}^{2n}>P_0{}^{3n}>P_0{}^{4H}$. In view of Eq. (2.28) of chapter 2, one may see that preformation is directly related with the hydrodynamical mass parameter $B_{\eta\eta}$, greater the value of $B_{\eta\eta}$, more will be the preformation probability. $B_{\eta\eta}$ for 1n is higher and least for ^4H fragment and consequently similar trend is observed in P_0 as shown in Fig. 5.8(a,b). The summed up preformation probability of both $^{214}Rn^*$ and $^{216}Rn^*$ compound nuclei is different but above mentioned trend is followed in

both the cases. However, in the case of transmission probability P, the reverse pattern is pointed out *i.e.* $P^{1n}<P^{2n}<P^{3n}<P^{4H}$ as shown in Fig. 5.8(c) and (d). It is clear from Eq. 2.34 that, the penetrability is decided by the first and second turning points of decay barrier. The first turning point R_a of 1n fragment is far away from the second turning point R_b thereby decreasing the penetrability and start closer for $2n$, $3n$ and $4H$ fragments, consequently P start increasing for them. For all light mass fragments, P is greater for $^{216}Rn^*$ in comparison to $^{214}Rn^*$. Therefore, using quadrupole deformation, the combined effect of P_0 and P is such that, 1n particle cross-sections of $^{216}Rn^*$ are higher than $^{214}Rn^*$ followed by 2n, 4H and 3n particles (as shown in Fig. 5.8(e)). Whereas on adding hexadecapole deformations, same systematic is obeyed, except for 3n-particle, for which higher order deformation of corresponding daughter fragment seem to play significant role which is analysed further in Fig. 5.8(f).

Now, within I_{NS} and I_S limits of interactions, the barrier lowering effect is also worked out, as an inbuilt property of the DCM. The neck-length ΔR fixes the barrier lowering ΔV_B, for best fit to the ER and ff data. The barrier modification ΔV_B depends upon the barrier height V_B and barrier penetration point $V(R_a)$ as shown in Eq. (2.52) of chapter 2. The Fig. 5.9 illustrates the barrier lowering ΔV_B for $^{16}O+^{198}Pt$ reaction as a function of angular momentum ℓ for both choices of MOI using β_2-static and β_4-static deformed cases. The left and right panels of figure depict the ΔV_B respectively for ER and ff processes. It is clear from Fig. 5.9(a) that, for ER channel, irrespective of moment of inertia, ΔV_B decrease (in magnitude) with increase in ℓ-value of the system independent of the order of deformation. On the other hand for I_S limit, in order to address ER cross-section, one need to modify barrier more as compared to I_{NS} limit (shown in inset of Fig. 5.9(a)), as the barrier lowering is larger (in magnitude) for I_S limit of interaction as compared to I_{NS} limit. One may remind here that, in I_{NS} approach, ΔR is higher in magnitude, and increase in ΔR shows that the first turning point approaches close to the barrier

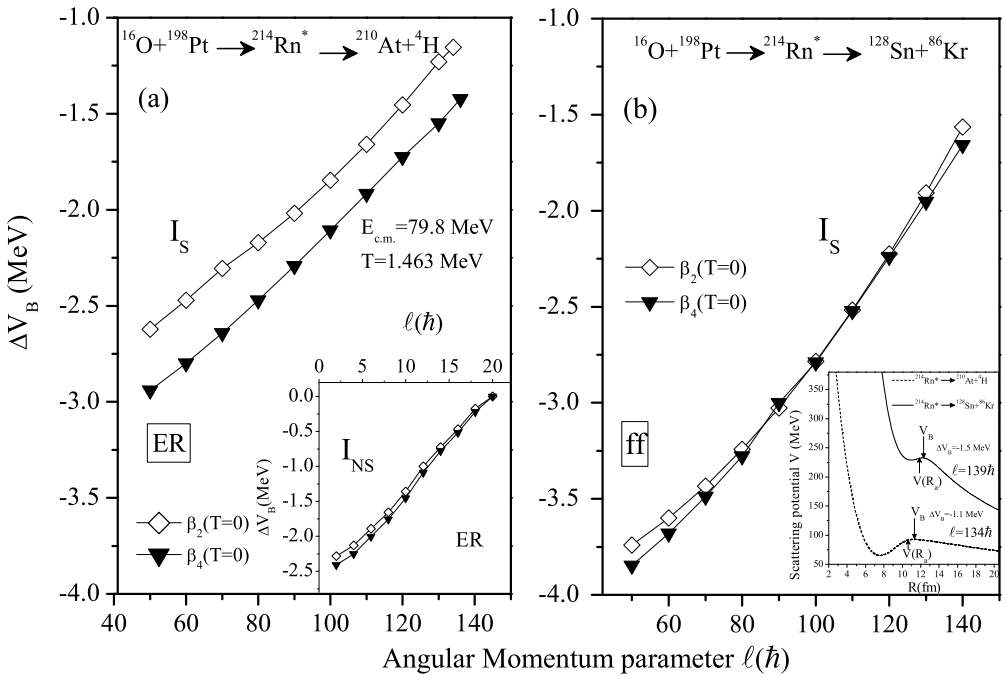

Figure 5.9: Variation of barrier lowering parameter ΔV_B for (a) ER and (b) ff fragment as a function of angular momentum $\ell(\hbar)$ using $\beta_2(0)$ and $\beta_4(0)$ deformed nuclei with sticking limit of moment of inertia for ^{16}O+^{198}Pt channel. Inset in (a) shows the ΔV_B within non-sticking limit of moment of inertia. Inset in (b) depicts the scattering potential for the decay of ^{214}Rn* into ER and ff channels.

height, which inturn indicate that the barrier lowering (ΔV_B) parameter decreases as compared to I_S approach. The difference in barrier lowering is further analyzed for two exit channels i.e. the decay of ^{214}Rn* into ^{210}At+^{4}H for ER and to ^{128}Sn+^{86}Kr for ff as shown in Fig. 5.9(a) and (b). Figures depict that, though the variation of ΔV_B is almost similar for both the exit channels (ΔV_B increases almost linearly with angular momentum ℓ), but the magnitude of ΔV_B is larger for ff as compared to ER. This means that, lesser barrier modification is required for ER decay. This point is clarified in the inset of Fig. 5.9(b), by plotting the scattering potential V(R) for the above mentioned ER and ff decay channels. One may observe that, the potential at first turning point V(R_a) and barrier height V_B are different for both the channels and consequently the ΔV_B gets modified. The different values of V(R_a) for both the exit channels are related with the corresponding choice(s) of neck-length parameter

ΔR. For the addressal of ER data, a larger neck-length is required as compared to ff (see Fig. 5.5) and therefore the first turning points are influenced accordingly. The barrier height V_B is also modified as we move from smaller fragments to bigger ones. As a result of this, the barrier modification is distinct for ER and ff like fragments as represented in Fig. 5.9 (a) and (b). Similar observation are drawn for ^{216}Rn* systems, but not discussed here to avoid the repetition. Thus the present study clearly emphasize that the different limits of MOI significantly influence the barrier modification parameter which inturn help to address the excitation functions of different nuclear systems.

5.2.3 Survival Probability and prediction of fission cross-sections

In addition to above, the survival probability W_{sur} of ER is calculated for both compound nuclei ^{214,216}Rn* as shown in Fig. 5.10. The figure is plotted in view of sticking limit of MOI as it is applicable for both ER and ff processes. The comparison is made at those excitation energies where experimental ff data is available. The W_{sur} is obtained by ratio of the evaporation residue cross section σ_{ER} to the CN formation cross section σ_{CN} (*i.e.* a sum of σ_{ER} and fusion-fission cross section σ_{ff}), each calculated as the dynamical fragmentation process, *i.e.* survival probability $W_{sur}= \frac{\sigma_{ER}}{\sigma_{CN}}$, where $\sigma_{CN}=\sigma_{ER} + \sigma_{ff}$. The survival probability W_{sur} is estimated for spherical as well as $\beta_2(0)$, β_2(T) and β_4 (0) choices of decaying fragments. It is clearly observed from Fig. 5.10 that, only β_4-choice of deformation is able to reproduce the experimental survival probability of the considered nuclei at all center of mass energies. Moreover, the W_{sur} of ^{214,216}Rn* decreases with increase in energy of the system, this essentially means that at highest energy, fission becomes the dominate mode of decay. Table 5.1 and Fig. 5.6 also show that, with increase in energy the experimental ER cross-sections decrease and ff start increasing. Here, an increase in survival probability with neutron number is also observed as depicted

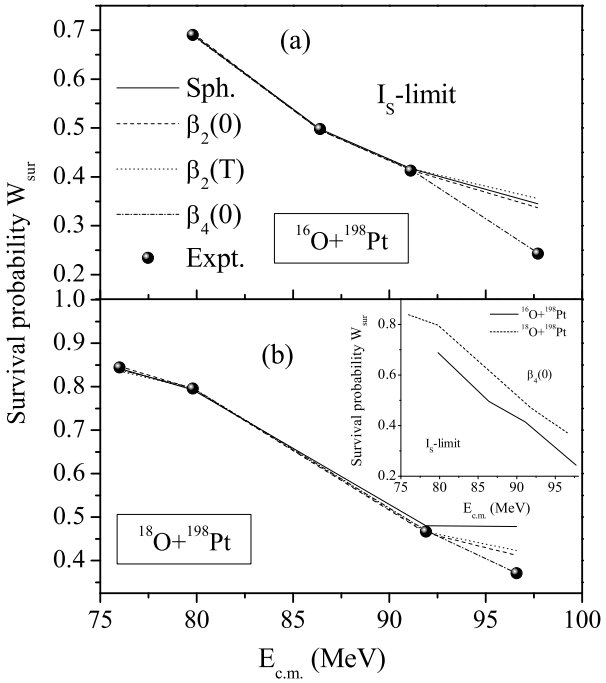

Figure 5.10: Comparison of DCM calculated ER survival probability W_{sur} with center of mass energy for $^{16}O+^{198}Pt$ and $^{18}O+^{198}Pt$ channels using different choices of nuclei. Inset shows the comparison of W_{sur} of $^{16,18}O+^{198}Pt$ channels with hexadecapole deformation only.

in inset of Fig. 5.10(b). For $^{216}Rn^*$ system with neutron number N = 130 has higher value of W_{sur} and attain more stability against fission as compared to $^{214}Rn^*$ with N = 128. Finally, the ff cross-sections ($\sigma_{fission}$) are predicted for $^{214,216}Rn^*$ systems in missing energy range using the MOI in sticking limit. Since, in order to fit ff excitation-functions, hexadecapole deformations are playing significant role, therefore prediction is done by including $\beta_4(0)$ deformations only. The systematics of neck-length ΔR is used in order to predict the fission data by employing polynomial fitting of order 2 which reads as,

$$\Delta R = -1.60234 + 0.0444E_{c.m} - 1.4709 \times 10^{-4}E_{c.m}^2 \tag{5.1}$$

for $^{214}Rn^*$ and for $^{216}Rn^*$ as

$$\Delta R = -2.80187 + 0.07253E_{c.m} - 3.0928 \times 10^{-4}E_{c.m}^2 \tag{5.2}$$

Table 5.2: Predicted fission cross-sections of ^{214,216}Rn* systems, calculated via the DCM using static hexadecapole deformation ($\beta_4(0)$).

$E_{c.m.}$(MeV)	Temp. (MeV)	ΔR(fm)	$\ell_{max}(\hbar)$	σ_{DCM}(mb)	$\sigma^{Expt.}$(mb)
		^{16}O+^{198}Pt$\rightarrow^{214}$Rn*			
72.1	1.346	0.834	141	17.5	—
75.1	1.393	0.902	141	32.8	—
77.9	1.435	0.963	142	64.0	—
79.8	1.463	1.003	142	90.0	90.0
81.6	1.489	1.041	142	124.4	—
85.2	1.540	1.112	143	236.0	—
86.4	1.556	1.139	143	282.0	280.97
88.8	1.589	1.180	143	370.0	—
91.1	1.619	1.219	143	432.0	430.61
93.0	1.644	1.254	143	578.0	—
94.8	1.667	1.284	143	678.0	—
97.7	1.704	1.332	145	910.0	910.0
		^{18}O+^{198}Pt$\rightarrow^{216}$Rn*			
71.4	1.319	0.8	138	9.62	—
76.0	1.391	0.925	138	33.6	32.77
79.8	1.447	1.014	138	76.0	77.21
84.4	1.513	1.116	138	175.4	—
88.2	1.565	1.189	139	322.0	—
91.9	1.614	1.253	141	536.0	536.8
96.6	1.674	1.317	144	774.0	776.4

Using the $E_{c.m.}$ of ER as input, the neck length ΔR is obtained and is used to estimate $\sigma_{fission}$ for ^{214,216}Rn* nuclei. The predicted cross-sections and the corresponding ΔR and ℓ-values are given in Table 5.2. An experimental verification is called for these predicted fission cross sections.

5.3 Conclusions

In this chapter, a comparative analysis of sticking and non-sticking limits of moment of inertia (MOI) is carried out in the reaction dynamics of ^{214,216}Rn* compound nuclei formed respectively in ^{16,18}O+^{198}Pt channels. For the purpose, spherical, quadrupole

deformed β_2 (static and dynamic) and static hexadecapole deformed $\beta_4(0)$ choices of interaction are considered. It is observed that, the choice of moment of inertia (MOI) significantly influences the barrier height (corresponding position) and the preformation paths of fragments formed at compound nuclear stage. The DCM based calculations suggest that, spherical and β_2(T) deformation behave alike whereas static $\beta_2(0)$ and $\beta_4(0)$ deformations behave similar in preformation plot. The ER and ff cross-sections are calculated by employing both the limits of moment of inertia. We could account successfully the data of ER within both I_S and I_{NS} interactions at all incident energies for spherical as well as deformed choices of decaying fragments. However, ff data is addressed only within I_S limit, specially after including deformations upto $\beta_4(0)$. The fitting is done by optimizing the neck-length 'ΔR'. Independent of deformation and orientation effects, $\Delta R_{I_{NS}} > \Delta R_{I_S}$ limit, which means that, larger barrier modification is required for the use of I_S as compared to that for I_{NS} limit. Furthermore, the survival probability is estimated for both compound nuclei and it is observed that $^{216}Rn^*$ with N=130 shows greater stability against fission as compared to $^{214}Rn^*$ with N=128. Finally, an effort is made to predict the ff data for $^{214,216}Rn^*$ compound nuclei by including higher order deformations (β_4) within sticking limit of MOI.

After explored the effect of entrance channel, excitation energy, angular momentum and deformations in chapters 3 to 5. An attempt is made to study the use of different nuclear interaction potentials in dynamics of light mass nuclei as discussed in next chapter.

Bibliography

[1] A. C. Berriman, D. J. Hinde, M. Dasgupta, C. R. Morton, R. D. Butt and J. O. Newton, Nature (London) **413**, 144-147 (2001).

[2] P. Fröbrich and I. I. Gontchar, Nucl. Phys. A **563**, 326 (1993).

[3] W. Ye, Phys. Rev. C **81**, 011603 (2010).

[4] R. Sandal *et al.*, Phys. Rev C **91**, 044621 (2015).

[5] R. Sandal *et al.*, DAE Symp. on Nucl. Phys. **57**, 534 (2012).

[6] N. Cindro and D. Pocanic, J. Phys. G: Nucl. Part. Phys. **6**, 359-366 (1980).

[7] R. Aroumougame, N. Malhotra, S. S. Malik, and R. K. Gupta, Phys. Rev. C **35**, 3 (1987).

[8] R. K. Gupta, in *Cluster in Nuclei*, Lecture Notes in Physics 818, Vol. I, edited by C. Beck (Springer-Verlag, Berlin), p. 223 (2010).

[9] Rajni, R. Kumar, and M. K. Sharma, Phys. Rev C **90**, 044604 (2014).

[10] B. B. Singh, M. K. Sharma, and R. K. Gupta, Phys. Rev. C **77**, 054613 (2008).

[11] J. Blocki, J. Randrup, W. J. Swiatecki, and C. F. Tsang, Ann. Phys. (NY) **105**, 427 (1977).

[12] G. Sawhney, R. Kumar, and M. K. Sharma, Phys. Rev. C **86**, 034613 (2012).

[13] R. K. Gupta, M. Balasubramanium, R. Kumar, N. Singh, M. Manhas, and W. Greiner, J. Phys. G: Nucl. Part. Phys. **31**, 631 (2005).

[14] R. K. Gupta, M. Manhas, and W. Greiner, Phys. Rev. C **73**, 054307 (2006).

[15] P. Moller and J. R. Nix, Nucl. Phys. A **361**, 117 (1981).

[16] As. Jensen and J. Damgaard, Nucl. Phys. A **203**, 578 (1973); M. Muenchow and W. Scheid, Nucl. Phys. A **468**, 59 (1987).

[17] G. Sawhney, R. Kumar, Rajni, and M. K. Sharma, AIP Conf. Proc. **1524**, 174 (2013).

[18] R. K. Gupta, Niyti, M. Manhas, and W. Greiner, J. Phys. G: Nucl. Part. Phys. **36**, 115105 (2009).

[19] G. Kaur, N. Grover, K. Sandhu, and M. K. Sharma, Nucl. Phys. A **927**, 232-248 (2014).

[20] K. Sandhu, M. K. Sharma, A. Kaur, and R. K. Gupta, Phys. Rev. C **90**, 034610 (2012).

[21] S. K. Arun, R. Kumar, and R. K. Gupta, J. Phys. G: Nucl. Part. Phys. **36**, 085105 (2009).

Chapter 6

Use of different nuclear interaction potentials in dynamics of light mass nuclei

6.1 Introduction

In previous chapters, nuclear interaction potential is obtained via the analytical methods such as Blocki based pocket formula. Such kind of approaches does not contain spin-orbit coupling effects, though they affects the fusion-fission dynamics appreciably. In this chapter, the coupling effects are accounted using different Skyrme forces. For this study, semi-classical energy density formalism is applied, where one can individually focus on spin-orbit density dependent and density independent parts of nuclear potential. The effect of deformation and related orientations of colliding nuclei is duly incorporated in the calculations and the results are discussed in section 6.2.1. Furthermore, the role of double spin-orbit parameters (W_0 and W_0') in spin-orbit dependent potential is explored view of SkI2, SkI3 and SkI4 Skyrme forces, discussed in section 6.2.2. In addition to this, the decay of $^{72}Se^*$ compound nucleus is examined via both SEDF and Blocki *et al.* potential and efforts are made to address fusion hindrance phenomena as described in section 6.3.

Finally the outcomes of this chapter are presented in section 6.4.

6.2 Deformation and orientation effects on spin-orbit density dependent (V_J) and independent (V_P) potentials

The aspect of nuclear deformations has been continually probed to analyze the fusion-fission processes. A lot of work has been done by taking one of the target or projectile as deformed nucleus [1–4]. When the nuclear deformations are incorporated in theoretical calculations, it is inherently necessary to account for the relative orientation of the projectile and target nucleus for better understanding of subsequent fusion dynamics. The orientation of the interacting nuclei has a significant influence on the fusion barrier height and also affects the compactness of the touching configuration. In order to have a better understanding of fusion barrier characteristics, the contribution of nuclear interaction potential plays a significant role. Various microscopic [5–7] and analytical approaches [8–10] have been developed in literature to understand the nucleus-nucleus interaction potential. The advantage of Skyrme based interactions over the competing proximity potentials is that, they give detailed information about the interactions of individual nucleons where the role of spin-orbit dependent and spin-orbit independent parts can be analyzed separately. In this work, semi-classical Skyrme energy density formalism (SEDF) is used to estimate the individual contribution of spin-orbit density dependent V_J and spin-orbit density independent V_P part of interaction potential. Until now [4, 11–13], the contribution of V_J is explored by considering single spin-orbit parameter (*i.e.* W_0) only. In the present study, the role of double spin-orbit parameter W_0 and W_0' is explored in the framework of semi-classical SEDF approach. Reinhard and Flocard [14] have used a systematic fitting procedure and determined five parameterizations of the Skyrme functional. Out of these five, we have used

three Skyrme forces *i.e.* SkI2, SkI3 and SkI4. The set SkI2 belongs to the standard Skyrme functional. For the set SkI3, authors have enforced the constraint W_0'=0. In this way, they impose a density dependence of the spin-orbit form factor proportional to ρ=ρ_p+ρ_n as in the relativistic mean field (RMF) calculations. With SkI4 Skyrme force, they have investigated the generalized Skyrme parametrization with the spin-orbit functional [15].

6.2.1 Influence of projectile shapes on V_J analyzed via Si-induced reactions

The role of deformation (quadrupole deformed β_2) and orientation is investigated on spin-orbit density dependent potential V_J of nuclear potential. Here, an effort is made to analyze the possible role of orientation degree of freedom on spin-orbit part via different β_2-deformed shapes. To facilitate discussion on V_J due to shape and orientation of deformed nuclei, calculations are performed for various Si-induced reactions *i.e.* ^{24}Si+^{30}Si, ^{26}Si+^{30}Si, ^{28}Si+^{30}Si, ^{38}Si+^{30}Si ^{40}Si+^{30}Si, ^{42}Si+^{30}Si, ^{44}Si+^{30}Si,^{46}Si+^{30}Si, ^{48}Si+^{30}Si, ^{50}Si+^{30}Si, ^{52}Si+^{30}Si and ^{54}Si+^{30}Si having quadrupole deformation (β_2) within range of $0.023 \leq \beta_2 \leq 0.531$ (for prolate) and $-0.242 \leq \beta_2 \leq -0.592$ (for oblate). The above mentioned reactions are chosen because the target ^{30}Si is spherical, whereas projectiles are weakly and highly deformed with prolate (p) and oblate (o) shapes. The ground state deformation of nuclei are taken from the work of Moller and Nix [16]. The SKRA Skyrme force [17] is opted for the study, because parameter set obtained from this force seem to address the nuclear interactions adequately. Further the effect of spin-orbit term is explored on fusion cross-sections (σ_{fusion}) obtained by using Wong formula [18].

First of all, we study the effect of orientation on spin-orbit potential by considering weakly and highly prolate systems i.e. ^{46}Si+^{30}Si and ^{54}Si+^{30}Si respectively as shown in left and right panels of Fig. 6.1. The variation of V_J is shown for different orientation degree of freedom θ *i.e.* from 0^0 to 90^0. It is observed from Fig.

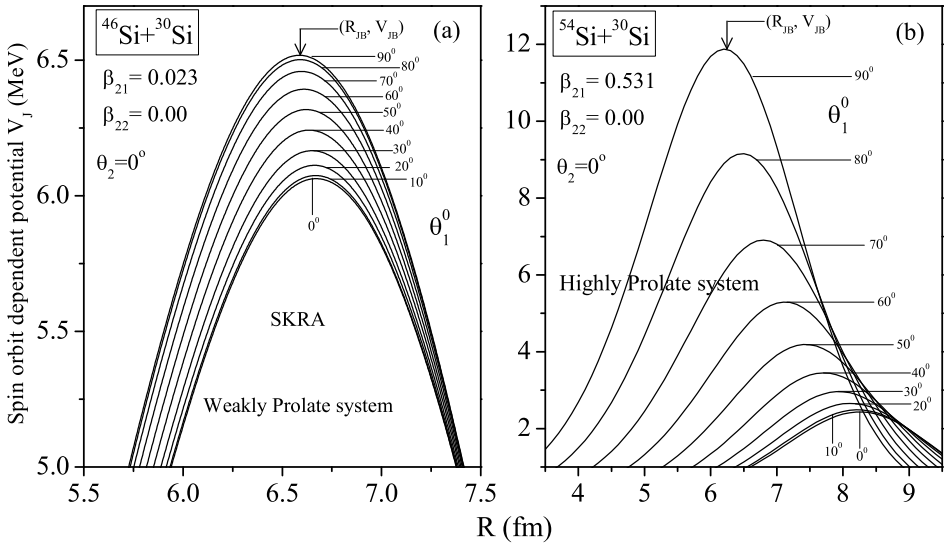

Figure 6.1: Figure shows the variation of spin-orbit dependent part V_J(R) of interaction potential, plotted for different orientation degree of freedom θ (a) for weakly prolate and (b) for highly prolate deformed nuclei. V_{JB} represent the maximum value of V_J and R_{JB} is corresponding position, different for different orientations.

6.1(a) that, for weakly prolate system with β_{21} =0.023 and β_{22} =0.00, V_J increases slowly with the change in orientation of projectile from 0^0 to 90^0. At an orientation θ=0^0, the height of spin-orbit barrier is $\sim$ 6.0 MeV, which for orientation angle of θ=90^0, increases to $\sim$ 6.5 MeV. Apparently, the spin-orbit barrier position R_{JB} is also affected by the orientation angles between the projectile and target as the maximum R_{JB} corresponds to θ_1=0^0 and the minimum to θ_1=90^0. On changing the orientation from θ_1 =0^0 to 90^0, the spin-orbit barrier position is shifting $\sim$ 0.1 fm towards lower interaction radius, making system more compact. Similar results are obtained for highly prolate system i.e. for ^{54}Si+^{30}Si reaction with β_{21} =0.531 and β_{22} =0.00 as depicted in Fig. 6.1(b). One may clearly see that, the enhancement in magnitude of V_J with respect to orientation degree of freedom is significantly high for highly prolate projectile as compare to weakly prolate ones. At an orientation angle of 90^0, V_J of highly prolate system is $\sim$ 6 MeV higher than weakly prolate system.

Further, the effect of orientation on spin-orbit part is analyzed through weakly

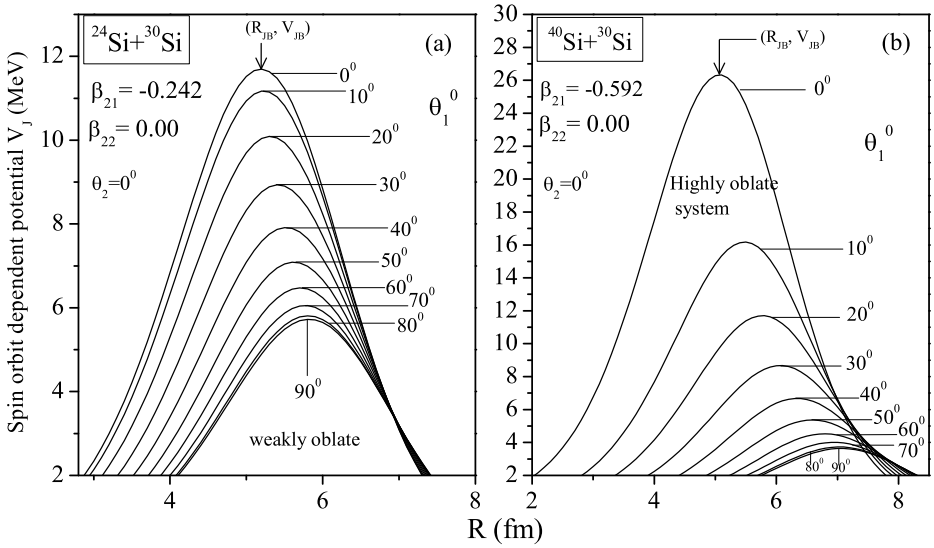

Figure 6.2: Same as Fig. 6.1 but for oblate shape nuclei.

and highly oblate shape nuclei as shown in Fig. 6.2. It is evident from the figure that, regardless of magnitude of deformation, the decrement in magnitude of spin-orbit barrier height V_{JB} is observed from orientation 0^0 to 90^0 (see Fig. 6.2(a) and Fig. 6.2(b)). The highest spin-orbit barrier and lowest spin-orbit position is attained at θ_1=0^0, θ_2=180^0. On changing the orientation of projectile from 0^0 to 90^0, the V_J get affected as following: (i) the V_{JB} of weakly oblate system decreases by about $\sim$ 6.0 MeV and shifts the spin-orbit barrier position $\sim$ 0.6 fm towards higher interaction radius i.e. more elongated. (ii) for highly oblate system, the V_{JB} is decreased by $\sim$ 23.0 MeV and R_{JB} moved $\sim$ 2.0 fm towards higher interaction radius.

Moreover, on comparing V_{JB} of weakly prolate (Fig. 6.1(a)) and weakly oblate system (Fig. 6.2(a)) at their respective optimum orientations, we find that, in comparison to weakly prolate system, V_{JB} of weakly oblate system is enhanced by about $\sim$ 5.2 MeV. However, V_{JB} of highly oblate system is $\sim$ 14.4 MeV higher than highly prolate system (see Fig. 6.1(b) and 2(b)).

The above analysis is further extended for other Si+Si reactions, where magnitude of deformation is in between $0.023 \leq \beta_2 \leq 0.531$ for prolate and $-0.242 \leq \beta_2 \leq$

Table 6.1: The spin-orbit barrier height V_{JB} and spin-orbit barrier position R_{JB} of various prolate and oblate deformed systems with their optimum orientations [19]. The coulomb barrier V_{CB} is also shown in table below. β_2-deformations are taken from the theoretical work of Moller and Nix [16]. β_{21} and β_{22} represents the deformation of projectile and target respectively.

A_P (Si)	A_T (Si)	θ_1	θ_2	β_{21}	β_{22}	V_{CB} (MeV)	V_{JB} (MeV)	R_{JB} (fm)
Prolate deformed nuclei								
38	30	90	0	0.234	0	26.360	8.185	6.0
46	30	90	0	0.023	0	25.092	6.526	6.6
52	30	90	0	0.490	0	25.254	11.323	6.2
54	30	90	0	0.531	0	25.119	11.875	6.2
Oblate deformed nuclei								
24	30	180	0	-0.242	0	29.320	11.695	5.2
26	30	180	0	-0.353	0	29.266	14.548	5.1
28	30	180	0	-0.478	0	29.351	19.11	4.9
40	30	180	0	-0.592	0	29.975	26.321	5.1
42	30	180	0	-0.321	0	26.554	13.169	5.7
44	30	180	0	-0.263	0	26.110	11.502	5.9
48	30	180	0	-0.398	0	26.232	16.467	5.7
50	30	180	0	-0.422	0	26.154	17.794	5.7

-0.592 for oblate systems. All prolate/oblate projectiles show similar result as discussed above (therefore not shown here to avoid repetition). Table 6.1 summarizes the result for all considered reactions with their spin-orbit barrier height and barrier position calculated at the optimum orientations (θ_1, θ_2). The present study suggest that, the magnitude of prolate/oblate deformations and corresponding orientation angle between the colliding nuclei, significantly influence the spin-orbit barrier height and position. Moreover, the compactness of the system also gets affected with the sign of β_2-deformation.

Now to analyze the role of spin-orbit density dependent potential in the total interaction potential (V_T=V_P+V_J+V_C=V_N+V_C), the spin-orbit independent potential (V_P) and Coulomb potential (V_C) parts are added to it. Fig. 6.3 shows the total interaction potential with and without the contribution of spin-orbit effect for ^{40}Si+^{30}Si reaction plotted at Coulomb barrier energy i.e. E_{CB}=29.98 MeV (tem-

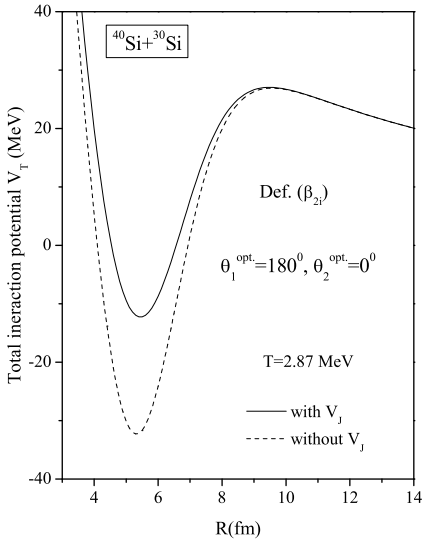

Figure 6.3: Total interaction potential V_T (MeV) of ^{40}Si+^{30}Si reaction as a function of inter nuclear distance R (fm) plotted with and without spin-orbit density effects at optimum orientations $\theta_1^{opt.}$=180^0 and $\theta_2^{opt.}$=0^0.

perature T=2.87 MeV). It is clear that, impact of spin-orbit part is significant on fusion pocket rather than on fusion barrier height. As, pocket becomes more shallower with inclusion of V_J. Moreover, the barrier curvature ($\hbar\omega$) also gets reduced with the inclusion of spin-orbit potential. In view of this, it is of further interest to study the influence of V_J on fusion cross-sections. The fusion excitation functions are calculated with and without the inclusion of V_J in the total interaction potential and plotted at different orientations as shown in Fig. 6.4. Calculations are performed using Wong formula for ^{38}Si+^{30}Si and ^{40}Si+^{30}Si reactions with respective prolate and oblate shapes. Since no experimental data is available for these reactions, therefore cross-sections are estimated at their respective Coulomb barrier energy (see Table 6.1). It is to be observed here that, the spin-orbit density part decreases the fusion cross-sections to a small extent. This fall off in cross-section is about $\sim$ 10 mb for prolate system and $\sim$ 20 mb for oblate system. As expected, for prolate system (as shown in Fig. 6.4(a)), independent of spin orbit effect, the fusion cross-sections are decreasing with increase in orientation angle of colliding nuclei with maxima at θ_2=0^0. On the other hand, for oblate nuclei, σ_{fusion} increases with

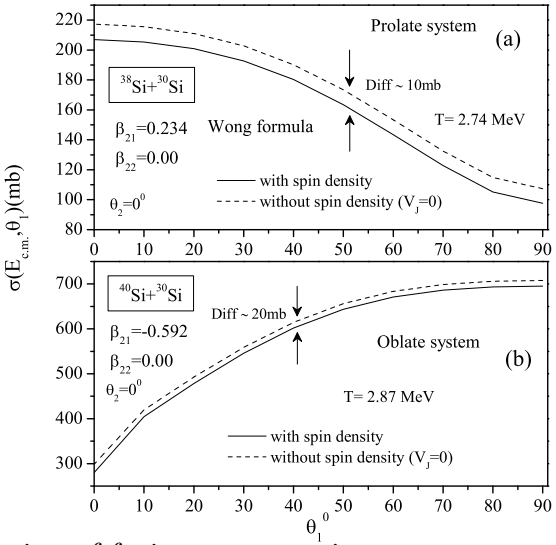

Figure 6.4: Variation of fusion cross-section σ_{fusion} at each angle with and without spin density effects (a) for prolate and (b) for oblate shape nuclei, plotted at their coulomb barrier energy (see Table 6.1).

increase in orientation angle of colliding nuclei and becomes maximum at θ_2=90^0 as shown in Fig. 6.4(b). For in between configurations the fusion cross-sections vary smoothly as a function of orientation angle. The above study suggest that, for oblate-spherical shape system, the spin-orbit barrier finds most compact configuration at orientation $(0^0, 180^0)$, which for prolate-spherical system obtained at $(90^0, 180^0)$. Now, this result is used to extend our study for understanding the effect of both spin-orbit dependent and independent parts on two nucleon transfer process forming same *Se* compound nucleus. Beside this the effect of N/Z ratio of Se nuclei is analyzed and the results are discussed in upcoming section.

6.2.2 Two nucleon transfer effects on V_J and V_P

Foremost, we have calculated the spin-orbit density dependent interaction potential for the two nucleon transfer channels using SIII Skyrme force [20] within semi-classical SEDF approach. We started with ^{23}Na+^{49}V reaction adopting two-nucleon transfer from target to projectile and worked on ^{25}Mg+^{47}Ti, ^{27}Al+^{45}Sc,^{29}Si+^{43}Ca and ^{31}P+^{41}K reactions- all giving the same compound system ^{72}Se* (as shown in

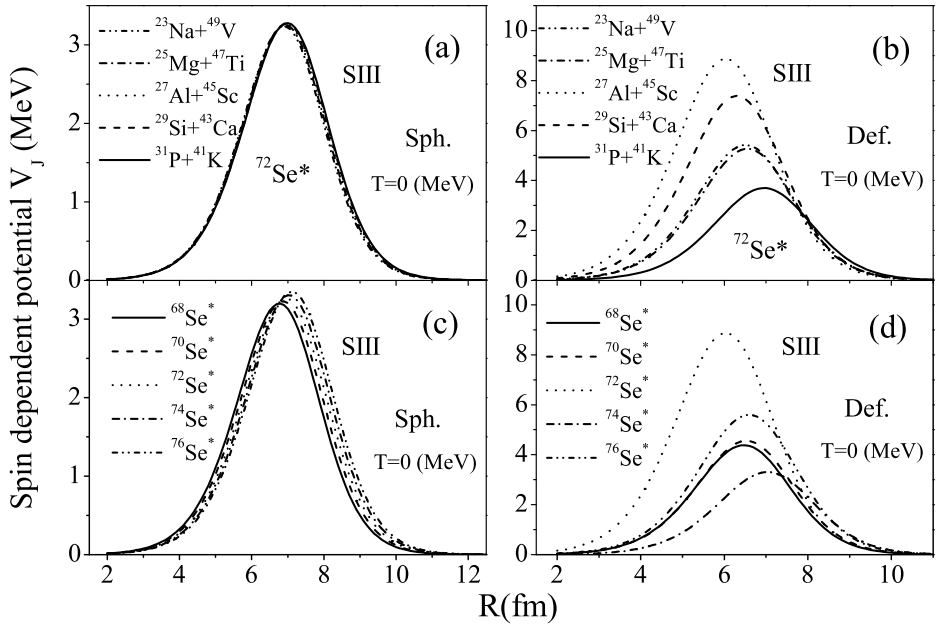

Figure 6.5: The spin-orbit interaction potential V_J as a function of R at T=0 (MeV) using SIII force for (a,b) two nucleon transfer products starting with ^{23}Na+^{49}V reaction and (c,d) for increase in N/Z ratio of Se via increase in neutron in the projectile nucleus, starting from ^{23}Al+^{45}Sc$\rightarrow^{68}$Se*. Left panel show the case for spherical nuclei and right panel for β_2-deformed nuclei.

Fig. 6.5(a) and Fig. 6.5(b)). The calculations are done for both spherical as well as deformed choices of colliding partners. It is to be noted here that, in view of results of Fig. 6.1 and Fig. 6.2, the variation of V_J in our further study is shown at optimum orientation only.

Fig. 6.5(a) shows that for spherical choice of colliding nuclei, the spin barrier height (V_{JB}) and the spin barrier position (R_{JB}) remain almost constant for simultaneous addition and stripping of two nucleon in projectile and target respectively. However, on allowing deformation effects, the enhancement in V_{JB} is higher, specially for oblate shape nuclei followed by prolate and then spherical choice of projectile-target combination. Interestingly, for oblate shape nuclei, with the increase in V_{JB}, spin barrier position shifts towards the smaller interaction radius in contrast to spherical case. The result obtained using deformed nuclei are in accordance with our previous study done with Si-induced reactions and also independent of the chosen Skyrme force. Thus, in transfer process, the different spherical reacting partners experience the maximum repulsion at about same distance whereas the

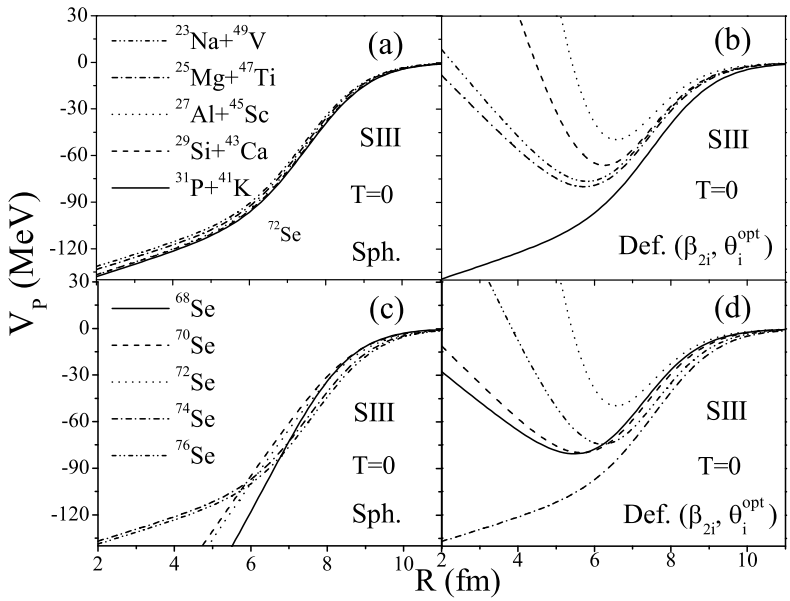

Figure 6.6: Same as Fig. 2 but for spin-orbit independent part V_P of interaction potential.

deformed nuclei, exhibit maximum repulsion at different interaction radius.

In order to see the dependence of N/Z ratio of Se on V_J, we have made calculations for $^{68-76}$Se* isotopes as shown in Fig. 6.5(c) and Fig. 6.5(d). In lower panel of Fig. 6.5, various isotopes of Se* are chosen starting with the target-projectile combination of ^{23}Al + ^{45}Sc forming ^{68}Se* compound system. Different isotopes of Se are formed by using stable ^{45}Sc target and adding two successive neutrons to the ^{23}Al projectile. One may note from Fig. 6.5(c) that, the spin barrier height V_{JB} increases slowly with increase in N/Z ratio in contrast to two nucleon transfer channels. On the other hand, with the inclusion of deformations, the trend in variation of V_{JB} remains similar as in Fig. 6.5(b) though with a difference in the magnitude of V_{JB} (being relatively smaller for N/Z-ratio case).

Further the effect of transfer channels and N/Z ratio is tested over spin orbit density independent part 'V_P'. The spin-orbit independent interaction potential at T=0 MeV for both spherical and deformed choice of nuclei is shown in Fig. 6.6(a,c) and Fig. 6.6(b,d) respectively. It is clear from the left panel of Fig. 6.6 that, indepen-

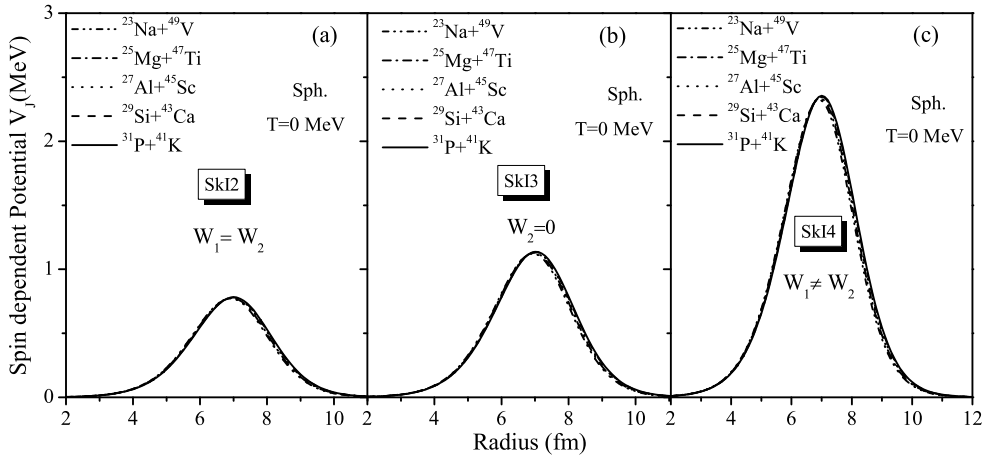

Figure 6.7: The spin-orbit density dependent interaction potential V_J as a function of R (fm) at T=0 (MeV) for spherical nuclei using (a) SkI2 (b) SkI3 and (c) SkI4 Skyrme forces.

dent of chosen reactions, the spin-saturated potential (V_P) is attractive for spherical reactions i.e. it does not show a repulsive core at a shorter distance. With the inclusion of deformation within optimum orientations approach, all chosen systems show attractive behavior at larger distances followed by repulsive core at shorter interaction range. It implies that, in the pocket formation process, β_2-deformation play significant role as depicted in the right panel of Fig. 6.6. Consequently, the barrier characteristics get modified i.e. the oblate shaped nuclear systems having higher spin barrier show narrow fusion pocket followed by prolate and spherical shaped nuclei. It is relevant to mention here that, no fusion pocket is seen for ^{29}Al+^{45}Sc and ^{31}P+^{41}K reactions as both projectile and target are spherical here.

Subsequently, the effect of two parameter spin-orbit potential (W_0 and W_0') is analyzed for transfer reactions as shown in Fig. 6.7. It may be noted that within DCM, the contribution of V_J till now is studied by using single spin-orbit potential i.e. $W_0 = W_0'$ only. In order to explore the specific role of spin-orbit parameters (W_0 and W_0'), the Skyrme forces SkI2 ($W_0 = W_0'$), SkI3 (W_0'=0) and SkI4 ($W_0 \neq W_0'$) are used here. Fig. 6.7 illustrate that, the presence of two parameter spin-orbit potential in spin-orbit part of interaction potential impart significant influence, as the magnitude of V_J become highest for SkI4 and least for SkI2 Skyrme force. On

adding deformation effects (not shown here), the enhancement in magnitude of V_J is observed whereas pattern remains same as observed in Fig. 6.5(b). This justifies our previous result that, the behavior of spin orbit potential is independent of the transfer channel as well as the choice of Skyrme force. Summarizing these results, we find that, the double S-O parameters of the spin-orbit strength significantly affect the spin-orbit density dependent potential V_J and consequently influence the fusion dynamics of nuclear systems. Hence, the relative influence of these Skyrme forces is further analyzed on fusion excitation functions of ^{72}Se* compound nucleus. The calculation and results are discussed in section 6.3.

6.3 Decay of ^{72}Se* compound nucleus using Skyrme forces and Blocki *et al.* potential

The fusion hindrance in heavy ion reactions has become a subject of interest as the steep fall of the fusion cross-section at sub-barrier region grab a lot of attention, and is analyzed extensively on experimental as well as theoretical fronts. In literature various theoretical models have been available to describe fusion hindrance phenomena. However, the most commonly used models during a present date to explain the deep sub-barrier fusion data are (a) based on sudden approximation using M3Y potential with repulsive core given by Misicu and Esbensen [21] (b) a dynamical two-step model proposed by Ichikawa *et al.* [22] based on adiabatic picture. In both the pictures, the shape of interaction potential is modified in terms of thicker barrier and shallower pocket. Likewise, in the dynamical cluster-decay model (DCM) barrier modification effects at sub-barrier energies are governed through barrier lowering parameter ΔV_B which arises in a natural way by the fitting of only parameter of the model, the neck-length ΔR.

Recently an experiment was performed at Argonne National Laboratory by Jiang and co-worker [23] using super-conducting linear accelerator ATLAS to measure the

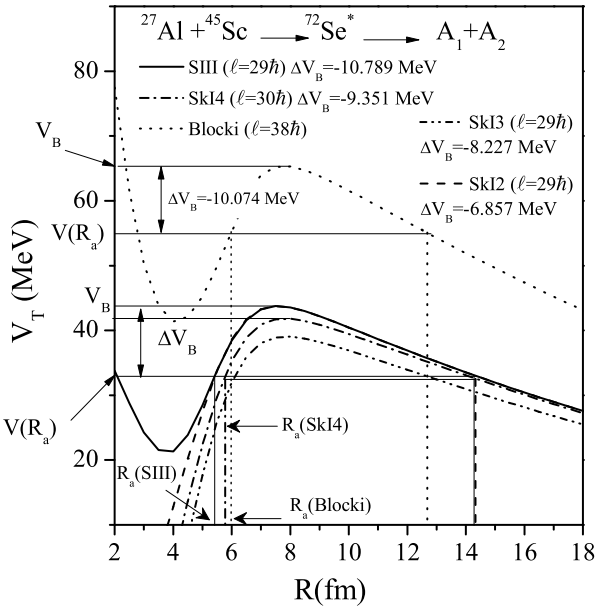

Figure 6.8: Total interaction potentials V_T (R) for the decay of ^{72}Se* plotted using SIII, SkI2, SkI3, SkI4 Skyrme forces and the Blocki potential at fixed $E_{c.m.}$ (T=2.337 MeV). Here barrier lowering is defined as ΔV_B=V(R_a) - V_B and R_a=R_1+R_2+ΔR.

evaporation residue cross-section for a positive Q-value ^{27}Al+^{45}Sc reaction down to about 300 nb. The theoretical calculations were performed using coupled channel (CC), optical model and shallow model. Both CC and optical model calculations show fusion hindrance for this system, whereas shallow potential model reproduces the data. In the present work, we use the two approaches (i) semiclassical SEDF in extended Thomas-Fermi approach, where kinetic energy and spin-orbit densities are expanded up-to the second order and two parameter Thomas-Fermi density is used as nuclear density with its parameters taken from [13]. (ii) based on Blocki *et. al.* potential [9] , which gives analytical description of nuclear potential. In this section, different nuclear interaction potentials are used to study the decay of ^{72}Se* nucleus formed in ^{27}Al+^{45}Sc reaction within dynamical cluster decay model (DCM) [24, 25] using both spherical as well deformed nuclei within optimum orientations [19].

Fig. 6.8 shows the total interaction potential V_T at temperature T=2.337 MeV as a function of inter-nuclear distance R(fm) plotted with SIII, SkIx (x=2,3,4) Skyrme

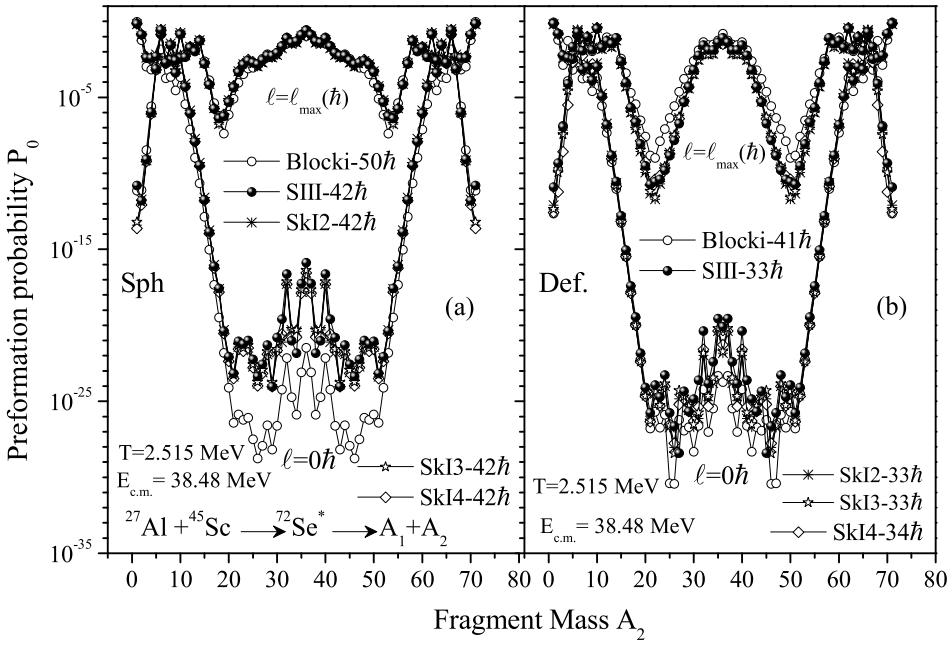

Figure 6.9: Preformation Probability P_0 as a function of fragment mass A_2 of ^{72}Se* system at comparable $E_{c.m.}$=38.48 MeV using SIII, SkI2, SkI3, SkI4 and Blocki potentials for (a) spherical and (b) β_2-deformed choice of nuclei.

forces and Blocki potential. The figure illustrates that, the barrier height V_B as well as barrier position R_B gets significantly modified with the use of different interaction potentials i.e. SIII, SkI2, SkI3, SkI4 and Blocki, thereby affects the barrier tunnelling probability P. The highest barrier is obtained on using Blocki *et al.* potential in comparison to chosen Skyrme forces. Out of the four selected Skyrme forces, SIII and SkI2 with W_0=$W_0^{'}$ attain highest barrier followed by SkI4 with W_0≠$W_0^{'}$ and SkI3 with $W_0^{'}$=0 has lowest barrier. In DCM, the first turning point R_a of penetration path define the effective "barrier lowering" ΔV_B for each decay channel. From the graph, it is clear that, for all considered potentials, the first turning point is different, which is further controlled via appropriate choice of neck parameter ΔR (different for different potentials as shown later in Fig. 6.10). As a consequences of this, the corresponding barrier modification ΔV_B comes into picture (see Eq. (2.52) of chapter 2), which helps to address the experimental data using different proximity interactions (discussed later). This indicates that, the effect of using

Table 6.2: The ER and IMF cross-sections of ^{72}Se* system, calculated using the DCM with deformed choice of nuclei at different $E_{c.m.}$'s for SIII Skyrme force compared with the experimental data [23].

$E_{c.m.}$	Temp.	ΔR	ℓ_{max}	σ_{DCM}(mb)			$\sigma_{ER}^{Expt.}$(mb)
(MeV)	(MeV)	(fm)	($\hbar$)	Without V_J	With V_J		
				σ_{ER}	σ_{IMF}	σ_{ER}	
31.74	2.337	0.57	29	2.26×10^{-5}	6.56×10^{-6}	2.03×10^{-4}	2.76×10^{-4}
32.49	2.357	0.74	30	5.23×10^{-4}	4.00×10^{-5}	0.00270	0.00245
33.06	2.373	0.84	30	2.47×10^{-3}	9.90×10^{-5}	0.0101	0.0104
33.67	2.389	0.94	31	1.28×10^{-2}	6.17×10^{-4}	0.0418	0.0425
34.28	2.406	1.05	31	5.63×10^{-2}	2.38×10^{-3}	0.153	0.152
34.85	2.421	1.11	31	0.292	5.19×10^{-3}	0.582	0.574
35.50	2.438	1.20	32	1.19	2.91×10^{-2}	2.06	2.038
36.46	2.463	1.35	32	5.47	0.178	8.39	8.248
37.62	2.493	1.48	33	15.1	1.07	21.6	21.932
38.48	2.515	1.55	33	37.0	2.23	49.6	48.130
39.41	2.539	1.61	33	46.7	3.94	64.1	65.98
40.75	2.572	1.67	33	95.9	6.69	121.0	122.19
42.48	2.615	1.747	34	142.0	16.1	174.0	175.70
44.78	2.671	1.80	34	213.0	22.8	255.0	255.49
47.42	2.733	1.876	34	363.0	33.5	424.0	424.86
50.05	2.794	1.971	34	555.0	66.4	598.0	611.29

different interaction potentials is to modify the barrier characteristics and hence the fusion cross-sections accordingly.

The relative effect of SEDF based interactions and usually applied Blocki *et al.* potential is further examined on the preformation profile of ^{72}Se* nucleus. Fig. 6.9 shows the preformation probability of decaying fragments of ^{72}Se* compound nucleus obtained by solving Schrödinger equation (Eq. (2.28) of chapter 2) using SIII, SkI2, SkI3, SkI4 and Blocki potentials. In order to see the possible role of deformation and related orientation of nuclei, both spherical as well as deformed choices of fragments are taken as depicted in left and right panels of Fig. 6.9. The comparison of preformation probability P_0 is made at Coulomb barrier energy $E_{c.m.}$= 38.48 MeV. On comparing the preformation factor of both choices of nuclei, one gets (i) broad spectrum in fission region for the use of spherical case, which on inclusion of β_2 deformation within optimum approach becomes narrower (ii) the

symmetric mass distribution is observed at ℓ=ℓ_{max} for both spherical and deformed nuclei, irrespective of choice of interaction potential. (iii) The effect of Blocki versus Skyrme based potential is evident at lower ℓ-values at which evaporation residue data is addressed. The contribution of some asymmetric fragments (intermediate mass fragments (IMF)) is also seen for spherical as well deformed choice of fragmentation. From Fig. 6.5, Fig. 6.6 and Fig. 6.9, it is clear that deformation effects modify the barrier characteristics, and subsequently the decay pattern gets influenced significantly. Therefore the further analysis is carried out with the deformed choice of nuclei only.

Next, the evaporation residue (ER) cross-sections of ^{72}Se* system are calculated using β_2-deformed choice of nuclei in reference to experimental data of [23]. Using different Skyrme forces within the framework of DCM, the fitting is done by optimizing the neck-length parameter "ΔR". The calculations are performed with and without the inclusion of spin-orbit part V_J in the total interaction potential. Table 6.2 depict the case for SIII and in Table 6.3 result of SkI2, SkI3 and SkI4 Skyrme forces are shown. It is anticipated from the tables that, the ER cross-sections are influenced significantly by the contribution of double spin parameter in the spin dependent part. One may observe that σ_{ER} deviates from experimental data by $\sim$ 56 mb for SIII, $\sim$ 76 for SkI2, $\sim$ 62 for SkI3 and $\sim$ 120 mb for SkI4 force, when V_J is excluded. The decrement in ER cross-section is larger for SkI4 force as compared to other Skyrme forces, showing the effect of double spin-orbit parameter. However, the ER cross-sections find nice agreement with available experiential data after the inclusion of spin-orbit part. Therefore, a study based on such analysis reveals that the double spin-orbit parameters of spin-orbit strength greatly influence the fusion dynamics of heavy ion induced reactions.

Table 6.3: Same as Table 6.2 but for SkI2, SkI3 and SkI4 Skyrme forces. The fitted neck-length ΔR values are shown in Fig. 6.10.

$E_{c.m.}$	Temp.	$\ell_{max}(\hbar)$			$\sigma^{ER}_{withoutV_J}$(mb)			$\sigma_{Expt.}$(mb)
(MeV)	(MeV)	SkI2	SkI3	SkI4	SkI2	SkI3	SkI4	
31.74	2.337	29	29	30	9.47×10^{-5}	8.51×10^{-5}	9.26×10^{-6}	2.76×10^{-4}
32.49	2.357	30	30	30	1.34×10^{-3}	1.12×10^{-3}	2.12×10^{-4}	0.00245
33.06	2.373	30	30	30	4.35×10^{-3}	3.03×10^{-3}	7.68×10^{-4}	0.0104
33.67	2.389	30	30	31	0.0243	0.0225	5.95×10^{-3}	0.0425
34.28	2.406	30	30	31	0.0901	0.0725	0.0415	0.152
34.85	2.421	31	31	31	0.384	0.334	0.163	0.574
35.50	2.438	31	33	33	1.50	1.36	0.696	2.038
36.46	2.463	32	33	33	6.31	7.24	3.47	8.248
37.62	2.493	32	33	33	17.4	15.4	11.9	21.932
38.48	2.515	33	33	34	36.7	37.5	24.7	48.130
39.41	2.539	33	33	34	47.0	52.2	35.6	65.98
40.75	2.572	33	33	34	103.0	94.2	81.2	122.19
42.48	2.615	33	34	35	153.0	148.0	123.0	175.70
44.78	2.671	34	35	35	226.0	221.0	187.0	255.49
47.42	2.733	35	35	35	376.0	371.0	341.0	424.86
50.05	2.794	35	35	35	535.0	549.0	491.0	611.29

Table 6.3 continued...

$E_{c.m.}$ (MeV)	Temp. (MeV)	σ_{DCM}(mb) With V_J						$\sigma_{Expt.}$(mb)
		σ_{IMF}			σ_{ER}			
		SkI2	SkI3	SkI4	SkI2	SkI3	SkI4	
31.74	2.337	9.90×10^{-9}	5.89×10^{-8}	2.43×10^{-7}	2.76×10^{-4}	2.78×10^{-4}	2.74×10^{-4}	2.76×10^{-4}
32.49	2.357	1.19×10^{-6}	3.23×10^{-6}	5.53×10^{-6}	0.00243	0.00245	0.00246	0.00245
33.06	2.373	4.99×10^{-6}	1.12×10^{-5}	2.24×10^{-5}	0.0107	0.0107	0.0104	0.0104
33.67	2.389	3.53×10^{-5}	7.71×10^{-5}	3.33×10^{-4}	0.0423	0.0423	0.0421	0.0425
34.28	2.406	1.77×10^{-4}	3.60×10^{-4}	1.42×10^{-3}	0.136	0.150	0.150	0.152
34.85	2.421	1.22×10^{-3}	4.59×10^{-3}	7.95×10^{-3}	0.572	0.572	0.581	0.574
35.50	2.438	9.46×10^{-3}	6.09×10^{-2}	9.76×10^{-2}	2.09	2.02	2.02	2.038
36.46	2.463	0.102	0.374	0.60	8.28	8.25	8.29	8.248
37.62	2.493	0.367	1.08	2.28	21.1	20.4	22.1	21.932
38.48	2.515	1.29	2.64	7.35	48.3	48.7	48.3	48.130
39.41	2.539	2.20	4.18	11.1	65.2	65.0	65.3	65.98
40.75	2.572	4.84	6.73	20.5	124.0	121.0	123.0	122.19
42.48	2.615	8.55	15.9	41.2	176.0	176.0	176.0	175.70
44.78	2.671	17.0	29.4	52.8	244.0	256.0	258.0	255.49
47.42	2.733	33.5	45.1	86.2	427.0	422.0	408.0	424.86
50.05	2.794	60.2	72.7	141.0	583.0	611.0	610.0	611.29

The Intermediate Mass Fragments (IMF) cross-sections are not measured experimentally [23]. Using the same neck-length as that for ER, we have estimated the IMFs and fission cross-sections. The fission cross-sections come out to be negligibly small (not shown in the table) for all $E_{c.m.}$ values, whereas the contribution of IMFs is significant as shown in Table 6.2 and Table 6.3. It may be noted from Table 6.1 that, for the use of SIII force, the IMF contribution increases with increase in center of mass energy and becomes about 10 % of total cross-sections at higher incident energies. However for SkI2, SkI3 and SkI4 forces, the contribution of IMFs respectively increases to 9.84 %, 11.89 % and 23.0 % at highest energy as shown in Table 6.3. Thus the results shown in Tables again support the fact that the contribution of V_J (along with contribution of W_0 and W_0') play important role in fusion dynamics of nuclear systems.

Beside the use of Skyrme forces, the ER cross-sections for the reaction ^{27}Al+^{45}Sc $\rightarrow$ ^{72}Se* $\rightarrow$ A_1+A_2 are also calculated using Blocki *et al.* potential and the results are shown in Table 6.4. Table 6.4 demonstrate that DCM calculated cross-section find nice comparison with experimental evaporation residue cross-section ($\sigma_{ER}^{Expt.}$) using Blocki interaction potential. Further Fig. 6.10 depict the fitted value of ΔR for SIII, SkI2, SkI3, SkI4 and Blocki potentials as a function of center of mass energy $E_{c.m.}$. It shows that ΔR increases almost linearly with $E_{c.m.}$ independent of the choice of interaction potential. For SkI3 force larger neck-length is required to address the experimental ER data across the Coulomb barrier followed by SkI4, SkI2, SIII Skyrme forces and Blocki potential. It is to be noted that, SIII force demands greater neck-length than Blocki potential at above barrier region, whereas reverse is true to attain below barrier excitation functions. It is relevant to mention that the barrier lowering ΔV_B enters through neck-length parameter ΔR and shows its dominance at near and sub-barrier energy region, and hence impart useful input to address the below barrier phenomena such as fusion hindrance. In this work, we have addressed various factors that affect the barrier lowering parameter such as energy, angular momentum and the use of different nuclear interaction potentials

Table 6.4: The ER cross-sections of ^{72}Se* system, calculated using Blocki potential compared with the experimental data [23]. The fitted neck-length ΔR values are shown in Fig. 6.10.

$E_{c.m.}$ (MeV)	T (MeV)	ℓ_{max} ($\hbar$)	σ_{ER}^{DCM} (mb)	$\sigma_{ER}^{Expt.}$ (mb)
31.74	2.337	38	2.73×10^{-4}	2.76×10^{-4}
32.49	2.357	38	0.00243	0.00245
33.06	2.373	39	0.010	0.0104
33.67	2.389	39	0.055	0.0425
34.28	2.406	40	0.132	0.152
34.85	2.421	41	0.573	0.574
35.50	2.438	41	2.06	2.038
36.46	2.463	41	8.26	8.248
37.62	2.493	41	21.7	21.932
38.48	2.515	41	46.8	48.130
39.41	2.539	41	67.4	65.98
40.75	2.572	41	125.0	122.19
42.48	2.615	41	178.0	175.70
44.78	2.671	41	255.0	255.49
47.42	2.733	41	426.0	424.86
50.05	2.794	41	610.0	611.29

etc. To study this, Fig. 6.11 is plotted, showing the variation of barrier lowering parameter (ΔV_B) as a function of center of mass energy ($E_{c.m.}$) for the deformed choice of decaying fragments. On left panel of Fig. 6.11, ΔV_B is shown for SIII force at ℓ_{min} and ℓ_{max} values and on right hand side the variation is shown for SIII, SkI2, SkI3, SkI4 and Blocki potentials at ℓ=ℓ_{max}. Fig. 6.11(a) illustrates that, the value of ΔV_B shows decrement in its magnitude as the center of mass energy $E_{c.m.}$ increases. At minimum angular momentum ℓ_{min}, the value of ΔV_B is higher (i.e. more negative) than maximum angular momentum ℓ_{max}. This imply that, the higher barrier modification is required for lower $E_{c.m.}$ and ℓ-values, which in turn seem to suggest that the corresponding fusion probability may decrease, giving rise to the occurrence of fusion hindrance at sub-barrier region.

The barrier modification effect is analyzed further in Fig. 6.11(b) using considered Skyrme forces and Blocki based potential. One can see that ΔV_B follows the trend of ΔR for all choices of proximity potentials (see Fig. 6.10). From Fig.

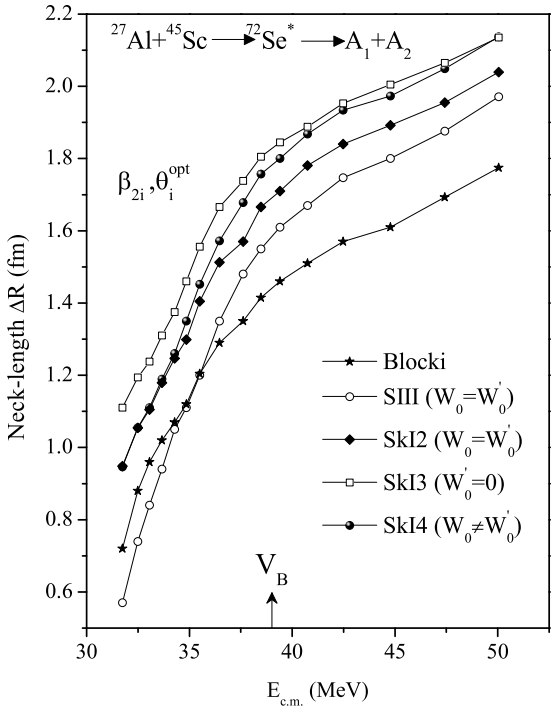

Figure 6.10: Comparison of neck-length parameter ΔR for different nuclear potentials varying as a function of $E_{c.m.}$.

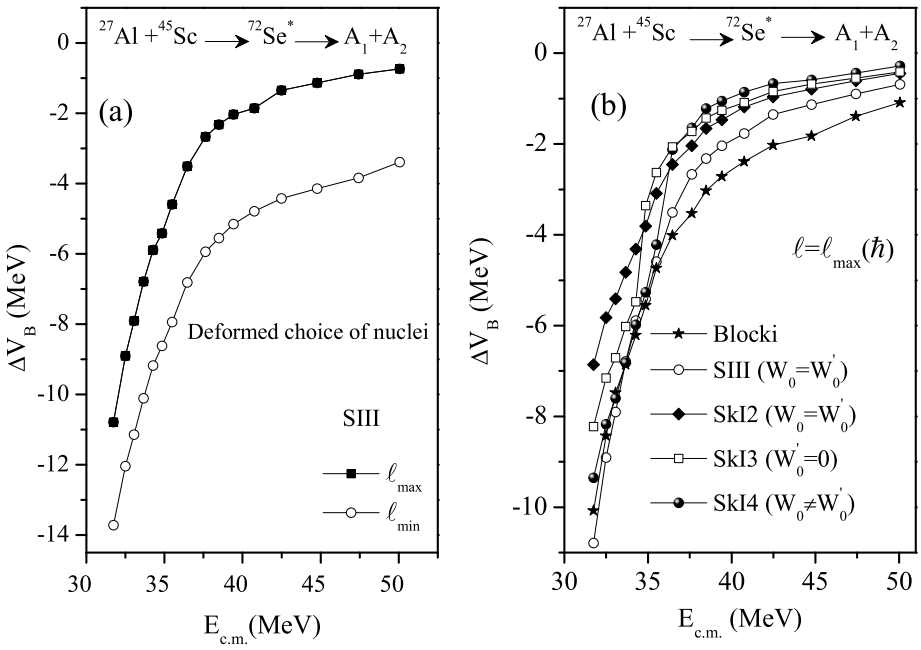

Figure 6.11: Barrier-lowering parameter ΔV_B as a function of $E_{c.m.}$ for highest contributing fragments (a) for SIII force at $\ell = \ell_{min}$ and $\ell = \ell_{max}$ and (b) for different interaction potentials.

Table 6.5: The predicted ER cross-sections and ℓ-values of ^{23}Na+^{49}V, ^{25}Mg+^{47}Ti, ^{29}Si+^{43}Ca and ^{31}P+^{41}K channels forming ^{72}Se* compound system, calculated at extreme $E_{c.m.}$, using the same neck-length as for ^{27}Al+^{45}Sc reaction with SIII Skyrme force.

Reactions	Temp. (MeV)	ℓ_{max} ($\hbar$)	σ_{DCM} (mb)
	$E_{c.m.}$=31.74 MeV		
^{23}Na+^{49}V	2.357	29	2.01×10^{-4}
^{25}Mg+^{47}Ti	2.340	29	2.03×10^{-4}
^{29}Si+^{43}Ca	2.279	29	2.03×10^{-4}
^{31}P+^{41}K	2.288	29	2.02×10^{-4}
	$E_{c.m.}$=50.05 MeV		
^{23}Na+^{49}V	2.811	35	578.28
^{25}Mg+^{47}Ti	2.797	35	693.72
^{29}Si+^{43}Ca	2.746	35	477.40
^{31}P+^{41}K	2.753	35	585.98

6.11(b), it is anticipated that, at below barrier energies, ΔV_B is more negative for SIII as compared to other interaction potentials. This means that larger barrier lowering is needed for SIII force and least for SkI4 force. The above results emphasize the fact that the barrier characteristics can be optimized via proper choice of neck length parameter which may in turn help to address the fusion hindrance phenomena governed at sub-barrier energy regime.

Finally, we have predicted the ER cross-sections of ^{23}Na+ ^{49}V, ^{25}Mg+^{47}Ti, ^{29}Si+^{43}Ca and ^{31}P+^{41}K reactions forming ^{72}Se* compound system at extreme center of mass energy i.e. $E_{c.m.}$=31.70 MeV and $E_{c.m.}$=50.05 MeV as shown in Table 6.5. The calculations are done by taking same neck-length parameter ΔR as taken for ^{27}Al+^{45}Sc reaction.

6.4 Conclusions

A systematic study is carried out to see the influence of deformation and orientation on spin-orbit density part V_J by employing various prolate and oblate shape nuclei

within the Skyrme Energy Density Formalism. The deformation is included upto β_2 lying within range of $0.023 \leq \beta_2 \leq 0.531$ for prolate and $-0.242 \leq \beta_2 \leq -0.592$ for oblate nuclei. We observed that, independent of magnitude of prolate deformed nuclei, higher spin-orbit barrier and lowest spin-orbit barrier position corresponds to orientation 90^0, which for oblate shape nuclei changes to orientation angle 0^0. The spin-orbit barrier and position is significantly influenced by both the sign and magnitude of deformation. The oblate shape nuclei ($\beta_2 < 0$) exhibit higher spin-orbit barrier (and lowest barrier position) in comparison to prolate systems ($\beta_2 > 0$). Also, the pocket of total interaction potential become more shallower with the inclusion of spin-orbit effect. In addition to this, the angular dependence of spin-orbit part is studied on fusion cross-section by taking both prolate and oblate systems. It is observed that, fusion cross-sections are maximum at θ_2=0^0 for prolate and θ_2=90^0 for oblate nuclei and their magnitude reduces slightly after inclusion of spin-density effect.

Along with this, the role of the spin-orbit density dependent and independent parts of interaction potential is studied for the two nucleon transfer process of ^{23}Na+^{49}V,^{25}Mg+^{47}Ti,^{27}Al+^{45}Sc, ^{29}Si+^{43}Ca and ^{31}P+^{41}K reactions forming ^{72}Se* compound nucleus by considering spherical as well as deformed choices of nuclei. For spherical choice, the barrier height and the barrier position are almost unaffected for the chosen set of reactions. However, the same gets influenced significantly after inclusion of deformations, depending on the sign and magnitude of quadrupole deformation. Deformations play important role in spin independent potential (V_P), as the fusion pocket start appearing for deformed case, which otherwise diminish for spherical nuclei. The same exercise is done for increase in N/Z ratio of Se by considering five even isotopes of $^{68-76}$Se*. Beside this, the effect of adding two parameter spin-orbit potential is analyzed for the two nucleon transfer reactions by employing SkI2, SkI3 and SkI4 Skyrme forces. In addition to this, the decay path of ^{72}Se* compound nucleus is studied within framework of dynamical cluster de-

cay model (DCM). The comparative analysis of SEDF (SIII, SkI2, SkI3 and SkI4 Skyrme forces) and Blocki based interaction is performed in the form of preformation probability and barrier lowering effects.

After an extensive analysis of nuclear dynamics of a variety of compound systems formed in heavy ion induced reactions at low energy region in chapters 3-6, a brief summary of the work and possible future prospects are explained in the next chapter.

Bibliography

[1] A. Iwamoto and P. Moller, Nucl. Phys. A **605**, 334 (1996).

[2] D. Jain, R. Kumar and M. K. Sharma, Nucl. Phys. A **915**, 106-124 (2013).

[3] Rajni, R. Kumar and M. K. Sharma, Phys. Rev. C **90**, 044604 (2014).

[4] D. Jain, M. K. Sharma, Rajni, R. Kumar and R. K. Gupta, Eur. Phys. J. A **50**, 155 (2014).

[5] D. Vautherin and D. M. Brink, Phys. Rev. C **5**, 626 (1972).

[6] C. Ngo *et al.*, Nucl. Phys. A **240**, 353 (1975).

[7] D. M. Brink and Fl. Stancu, Nucl. Phys. A **299**, 321 (1978).

[8] R. Bass, Nucl. Phys. **231**, 45 (1974).

[9] J. Blocki, J. Randrup, W. J. Swiatecki, and C. F. Tsang, Ann. Phys. (NY) **105**, 427 (1977).

[10] I. Dutt and R. K. Puri, Phys. Rev C **81**, 064609 (2010).

[11] R. K. Puri, P. Chattopadhyay and R. K. Gupta, Phys. Rev C **43**, 315 (1991); M. K. Sharma, R. K. Puri and R. K. Gupta, Eur. Phys. J. A **2**, 69-75 (1998); K. Puri, R. Arora and R. K. Gupta, Phys. Rev C **60**, 054619 (1999).

[12] R. K. Gupta, D. Singh, W. Greiner, Phys. Rev C **75**, 024603 (2007); R. Arora, R. K. Puri, and R. K. Gupta, Eur. Phys. J. A **8**, 103-114 (2000).

[13] R. K. Gupta, D. Singh, R. Kumar, and W. Greiner, J. Phys. G: Nucl. Part. Phys. **36**, 075104 (2009).

[14] P.-G. Reinhard and H. Flocard, Nucl. Phys. A **584**, 467-488 (1995).

[15] V. Blum, J. A. Maruhn, P.-G. Reinhard and W. Greiner, Phys. Lett. B **323**, 262 (1994).

[16] P. Moller and J. R. Nix, Nucl. Phys. A **361**, 117 (1981).

[17] M. Rashdan, Mod. Phys. Lett.**15**, 1287 (2000).

[18] C. Y. Wong, Phys. Rev. Lett. **31**, 766 (1973).

[19] R. K. Gupta, M. Balasubramanium, R. Kumar, N. Singh, M. Manhas, and W. Greiner, J. Phys. G: Nucl. Part. Phys. **31**, 631 (2005).

[20] J. Friedrich, P.-G. Reinhardt, Phys. Rev. C **33**, 335 (1986).

[21] S. Misicu and H. Esbensen, Phys. Rev. Lett. **96**, 112701 (2006).

[22] T. Ichikawa, K. Hagino and A. Iwamoto, Phys. Rev. C **75**, 064612 (2007).

[23] C. L. Jiang *et al.*, Phys. Rev. C **81**, 024611 (2010).

[24] B. B. Singh, M. K. Sharma, and R. K. Gupta, Phys. Rev. C **77**, 054613 (2008); R. Kumar, and R. K. Gupta, Phys. Rev. C **79**, 034602 (2010); R. K. Gupta, in *Cluster in Nuclei*, Lecture Notes in Physics 818, Vol. I, edited by C. Beck (Springer-Verlag, Berlin, 2010), p. 223.

[25] R. K. Gupta, S. K. Arun, R. Kumar, and M. Bansal, Nucl. Phys. A **834**, 176c (2010); . K. Sharma, S. Kanwar, G. Sawhney, R. K. Gupta, and W. Greiner, J. Phys. G: Nucl. Part. Phys. **38**, 055104 (2011).

Chapter 7

Summary and concluding remarks

In this thesis, the dynamics involved in various heavy ion induced compound nucleus (CN) reactions is studied at low energy regime. The main goal of this work is to explore the effect of excitation energy, angular momentum, deformation and orientation associated with the formation and decay of CN. Since, the CN processes are sensitive to such effects, a systematic study of these properties is used for better understanding of nuclear dynamics. The studied systems are chosen considering the fact that they provide an opportunity to address both the evaporation residue and fission channels, the main contributors of decay channel at low energy region. A brief account of heavy ion collision and related aspect occurring at low energy province have been discussed in chapter 1. To carried out the proposed work, various theoretical models are applied such as Wong formula, ℓ-summed Wong formula and the dynamical cluster-decay model (DCM). The CN formation is described using the framework of the Wong and ℓ-summed Wong formula, whereas for the decay part, dynamical cluster decay model (DCM) is employed. In Wong, barrier characteristics ($\hbar\omega$, V_B and R_B) are primary inputs, and are used to address the CN fusion cross-sections. On the other hand, within DCM, preformation probability P_0 and tunnelling probability P are exploited to attain the compound nucleus decay cross-sections. Both the nuclear models have been discussed in detail in chapter 2. Along with this, a brief interpretation of nuclear interaction potential obtained from

proximity theorem and from Skyrme energy density formalism (SEDF) is outlined in chapter 2.

In affirmation to Bohr independence hypothesis, it is believed that the formation and decay of CN are independent processes, besides the requirement of various conservation laws. However, as an exception, there may be a possibility that the decay channel retains the memory of colliding partners. Following this, the present work involves the investigation of entrance channel dependence in the formation and decay of CN ^{200}Pb* formed via ^{16}O+^{184}W, ^{19}F+^{181}Ta and ^{30}Si+^{170}Er reactions. Wong formula, ℓ-summed Wong formula and DCM are used respectively for fusion and decay processes. For the purpose of study, both spherical and deformed (quadrupole β_2) choices of nuclei are considered. Though all three entrance channels populates the same CN, but choice of different target-projectile combinations seem to influence the fusion cross-sections, as Wong based calculation is reasonably good to reproduce the experimental fusion data of ^{19}F and ^{30}Si-induced reactions and show deviation for ^{16}O+^{184}W reaction, where possibility of some non-compound nuclear process is anticipated. These facts directly indicate the signature of entrance channel dependence in formation of compound nucleus ^{200}Pb*. In addition to fusion, the entrance channel effect is also analyzed in the deformed fragmentation process of ^{200}Pb* nucleus. Moreover, the ER and fission cross-sections are predicted within energy range of $E_{c.m.}$ = 98-128 MeV. Finally the behavior of neighboring isotopes of ^{200}Pb* such as ^{192}Pb* and ^{202}Pb* is analyzed via total average kinetic energy, penetrability and mass yield distribution patterns. The detail description of this work is discussed in chapter 3.

The entrance channel effects are further examined in the decay of lower mass compound systems such as ^{76}Kr and ^{92}Zr using DCM, results are discussed in chapter 4. The role of iso-spin (N/Z ratio) and deformations is explored by analyzing the decay pattern of various Zr-nuclei formed in ^{16}O induced reactions. It is observed that the behavior of fragmentation potential and preformation probability gets in-

fluenced with inclusion of deformation effects as different systematics are obtained for spherical and deformed choices. Also, the dynamics of relatively heavier mass Sn isotopes is exercised using ^{16}O and ^{18}O projectiles. Beside this, the role of excitation energy and angular momentum is duly addressed.

It is observed that, the fusion evaporation and fusion-fission (ff) processes are affected by the excitation energy of projectile (or corresponding temperature), total angular momentum and associated moment of inertia etc. Considering this, in chapter 5 the study of ER and ff processes is carried out in terms of barrier characteristics, preformation probability and barrier lowering effects, where angular momentum effects are exploited via two approaches of moment of inertia such as sticking I_S and non-sticking I_{NS} limits. It is to be noted here that, in previous chapters, the deformation effects were added upto β_2 only, however in this chapter, the higher order nuclear deformations are considered i.e. from quadrupole β_2 (with optimum orientations) to hexadecapole β_4 (with compact orientations). Along with this, the role of dynamical deformation is also assimilated in the calculations. The barrier height (and corresponding position) and the preformation paths of ^{214,216}Rn* compound systems change significantly while going from I_{NS} to I_S approach and also dependent on the choice of deformations. The data of ER is successfully addressed within both the limits of moment of inertia at all incident energies for spherical as well as for deformed choices of decaying fragments, whereas the fission excitation functions are fitted within I_S limit only, specially after including deformations upto $\beta_4(0)$. Furthermore, the influence of increase in energy and neutron number is analyzed in reference to ER survival probability of Rn compound nucleus. It is confirmed that ^{216}Rn* system with N=130 has greater stability against fission as compared to ^{214}Rn* nucleus with N=128. Finally, the ff cross-sections of ^{214,216}Rn* nuclei are predicted using the sticking limit of moment of inertia as the same is more suitable for such decay process.

In all previous chapters, the nuclear interaction potential was obtained using an-

alytical method such as Blocki based pocket formula. Such kind of approaches does not comprises contribution from spin-orbit density dependent part, though they affect the fusion-fission dynamics substantially. In view of this, the role of both the spin-orbit density dependent (V_J) and independent (V_P) potentials obtained from Skyrme energy density formalism (SEDF) is probed independently along with deformation and orientation effects, and the results are discussed in chapter 6. Firstly the impact of deformation and orientation is explored on spin-orbit density dependent (V_J) part of nuclear interaction potential by considering $^{24-54}$Si+^{30}Si reactions. In which target ^{30}Si is spherical and projectiles $^{24-54}$Si have prolate and oblate shapes. In this work, the deformations are included upto β_2 only (quadrupole deformation), varying within range of $0.023 \leq \beta_2 \leq 0.531$ for prolate and $-0.242 \leq \beta_2 \leq -0.592$ for oblate projectiles. It is manifested from the calculations that, the effect of orientation on V_J is much prominent for nuclei with $\beta_2 < 0$ as compare to $\beta_2 > 0$. This study suggests that, for oblate-spherical shape system, the spin-orbit barrier finds most compact configuration at orientation $(0^0, 180^0)$, which for prolate-spherical system is obtained at $(90^0, 180^0)$. Subsequently this analysis is used to study the effect of both spin-orbit dependent and independent parts individually on two nucleon transfer reactions *i.e.* ^{23}Na+^{49}V, ^{25}Mg+^{47}Ti,^{27}Al+^{45}Sc,^{29}Si+^{43}Ca and ^{31}P+^{41}K forming the same compound nucleus ^{72}Se* using single spin-orbit parameter (W_0) Skyrme force *i.e.* SIII. In this work both spherical as well deformed nuclei are considered. One may conclude that, in transfer reactions, the spin barrier height V_{JB} as well as spin barrier position R_{JB} remain almost unaffected on considering spherical choice of target and projectile. However, the same get influenced significantly for deformed nuclei with optimum orientation. The effect of deformation is evident in V_P also as the fusion pocket start appearing, which otherwise dissipate for spherical systems. The same exercise is done for increase in N/Z ratio of Se by considering five even isotopes i.e. $^{68-76}$Se*. Beside this, the role of adding two parameters (W_0 and W_0') in spin-orbit potential is analyzed for the two nucleon transfer reactions by employing

SkI2, SkI3 and SkI4 Skyrme forces. In addition to this, the decay of $^{72}Se^{*}$ compound nucleus is investigated under the effect of various nuclear interaction potentials and efforts are made to address fusion hindrance phenomena.

The above work can be extended for the future study. The influence of double spin-orbit parameter W_0 and W_0' can be examined in the formation and decay channels of compound nucleus. In this work the impact of spin-orbit part of nuclear interaction potential via W_0 and W_0' is accounted on low mass system only, the contribution of W_0 and W_0' can be tested in fusion cross-section of variety of nuclear systems spread from low to super heavy mass region. In addition to this, one may explore the effect of higher order deformations (both negative and positive shapes) in reference to spin-orbit density dependent potential, which is tested for quadrupole shape of nuclei in this present work.